Optical near-field investigations of photonic structures for application in silicon-based thin-film solar cells

Alexander Markus Ermes

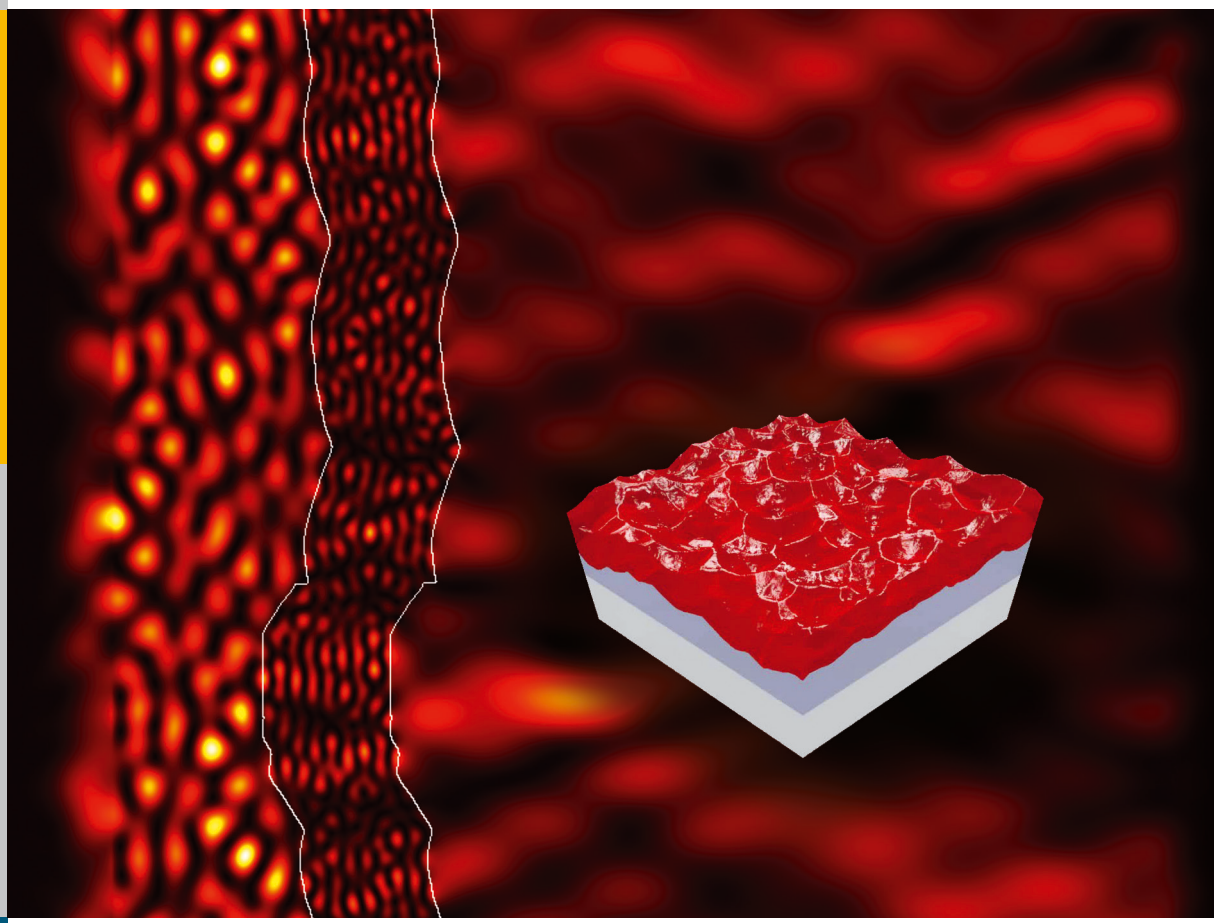

Energie & Umwelt / Energy & Environment
Band / Volume 299
ISBN 978-3-95806-108-8

JÜLICH FORSCHUNGSZENTRUM

Member of the Helmholtz Association

Schriften des Forschungszentrums Jülich
Reihe Energie & Umwelt / Energy & Environment Band / Volume 299

Forschungszentrum Jülich GmbH
Institute of Energy and Climate Research
IEK-5 Photovoltaics

Optical near-field investigations of photonic structures for application in silicon-based thin-film solar cells

Alexander Markus Ermes

Schriften des Forschungszentrums Jülich
Reihe Energie & Umwelt / Energy & Environment Band / Volume 299

ISSN 1866-1793 ISBN 978-3-95806-108-8

Bibliographic information published by the Deutsche Nationalbibliothek.
The Deutsche Nationalbibliothek lists this publication in the Deutsche Nationalbibliografie; detailed bibliographic data are available in the Internet at http://dnb.d-nb.de.

Publisher and Distributor: Forschungszentrum Jülich GmbH
Zentralbibliothek
52425 Jülich
Tel: +49 2461 61-5368
Fax: +49 2461 61-6103
Email: zb-publikation@fz-juelich.de
www.fz-juelich.de/zb

Cover Design: Grafische Medien, Forschungszentrum Jülich GmbH

Printer: Grafische Medien, Forschungszentrum Jülich GmbH

Schriften des Forschungszentrums Jülich
Reihe Energie & Umwelt / Energy & Environment, Band / Volume 299

D 82 (Diss. RWTH Aachen University, 2015)

ISSN 1866-1793
ISBN 978-3-95806-108-8

The complete volume is freely available on the Internet on the Jülicher Open Access Server (JuSER) at www.fz-juelich.de/zb/openaccess.

ABSTRACT

In this thesis, light scattering and propagation inside a silicon-based thin-film solar cell is investigated using optical simulations based on the finite-difference time-domain method. The special focus in this thesis lies in the analysis of the influence of randomly textured surfaces on cell performance. Due to the random nature of these structures and their varying sizes, simulation domains have to be sufficiently large to have a statistically significant distribution of features. The investigations focus on three different areas: The first area is light scattering at different interfaces in transmission as well as reflection. These simulations are compared to results from an improved scalar scattering model proposed by Dominé et al. [J. Appl. Phys. **107**, p. 044504, 2010]. The agreement of both methods is very good, with the limits of the scalar model lying in multiple interfaces and layers with a thickness below the peak-to-peak roughness of the surface. Secondly, the absorptance inside different hydrogenated amorphous and microcrystalline silicon layers is investigated for different structures; these include comparisons between conformal surfaces and surfaces as obtained in real devices by silicon growth. Further investigations in this area included simple stretching of the surfaces along different axes, as well as more complex modifications based on the scalar scattering theory; additionally, an amorphous/microcrystalline silicon solar cell is simulated and compared to experimental results to find limitations in the simulation approach. All of these simulations show a better performance for steeper features with a lateral size of about 500 nm. Additionally, the changes in topograhpy introduced by the silicon growth has a significant impact on cell performance. The last part of this thesis compares optical simulations to measurements of a scanning near-field optical microscope (SNOM). When comparing simulated intensities directly above a rough surface to measurements, it is found that the offset of the tip due to its finite physical size is the strongest influence, while light scattering at the tip has very little impact on (relative) intensity measurements.

ZUSAMMENFASSUNG

In dieser Dissertation werden Lichtstreuung und -ausbreitung in Siliziumbasierten Dünnschichtsolarzellen mithilfe optischer Simulationen untersucht. Als Simulationsmethode wird die sog. "Finite-Difference Time-Domain" oder FDTD-Methode genutzt. Der Schwerpunkt dieser Arbeit liegt in der Analyse von zufällig texturierten Oberflächen und deren Einfluss auf die Leistung der Solarzellen. Durch die zufällige Natur dieser Strukturen und deren sehr unterschiedlichen Größen müssen die Simulationen ein entsprechend großes Gebiet beinhalten, um eine statistisch signifikante Verteilung der Strukturen zu gewährleisten. Diese Untersuchungen beinhalten drei Bereiche: Zunächst wird die Lichtstreuung in Transmission und Reflexion an verschiedenen Grenzflächen betrachtet. Es werden dabei die Ergebnisse der Simulationen mit denen eines verbesserten skalaren Streumodells von Dominé et al. [J. Appl. Phys. **107**, p.044504, 2010] verglichen. Die Übereinstimmung der beiden Methoden ist sehr gut, wobei die skalare Streutheorie nur für einzelne Grenzflächen berechnet werden kann und die Ergebnisse für Schichten, die dünner sind als der maximale Hub der zugrundeliegenden Oberfläche, nicht aussagekräftig sind. Im zweiten Teil der Arbeit wird die Absorptionsveränderung in verschiedenen hydrierten amorphen und mikrokristallinen Siliziums-Schichten in Abhängigkeit von der Oberflächentextur untersucht. Dabei werden verschiedene Ansätze verfolgt: Zum einen werden Ergebnisse für konformale Oberflächen mit denen der durch das Siliziumwachstum modifizierten Strukturen verglichen, zum anderen werden einfache Modifikationen, speziell das Strecken und Stauchen einer Struktur, untersucht. Weiterhin wird eine mathematisch aufwendigere Modifikation auf Basis der skalaren Streutheorie behandelt. Außerdem wird eine Tandem-Solarzelle aus amorphem und mikrokristallinem Silizium untersucht, um Limitierungen der Simulationsmethode zu erörtern. Diese Simulationen haben eine Verbesserung der Solarzelle bei steileren Oberflächenstrukturen gezeigt. Zusätzlich ergibt sich ein starker Einfluss der Nicht-Konformalität auf die Leistung einer Solarzelle. Der letzte Teil dieser Dissertation beschäftigt sich mit dem Abgleich von Messungen einer Nahfeld-Mikroskop (scanning near-field optical microscopy - SNOM) mit Simulationen. Diese wurden sowohl mit als auch ohne die im SNOM eingesetzte Messspitze durchgeführt. Dabei hat sich durch den Vergleich der Simulationsdaten an verschiedenen Höhen über der Oberfläche mit Messungen ergeben, dass der durch die Spitzenausdehnung bedingte Abstand zur Oberfläche den stärksten Einfluss hat. Dagegen verändert die Lichtstreuung an der Spitze die (relative) Intensitätsmessung nur marginal.

Contents

1 INTRODUCTION 1

I FUNDAMENTALS 5

2 SILICON BASED THIN-FILM SOLAR CELLS 9
- 2.1 Light scattering in thin-film devices 12
- 2.2 Tandem thin-film solar cells 13

3 SIMULATION METHODS AND MODELS 15
- 3.1 Finite-Difference Time-Domain algorithm 15
  - 3.1.1 MEEP FDTD solver 17
    - Custom interface to MEEP used in this thesis 17
    - Limitations of the simulation software 18
- 3.2 Improved scalar scattering model 20

4 ANALYSIS METHODS 21
- 4.1 Intensity distribution 21
- 4.2 Absorptance 21
- 4.3 External Quantum Efficiency 22
- 4.4 Absorption Planes 23
- 4.5 Spectral Haze 27
- 4.6 Angular Intensity Distribution 27

5 EXPERIMENTAL METHODS 29
- 5.1 Atomic Force Microscopy 29
- 5.2 Angular Resolved Scattering 30
- 5.3 Scanning Near-Field Optical Microscope 31

II RESULTS 35

6 FAR-FIELD SCATTERING 37
- 6.1 FDTD vs. scalar model 37
  - 6.1.1 Spectral haze 40
  - 6.1.2 Angular intensity distribution 42
  - 6.1.3 Near-field effects 45
  - 6.1.4 Remarks about the use of the phase model 48
- 6.2 Scattering at flat front side and textured back side 49
  - 6.2.1 AID measurements, PM and FDTD 52
  - 6.2.2 Quantum efficiency and absorptance enhancement 55
  - 6.2.3 Conclusion 58

7 ABSORPTION AND QUANTUM EFFICIENCY 59
- 7.1 Non-conformal interfaces 59
- 7.2 Simple texture modifications 65

7.2.1 a-Si:H cell with PEC back contact 67
7.2.2 a-Si:H cell with a μc-Si:H back side 71
7.3 Textures optimised for light scattering 74
7.3.1 PM results 80
7.3.2 FDTD results 80
7.3.3 Conclusion 81
7.4 A complete tandem solar cell 82
8 FDTD SIMULATIONS AND NEAR-FIELD MICROSCOPY 87
8.1 Post-processing algorithm for topography artefacts 87
8.1.1 The post-processing algorithm 88
8.1.2 Samples 90
8.1.3 Offset Maps 90
8.1.4 Intensity Maps 92
8.2 Incorporating the near-field tip into simulations 96
8.2.1 Collecting tip over an idealised crater 96
8.2.2 Conclusion 105

III SUMMARY AND OUTLOOK 107
9 SUMMARY 109
10 OUTLOOK 113

IV APPENDIX 115
A DOCUMENTATION FOR THE SIMULATION SOFTWARE 117
B CONVERGENCE TESTS AND CONSIDERATION OF DIFFERENT RESOLUTIONS 121
Bibliography 124
List of Figures 149
Nomenclature 150
Acknowledgement 153
Assurance 157

1

INTRODUCTION

Optical simulations to investigate randomly nano-textured structures for applications in thin-film silicon (Si) solar cells - what does it mean, why is it necessary and why would anyone choose this as the topic for his thesis? And, as an extension, how could this area of research develop in the future?

What does it mean? Since random nano-textured structures in thin-film Si solar cells are investigated, I first have to explain these structures and why they are important for Si-based thin-film solar cells. The silicon-based thin-film solar cells investigated in this thesis consist of a layer stack containing a transparent conductive oxide (TCO), one or two hydrogenated amorphous (a-Si:H) or microcrystalline silicon (μc-Si:H) cells and a back contact, typically a combination of another TCO and silver (Ag). The silicon-based cells in these devices consist of a p-i-n type structure, an intrinsic layer between a p-doped and an n-doped layer. The nano-textured structures investigated consist mainly of textures applied to the TCO feature sizes that are typically in the range of the wavelength of the incident light. These textures induce light scattering at each interface between different layers, possibly scattering the light into an angle beyond the critical angle of total internal reflection, therefore effectively trapping the light inside a layer[1] and has been thoroughly investigated at the Institut für Energie- und Klimaforschung 5, Photovoltaik, FZ Jülich GmbH (IEK5).[2, 3]

So, why do we need this in Si-based thin-film solar cells? Since these are *thin-film* solar cells, the absorber layers inside the cell are typically much thinner than the thickness required to reliably absorb most of the light in the whole wavelength region for which the absorber material is of interest, 300 nm-800 nm for a-Si:H and 300 nm-1100 nm for μc-Si:H. The optical data of these materials as used in these thesis were obtained in the course of [4] This means that for flat interfaces, the light has to be absorbed in two passes through the cell, which is highly unlikely for wavelengths above 600 nm. Due to the light scattering induced by the textured surface, however, the amount of material it passes can be significantly improved by scattering into large angles and possibly total internal reflection. The exact numbers for this will be shown in the fundamentals chapter of this thesis.

Most investigations in this thesis, be it light scattering, absorption enhancement or investigations of a near-field tip, are focused on wet-etched zinc oxide structures, due to two reasons: Firstly, this is the primary system in use for the microcrystalline single junction and amorphous/microcrystalline tandem

solar cells at IEK5; secondly, due to the resolution limitations discussed in the fundamentals part of this thesis, finer structured samples cannot be resolved with the accuracy necessary for reliable results.

And why are these investigations carried out using simulations? Simulations give a unique opportunity to investigate structures far more rigorously than any experiment, up to the point that you can actually look what is happening *inside* the sample, an area not accessible by experiment. At the beginning of this thesis, the fabrication of textured TCOs was limited to as-grown roughness, wet-etching and buying a commercial substrate. This gives only very limited possibilities to modify the textures. With simulations, even the most unlikely and alien textures can be investigated at least theoretically. Additionally, when using a high-performance cluster (HPC) system, the time necessary for the simulation of even a whole spectrum is much shorter than that of fabricating an actual device, and much cheaper, too. You typically need one or two days for the fabrication of a cell - given there are no complications - and measurements, while the simulation time can be tuned to your needs; if you want to use your computation time efficiently, a spectrum can be calculated in twelve hours, if you need the results urgently, this can be reduced to as little as three hours when utilising more processors (CPU).

I chose this topic for my thesis for a multitude of reasons. One of the most important factors is that due to my disability, I am not able to perform experiments which rely on good dexterity or which require me to lift and carry around heavy objects. Therefore, a thesis consisting mainly of simulations and work on computers seemed ideal for me. Also, the opportunity to work in the HPC area was - and is - very interesting and give a fascinating insight into the working of these systems and the community. The fact that I could help to develop solar cells was a great opportunity too.

While I am reluctant to believe that solar cells will solve all of humanity's energy problems and stop global warming*, I personally think it mandatory for humanity to at least reduce its dependency on fossil fuels, all the more with recent development of oil prices, which are erratic to say the least, as is shown in Fig. 1.1[5]. Another sector in which photovoltaics - especially Si-based thin-film solar cells - can significantly improve people's lives is the third world, where there is no electricity grid with blanket coverage.[6]

The aforementioned savings in time and money when performing simulation also contributed to my decision to choose this topic for my thesis, since people and institutions have to save money wherever they can to be able to invest in more expensive fields.

Last but not least, this topic shows much promise for the future. With this (optimistic) outlook, I want to add the following remarks to this introduction:

When first starting this thesis, the idea of performing the simulations in the way I did was always closely related to the ability to utilise the supercomputing resources at the FZ Jülich. I essentially continued the work of Rockstuhl et

* in my opinion a system too complex to be predicted with today's simple models. Also, there is still ongoing discussion about much of the validity of measurements and results of the past decades

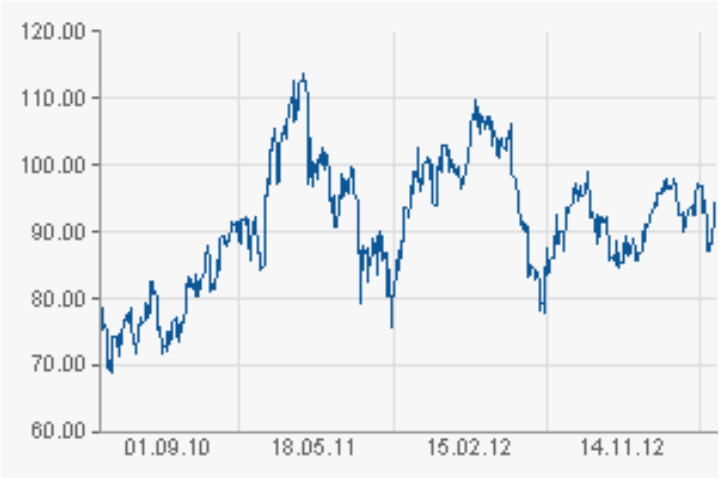

Figure 1.1.: 3-year chart of the oil-price (April 30th, 2013). The erratic behaviour in oil price is clearly visible with price differences between 70 USD and 150USD. Taken from [5].

al.[7], which was investigating effects of textures for a few choice wavelengths. With time, however, the price of computing resources dropped tremendously†, up to a point that the amount of computing power needed for a single wavelength simulation is now in the range of 2000 EUR, with the main contribution to that price being the memory‡. It is likely that even in the near future, the readily available computation power at each desk will be enough for such simulations. Also, there have been major advances in harnessing the compute power of graphics processing units (GPU) for simulations, which is orders of magnitude larger than that of conventional CPUs.[8]

Another interesting development during this thesis concerns the fabrication of arbitrary structures using nano-imprint lithography[9]. A significant portion of this thesis was to investigate how existing structures can be modified for better light scattering. However, these modified textures could not be created at all at the beginning of this thesis. With the development of nano-imprint lithography, however, it is very likely that these structures can be manufactured in the foreseeable future, even at a large scale.

And finally, the kind of investigation in this thesis and the tools used[10] can be applied not only to photovoltaic applications, but to all fields which rely on light propagation in thin layers and structures, e.q. the research on light emitting diodes (LED).[11, 12]

With this, I finish this introduction and hope to have given the reader an insight into my motivation for this thesis and the importance of this field of research.

† as it has done the past three decades

‡ at a necessary 32 Gigabyte§ for a single simulation

Part I

FUNDAMENTALS

To better understand the results of this thesis, some fundamentals have to be considered. First and foremost, the functionality of a silicon based thin-film solar cell has to be explained, especially the difference between a single and a multi junction device. Additionally, the light scattering in thin-film devices is introduced in detail, since this is one of the main motivations of this thesis.

Also, the simulation methods used in this thesis are introduced, with a focus on the Finite-Difference Time-Domain method used for *all* research in this thesis. This includes the algorithm as such as well as the actual software used for calculations and an analysis of its limitations. Additionally, an extended scalar scattering model is introduced, which was used especially for the analysis of light scattering.

The analysis methods applied to simulation results will be explained in short, with a special focus on a new analysis method to investigate local effects on absorption inside a layer, which is referred to as "absorption planes".

Closing this part of the thesis will be an introduction to the experiments to which simulations were compared, which include near-field microscopy, atomic force microscopy and angular resolved scattering.

2

SILICON BASED THIN-FILM SOLAR CELLS

In this chapter, silicon-based thin-film solar cells[13] will be introduced. Due to the main topic and investigations in this thesis, this introduction will focus strongly on the optical aspects of solar cells. In the first section, the basic principles of solar cell and light absorption therein will be discussed. These fundamentals are applicable to all kind of solar cells. In the next section, general properties of thin Si-based solar cells will be discussed. Following this, tandem devices will be explained with a-Si:H/μc-Si:H tandem cells as an example, since these are the state-of-the-art solar cells manufactured at IEK5 at the time of writing. The last section will focus on improving absorption in thin devices by utilising light scattering and trapping, again with a focus on silicon based devices, since this is the main way of improving solar cells at the IEK5.

The basic idea behind a solar cell is to convert light* into electrical power. The main materials to do this are currently semiconductors and this possibility was first discovered for silicon based pn-junctions in the 1960s at Bell Labs[14]. While new approaches include other methods of converting light to electrical power[15], the main idea for all types of photovoltaic devices is to absorb photons and convert them into free carriers. This is done by exciting electrons from the valence band into the conduction band, e.g. [16]. The dominating effect for this is the energy transfer from incident photons to the electrons in the valence band. A sketch of this can be seen in Fig. 2.1 for a direct (a) and indirect (b) semiconductor, with silicon being the latter. Depending on the material used in the solar cell, the amount of light absorbed at different wavelengths can be very different; examples for GaAs and Si can be found in [17] and [18]. For photons with an energy above the band gap, however, the additional energy is lost, which is also shown in Fig. 2.1. This loss is called "thermalisation loss".[16] Therefore, the band gap of the absorber material has to be chosen according to the incident solar spectrum. Another way of addressing this is shown in Sec. 2.2. For our applications, which consist mainly of terrestrial non-concentrated solar modules which need to utilise the AM1.5 spectrum[19], we focus on silicon in amorphous and microcrystalline form due to their abundance and low cost in manufacturing. Their absorption behaviour is shown in Fig. 2.2 alongside that of crystalline silicon (c-Si).[20, 21]

As can be seen, the absorption coefficients of these materials show a certain resemblance. However, crystalline silicon solar cells are typically fabricated

* Preferably from a near-infinite source which requires no energy input, such as the sun

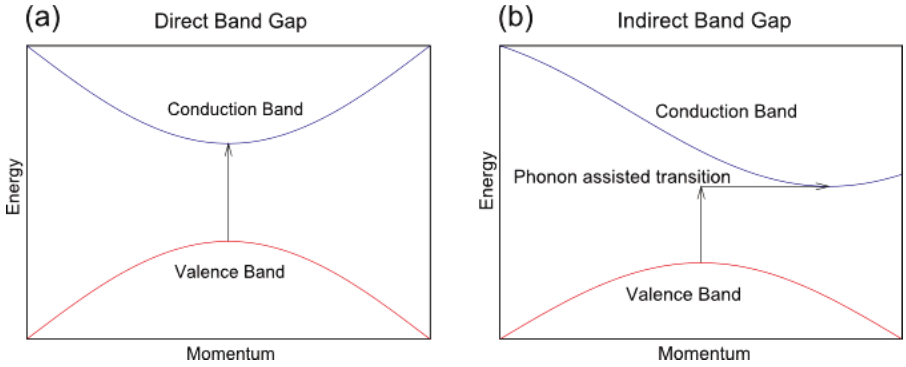

Figure 2.1.: Conversion of a photon into an electron-hole pair. If the energy of the photon is larger than the band gap, an electron-hole pair can be generated by exciting an electron from the valence into the conduction band. Any additional energy of the photon above the band gap is lost due to thermalisation. Drawings taken from [22].

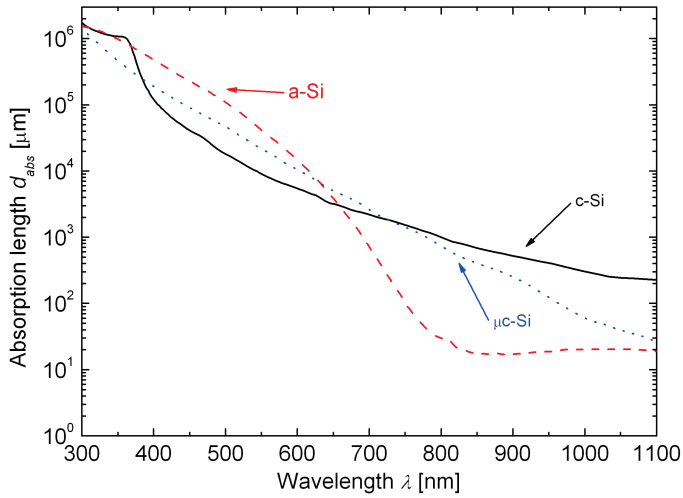

Figure 2.2.: Absorption coefficient alpha of crystalline (black, solid), amorhpous (red, dashed) and microcrystalline (blue, dotted) silicon. While there are some differences in the absorption of the materials, the trends are very similar. the notable differences are the significantly higher absorption of crystalline silicon in the low energy regime and the higher absorption for a-Si:H in the intermediate wavelength range between 350 nm and 600 nm.

from wafers with a thickness of the absorber layer of up to 200 µm,[23] while the cells produced at IEK5 have an absorber layer thickness between 300 nm and 2 µm.[24, 25] Looking at a quantity called the "absorption length", shown in Fig. 2.3, it is clear that these small thicknesses are only able to absorb a very small portion of the incident light, since the light only passes the absorber layer twice before leaving the cell: Once after entering the cell through the (transparent) front contact, and once more after being reflected at the back contact, which usually consists of a highly reflective metal, but can be transparent for bi-facial cells as well[26]. This simple view neglects multiple reflections inside the cell as well as losses in the metallic back contact, but is a good enough approximation to show the limitations of thin absorber layers. This effect grows stronger as the wavelength of the incident light increases, since light with energies slightly above the band gap is less likely to be absorbed in an indirect semiconductor. This is also reflected in the strongly increasing absorption lengths at wavelengths above 600 nm.

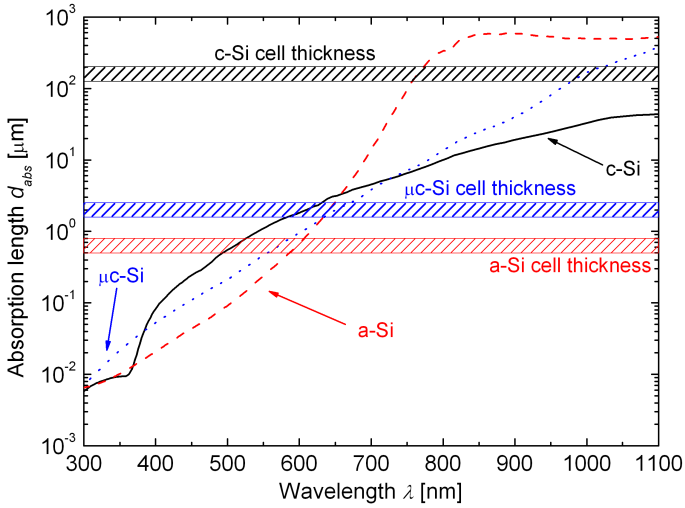

Figure 2.3.: Absorption length and typical absorber layer thickness for crystalline (black, solid), amorphous (red, dashed) and microcrystalline (blue, dotted) silicon. Since the thickness of a typical wafer-cell is always larger than the absorption length, these cells already show good performance without textured interfaces. For the amorphous and microcrystalline cells, however, absorber layer thicknesses are smaller than the absorption length at wavelengths above 600 nm. Therefore, the light path inside the absorber layers has to be increased significantly, e.g. by light scattering at textured interfaces.

These properties indicate that a good way to increase performance of the cell while retaining the small absorber layer thickness would be to increase the path length of the light inside the absorber layer. The most common way to achieve this will be discussed now: Light scattering at different interfaces.

2.1 LIGHT SCATTERING IN THIN-FILM DEVICES

As described above, the thin absorber layer thickness in thin-film solar cells is a major challenge when trying to obtain high efficiencies. For this to be successful, the amount of time the incident light spends in the cell has to be increased by a large amount, so the probability for light absorption increases.[27, 28] While with layer thicknesses below the wavelength of the incident light it cannot be described with ray optics, the term of "effective light path" is commonly used as a measure for light scattering, suggesting a linear path of the light inside the cell[28]. This effective light path is sketched in Fig. 2.4.

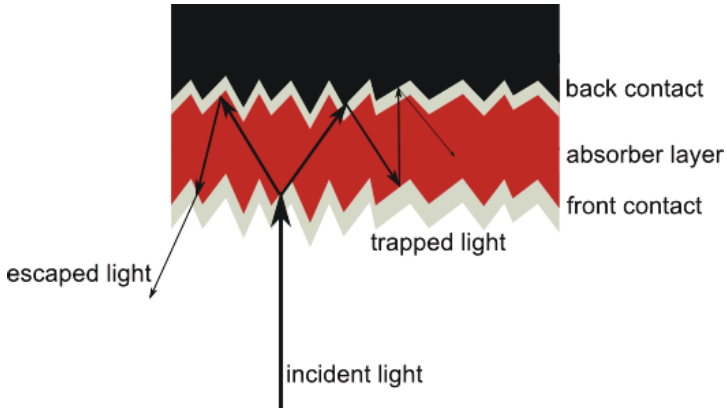

Figure 2.4.: Sketch of light trapping approximated using geometrical optics. A textured interface can scatter light into different angles. For small angles (left side), the light can couple out of the cell in the same way it could with flat interfaces, however the light path is increased by the angle. In the best case (right side), the light is scattered into an angle above the angle total internal reflection and trapped inside the absorber layer until it is absorbed.

The maximum increase in absorption - also referred to as "path length enhancement"[27, 28] and calculated using ray optics - can be expressed by an effective absorption coefficient for a material with refractive index n, real absorption coefficient α, reflectivity r and layer thickness d as:

$$\alpha_{eff} = \frac{1-r}{\frac{1-r}{4n^2\alpha d}+1} \tag{2.1}$$

$$\xrightarrow{\alpha<<1} \alpha_{eff} = 4n^2\alpha L. \tag{2.2}$$

This limit was first proposed by Yablonovitch in 1982[29]. To obtain light scattering inside a solar cell, in most cases the front and/or back contact are structured in some way or another. These include growth-induced textures[30], wet-chemical etching[31], fabrication of photonic crystals[32] or plasmonic scattering at the front or back contact[33] and nano-imprint lithography[9].

In this thesis, the focus will lie on commercially available or easily manufactured textures as a basis for all simulations and optimisations. These

include commercially available Asahi-U[34] structures, wet-chemical etched aluminium-doped zinc oxide (ZnO:Al) structures, developed in Jülich[31] and as grown textures of boron-doped zinc oxide (ZnO:B) deposited via liquid phase chemical vapour deposition (LPCVD) as developed at Neuchâtel[30] and plasmonics[33] or periodic structures[32].

These structures will also be modified to enhance light scattering and absorption in the active layer of the cell; this, however, are purely theoretical investigations. While it might be possible to create such structures using small-scale technologies such as electron beam lithography and then copy them to large areas using nano-imprint lithography, the growth behaviour of the different silicon layers has shown to be non-optimal for structures with high aspect ratios and steep flanks.

2.2 TANDEM THIN-FILM SOLAR CELLS

Another way to increase the performance of a thin-film solar cell is to make it a so-called "tandem cell" or "multi-junction cell"[16]. In this case, the device consists of multiple stacked cells with each cell consisting of a material with a different band gap. By using cells with band gaps that get smaller for each consecutive cell, the incident light can be used more efficiently, as described for example in[16]. Since most of the high energy photons are absorbed in the high band-gap materials at the front of the cell, the thermalisation losses in the bottom cell(s) are much smaller. Previous calculations[16] have shown a maximum efficiency of 86% for a multi-junction cell with an infinite number of materials covering the whole solar spectrum, neglecting losses in all but the absorber layers.

Since an infinite number of cells for a multi-junction cell are challenging to fabricate, the focus in research and industry lies on devices with two to four individual cells in a stack. At this institute, two-junction cells are the focus of research, due to the comparatively low manufacturing costs[35]. In these tandem cells, a combination of a-Si:H and μc-Si:H are used, with a-Si:H as the top cell due to the higher band gap. A sketch of the layer stack used for these cells is shown in Fig. 2.5(b); as a comparison, a typical layer stack of a single junction amorphous silicon cell is shown in Fig. 2.5(a). The absorption in a tandem device is similar to the single junction device (Fig. 2.1. Any photon that passes through the top cell unabsorbed can be absorbed in the lower band gap material of the bottom cell. These tandem cells have been shown to have an efficiency of about 14% which decreases to 10%[36] due to light induced degradation,[37] mostly in the a-Si:H layer[37]. An additional challenge is the fact that both cells are connected in series and therefore the current is limited by the cell in the stack which has the lowest short circuit current density. If the tandem cell is limited by the (μc-Si:H) bottom cell, in most cases it is sufficient to increase the cell thickness. For the a-Si:H top cell however, this is not the best approach due to light induced degradation.[37] In this case, the band gap can be adjusted by deposition parameters within a small area, or an intermediate

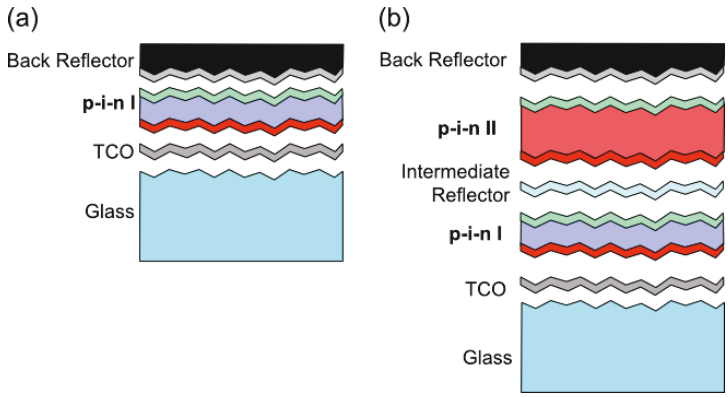

Figure 2.5.: Sketch of an amorphous silicon single junction (a) and an amorphous/microcrystalline silicon tandem solar cell (b). The tandem cell consists of two individual cells with absorber layers exhibiting different band gaps. The top cell consists of an amorphous silicon pin stack and the bottom cell of a microcrystalline pin stack. Optionally, an intermediate reflector can be placed between the two to improve current matching.

layer can be introduced to reflect high energy photons back into the top cell while low photons can pass through to the bottom cell. This leads to a higher current in the top cell, since more high energy photons are converted in the high band gap material, reducing thermalisation losses.

3

SIMULATION METHODS AND MODELS

After introducing the basics of the solar cells simulated in the course of this thesis, the simulation methods will be introduced now. The main focus will lie on the Finite-Difference Time-Domain method, which was used for each and every investigation in this thesis. Additionally, a short introduction will be given into an improved scalar scattering model.

3.1 FINITE-DIFFERENCE TIME-DOMAIN ALGORITHM

The simulation method mainly used throughout this thesis is based on the Finite-Difference Time-Domain (FDTD) method for solving Maxwell's equations. This method was first proposed by Yee in 1966[38] and has been discussed in detail, including implementation details, by Taflove et al.[39]. In principle, Maxwell's equations,

$$\frac{\partial \vec{B}}{\partial t} = -\nabla \times \vec{E} - \vec{M} \tag{3.1}$$

$$\frac{\partial \vec{D}}{\partial t} = \nabla \times \vec{H} - \vec{J} \tag{3.2}$$

$$\nabla \cdot \vec{D} = 0 \tag{3.3}$$

$$\nabla \cdot \vec{B} = 0 \qquad \text{with} \tag{3.4}$$

$$\vec{D} = \epsilon_r \epsilon_0 \vec{E} \tag{3.5}$$

$$\vec{B} = \mu_r \mu_0 \vec{H} \qquad \text{and} \tag{3.6}$$

$$\vec{J} = \vec{J}_{source} + \sigma \vec{E} \tag{3.7}$$

$$\vec{M} = \vec{M}_{source} + \sigma' \vec{H}, \tag{3.8}$$

where $\vec{E}$ and $\vec{D}$ are the electric field and electric flux density, respectively. $\vec{H}$ represents the magnetic field and $\vec{B}$ the magnetic flux density. $\vec{J}$ is the electric current density, $\vec{M}$ the equivalent magnetic current density, ϵ_r and ϵ_0 the relative and free-space permittivity, respectively. Lastly, μ_r and μ_0 are relative and free-space permeability. σ and σ' are the electric and magnetic conductivity, and $\vec{J}_{source}$ and $\vec{M}_{source}$ describe electric and magnetic sources, with the latter always being equal to zero ($\vec{M}_{source} = 0$). As described in [38], the Yee algorithm proposed to simplify these equations and adapt them to the so-called Yee-lattice, where electric and magnetic field components are placed at a dis-

tance of one half cell from each other in space and time, as illustrated in Fig. 3.1 for the discretisation in space. This figure was taken from [39].

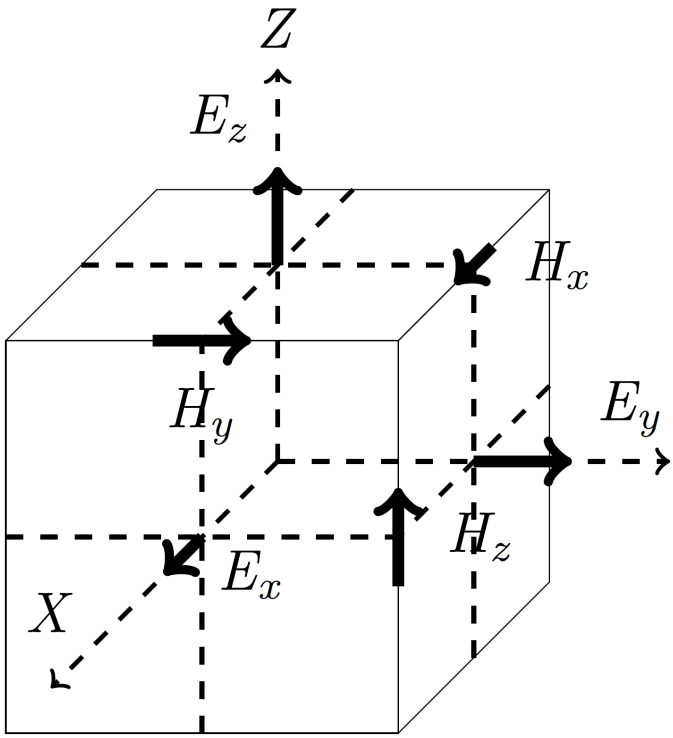

Figure 3.1.: Sketch of the Yee-cell, showing placement and direction of the electric and magnetic fields.[38]

By staggering the electric and magnetic field vectors in space as well as in time, a simplified version of Maxwell's equations, introduced and demonstrated by Taflove ([39], pp.67-87), reduces the problem of calculating these fields to a simple set of equations in the following form:

$$\vec{E}^{n+1} = \vec{E}_s + C_1\vec{E}^n + C_2\nabla \times \vec{H}^{n+1/2} \tag{3.9}$$

$$\vec{H}^{n+3/2} = \vec{H}_s + C_3\vec{H}^{n+1/2} + C_4\nabla \times \vec{E}^{n+1}, \tag{3.10}$$

where $\vec{E}_s$ and $\vec{H}_s$ are the source electric and magnetic fields, respectively, while $C_i, \quad \in \{1, 2, 3, 4\}$ are material constants at the respective position. These equations are only valid for single wavelengths with a constant dielectric function; while it is possible to include dispersive materials by approximating the dielectric function using oscillators of various kinds[4], it will not be introduced here, since each wavelength was simulated using a constant dielectric function. These equations are easily parallelised, and there are many implementations of the FDTD method available using multiple CPUs or even multiple nodes in a high performance computing (HPC) cluster. In this thesis, only one solver was used, which will be introduced in the following section.

3.1.1 *MEEP FDTD solver*

The software used to perform simulations was based on the MEEP FDTD solver, developed at MIT[10]. This software is being developed as open source, and is already parallelised for use with HPC cluster. This software is usually programmed using a SCHEME interface, which is well documented and offers many features. However, this interface has some serious shortcomings when used in combination with topographies of randomly textured surfaces; it is only possible to define simple geometrical shapes. Using these to model the random surface, one object has to be defined at each point of the surface, as shown in Fig. 3.2. This again has a serious impact on the initialisation speed of the simulation. For example, a single rough layer of 500×500 points leads to an initialisation time of approximately one hour, with each additional layer increasing this time by a similar amount. With typical calculation time being in the order of two to five hours and limited calculation time, this had to be improved. The chosen path of this thesis to circumvent these shortcomings as well as its limitations will be discussed in this section.

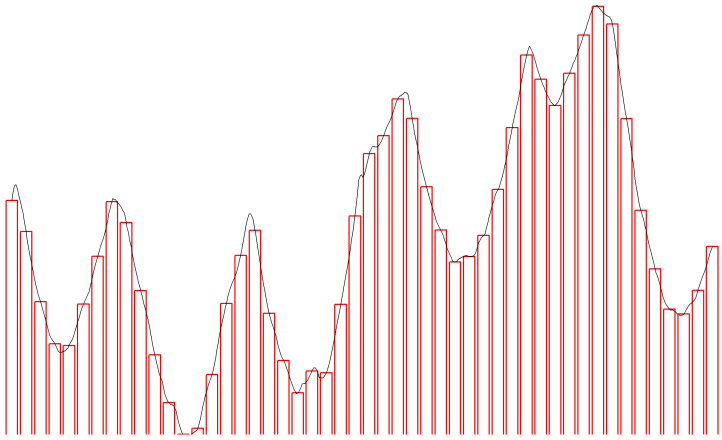

Figure 3.2.: Discretisation of a line of a topography scan by using rectangular blocks. The better the surface has to be approximated, the more blocks have to be defined. For an algorithm with an initialisation time depending on the number of blocks, a fine discretisation and/or a large domain lead to an extremely large number of blocks, increasing the initialisation time beyond the computation time, making the software unsuitable for use with HPC systems.

Custom interface to MEEP used in this thesis

In addition to the SCHEME interface, MEEP also offers a C++ interface via a header file. However, this interface is scarcely documented, with only a few

functions explained, and developing a simulation software using it proved to be a challenge. Due to the lack of documentation, only very few functions could be used for the software. The software developed in-house shortens initialisation to a maximum of 30 seconds, which is sufficiently small compared to calculation times. In contrast to the original interface, however, this software only allows for simulations of layer stacks of dielectric materials, with an optional tip of a near-field microscope for special investigations. This optimised software performs the following steps, as are shown in Fig. 3.3:

1. Read the configuration file and obtain number of layers, layer thicknesses, dielectric properties, wavelength and interface files.

2. Create arrays from interface files for all interfaces.

3. Calculate dielectric properties for all points (with a minimal memory footprint).

4. (optional) Include near-field tip in simulation.

5. Place light source.

6. (optional) Write dielectric constants for all points to disk as three-dimensional array.

7. Simulate a pre-defined number of time steps.

8. Write all complex electric fields to disk.

An example of a configuration file along with an explanation of all parameters is shown in chapter A.

Limitations of the simulation software

With all advantages and optimisation for the kind of investigations performed in the course of this thesis, this interface to the MEEP software has one distinct disadvantage: It is only possible to define a single dielectric constant for each material, and its real part must be positive*. This has two major consequences: Firstly, the only metal that can be simulated is a perfect electric conductor (PEC), so any absorption in a possible contact is neglected. Secondly, it is not possible, as would be in the SCHEME interface, to define the dielectric properties as a function of wavelength. Therefore, each wavelength has to be simulated independently, leading to a high computation time needed for a whole spectrum. Due to the large amount of data stored after the simulation is finished, however, a transient calculation including several wavelengths is also not possible with the resources at our disposal.

* with the exception of a perfect electric conductor, with $\epsilon_r = -\infty$

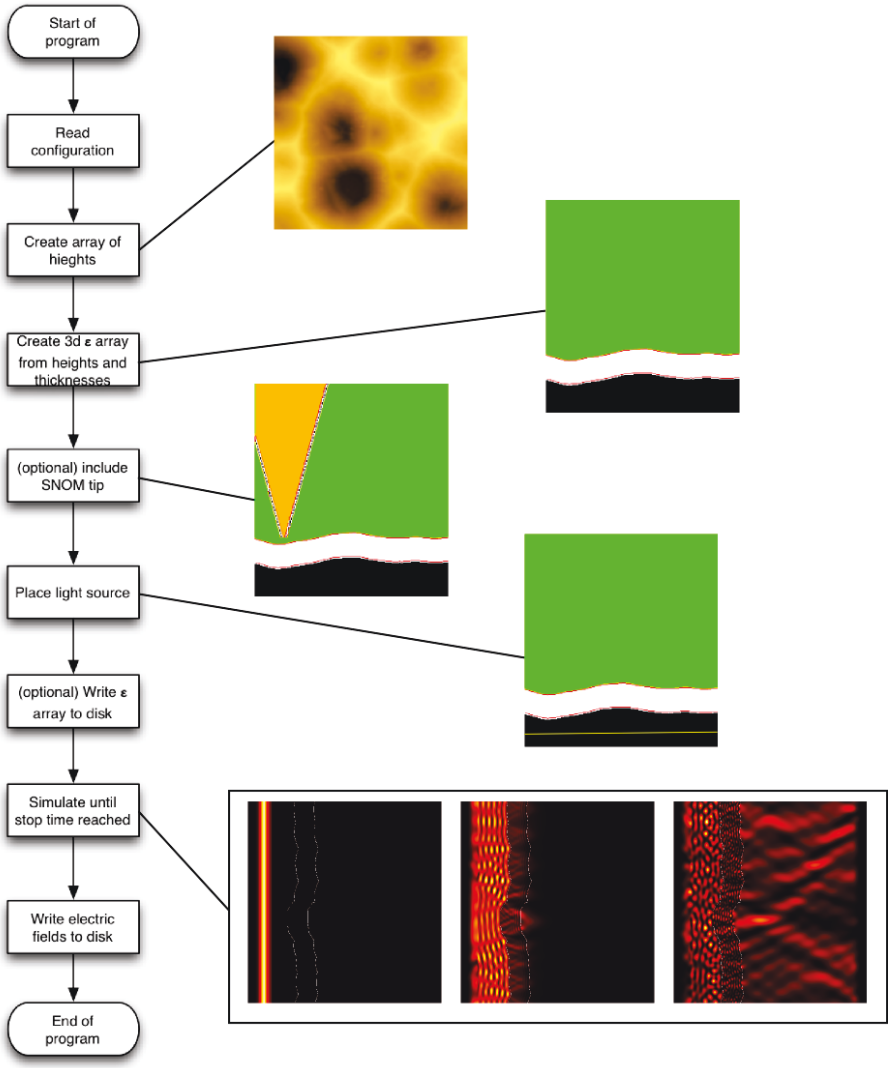

Figure 3.3.: Flow chart and example pictures of our custom MEEP interface. After reading the config file, the topography is read. From this, a three-dimensional representation of the optical properties is created. After optionally including the SNOM tip, a light source is placed. In this example, it is a planar illumination through the substrate. Before actual simulation, the real part of the dielectric function can optionally be written to disk. After this, the actual simulation runs for a pre-determined number of time steps, after which the electric fields are written to disk.

3.2 IMPROVED SCALAR SCATTERING MODEL

To investigate the light scattering at single interfaces, as is done in Chapter 6, an additional model is used for comparison with FDTD simulations. Based on scalar scattering theory, which includes many approaches[40, 41, 42], the extended scalar scattering model proposed by Dominé et al. in 2010[43] is used in this thesis and referred to as "phase model" (PM), and can be applied to any topography. This topography is assumed to be placed between two materials, both treated as a half-space. Therefore, this model only yields information for a single interface, and further analysis of this calculation should be considered as far-field effects. This model's principle is illustrated in Fig. 3.4.

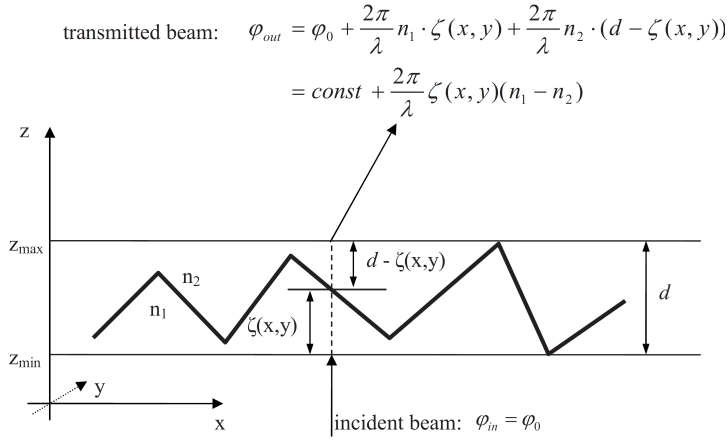

Figure 3.4.: Illustration of the phase model. At each point the height of the topography is used to calculate a phase shift based on the refractive index of the materials surrounding the interface.[43]

Essentially, for each point of the topography, a phase difference of the incident light is calculated via the following formula:

$$\phi_{out} = \phi_0 + \frac{2\pi}{\lambda} n_1 \cdot \zeta(x,y) + \frac{2\pi}{\lambda} n_2 \cdot (d - \zeta(x,y)) \tag{3.11}$$

$$= const + \frac{2\pi}{\lambda} \zeta(x,y)(n_1 - n_1) \tag{3.12}$$

In this equation, ϕ_{out} represents the resulting phase, ϕ_0 the initial phase, λ the wavelength of the incident light in vacuum, and n_1 and n_2 the refractive indices of the materials on the incident and transmitted side of the interface, respectively. $\zeta(x,y)$ represents the height of the topography at a given point x and y for a two-dimensional scan. The quality of this model and its predictive power will be discussed in detail in Chapter 6.

4

ANALYSIS METHODS

With the calculation methods introduced, the analysis methods will be introduced in this chapter, since the quantities obtained by FDTD are electric field distributions, not particularly useful on its own. In this section, essential quantities such as absorption, quantum efficiency and Fourier analysis of the electric fields will be described. Additionally, a special analysis was developed to correlate absorption inside a layer with surface features of the topography. These "absorption planes" will be discussed in more detail. For both FDTD and PM calculations, Fourier analysis allows for calculation of angular intensity distribution and light scattering into evanescent modes, which will also be introduced.

4.1 INTENSITY DISTRIBUTION

The first quantity to describe is a very simple one, on which many of the other analysis methods rely: The intensity distribution in a given system. The intensity is simply calculated by:[44]

$$I(x,y,z) = E_x^2 + E_y^2 + E_z^2 \tag{4.1}$$

$$= E_{x,r}^2 + E_{x,i}^2 + E_{y,r}^2 + E_{y,i}^2 + E_{z,r}^2 + E_{z,i}^2, \tag{4.2}$$

with $I(x,y,z)$ being the resulting intensity at the point x,y,z, and E_i the electrical field component in the respective direction x,y,z. With the electrical field being a complex number, the latter equation results. The fields and resulting intensity for an example system is shown in Fig. 4.1.

4.2 ABSORPTANCE

As next step from the intensity distribution, the absorptance in each point has to be considered, which is calculated as

$$A(x,y,z) = \frac{1}{2}\epsilon_0 c\omega \cdot \epsilon_i(x,y,z) \cdot I(x,y,z). \tag{4.3}$$

In this equation, ω represents the frequency of the incident light, ϵ_i the imaginary part of the dielectric function at the position (x,y,z), and $I(x,y,z)$ the intensity at the same point. This quantity is a measure of how much of the incident light is absorbed at any given point.

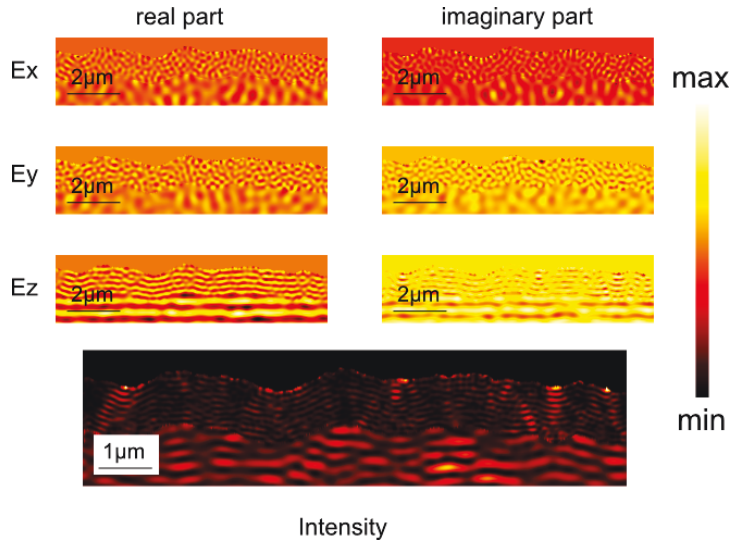

Figure 4.1.: Visual representation of the calculation of an intensity distribution in a modelled 1 µm thick µc-Si:H cell according to Eq. (4.1).

As an example of the difference the frequency and ϵ_i can have, Fig. 4.2 shows the intensity distribution (a) and absorptance (b) at a wavelength of 800 nm for a material system consisting of ZnO:Al and µc-Si:H.

4.3 EXTERNAL QUANTUM EFFICIENCY

To allow for a straight-forward comparison between experiment and simulation, the external quantum efficiency or *EQE* is used. For a real-life device, it is defined as the number of electrons extracted from the device divided by the number of photons entering the cell, or:

$$EQE(\lambda) = \frac{(\text{electrons/s})_{out}}{(\text{photons/s})_{in}}, \tag{4.4}$$

However, the simulations performed in the course of this thesis only account for optical effects, and not electrical effects. Therefore, an approximation has to be made for the number of electrons extracted from the cell. For all optical simulations, it is assumed that all absorbed photons are converted into electron/hole-pais and that all carriers are extracted. For this case, the formula for the EQE as obtained by simulations changes as follows:

$$EQE(\lambda) = \frac{A_{layer}}{I_0 \cdot S_{domain}}, \tag{4.5}$$

where A_{layer} is the absorptance in ta given layer, in this case the silicon layer(s) of the single junction or tandem device; I_0 is the intensity of the incident light*,

* which has to be calculated from an empty domain

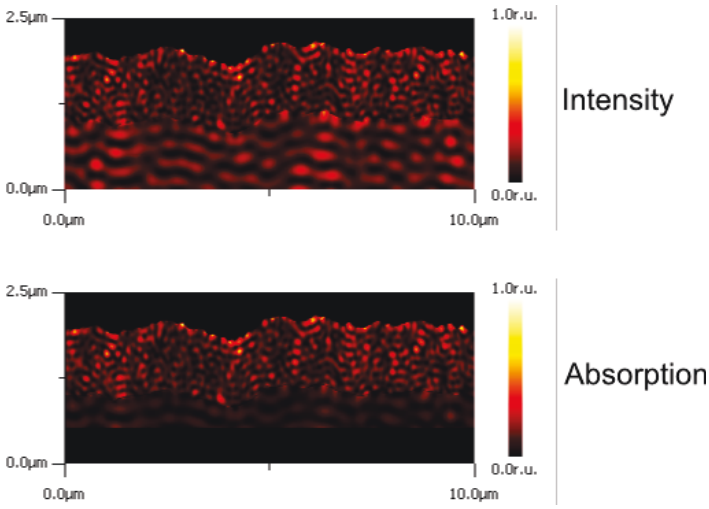

Figure 4.2.: Comparison of intensity distribution and absorptance for a single slice of a three-dimensional simulation at a wavelength of 800 nm. While intensity is visible in glass (bottom-most layer), front TCO (middle layer) and µc-Si:H (top-most layer), only the front TCO and µc-Si:H show absorption due to the assumption of $\epsilon_{i,glass} = 0$.

defined as $I_0 = \epsilon_0 c \sqrt{\frac{1}{\epsilon}} |E_0|^2$, and S_{domain} is the surface area of the domain perpendicular to the incident wave. This quantity is typically $10\mu m \times 10\mu m$ in this thesis.

4.4 ABSORPTION PLANES

Since the goal of this thesis is to correlate the absorption inside a layer with local texture features, an additional analysis method was developed to investigate this special question. While the results of the simulation are three-dimensional arrays, the amount of data in these arrays is far too much to correlate directly with the surface structures found on our TCO textures. An single value, such as absorptance or even EQE, however, lead to a loss of information for most of the structure. These quantities only allow for correlations between overall distribution of surface features with total performance of the cell. These correlations hardly result in scientifically stable conclusions and reflects more of a trial and error approach to optimising structures.

Therefore, a new approach is proposed in this thesis to reduce the three-dimensional absorption distribution inside a layer to a two-dimensional map of absorptions, which is easier to comprehend and compare to the also two-dimensional height map of a typical texture scan. For this approach, the ab-

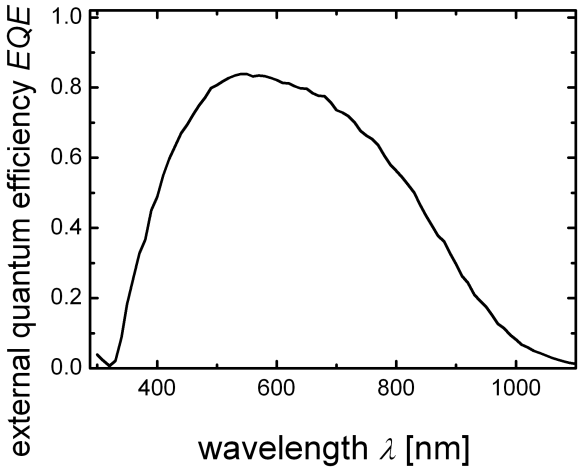

Figure 4.3.: Sample EQE of a typical 1.5 µm thick textured µc-Si:H single junction cell. The cell absorbs light in a wavelength region between 300 nm and 1100 nm, with the highest EQE at around 500 nm.

sorption inside a layer is integrated in the propagation direction of the incident light or, mathematically:

$$P_A(x,y) = \int_{z_i} A(x,y,z)dz. \tag{4.6}$$

A schematic of this algorithm is shown in Fig. 4.4, with a cross-section of the simulated absorptance (a), and the integrated absorption along this cross-section (b). Figure 4.4(c) shows the resulting absorption plane for the whole three-dimensional system, with the equivalent of (a) and (b) marked as a dotted line.

A comparison of this two-dimensional array with the original texture can give a good insight into the effects of local features on absorption inside a layer, provideda they exist. Examples of this are shown in Fig. 4.5 and Fig. 4.6 for cases of stronger and lesser resemblences between texture and absorption plane, respectively. The main difference in these two cases is the thickness of the layer, which the algorithm was applied to. The example showing similarities between surface and absorption planes (Fig. 4.5) has a very small layer thickness and a high absorption, so there is little light scattering after transmission through the textured interface and therefore a the general shape of the texture is still visible in the absorption plane, with the Si-layer above the crater rims showing the lowest absorption, while inside the craters, the absorption plane shows interference patterns due to light scattering. For the case of little resemblance (Fig. 4.6), the correlation is much worse, which in this case is due to a thick layer and a low absorption coefficient. As can be seen with these examples, this analysis method allows for better argumentation when

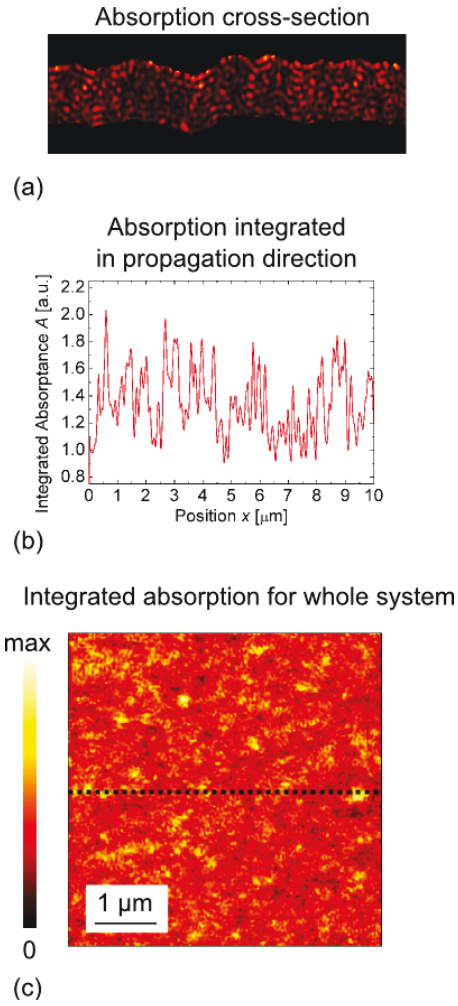

Figure 4.4.: Sketch of the algorithm used for calculating "absorption planes". The absorption for each point is integrated along the propagation direction of the light. As an example, this is shown for one slice of the three-dimensional simulation (a), with the integrated absorption at each point shown in plot (b). Doing this for all points of a layer results in a distribution as shown in (c).

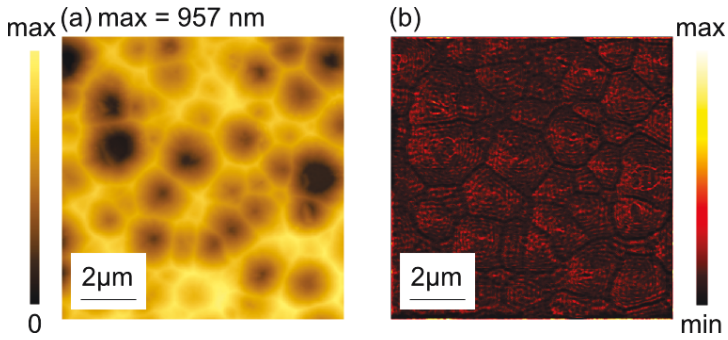

Figure 4.5.: Example of an absorption plane (b) showing the crater rims of the original texture (a). In this example, a 300 nm thin a-Si:H layer was simulated on top of the texture. Due to the small thickness, the correlation between topography and absorption plane is still clearly visible. Additionally, at the simulated wavelength (450 nm), the absorption of the a-Si:H is high enough so that the light is not reflected again at the back side, so no influence of the back side texture is visible.

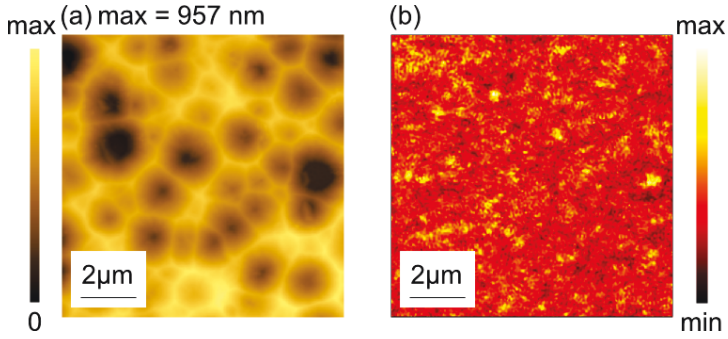

Figure 4.6.: Example of an absorption plane (b) showing little resemblance to the original texture (a). In this example, a 1 µm thick µc-Si:H layer was simulated on top of the texture at a wavelength of 800 nm. Due to the small absorptance, the light passes through the µc-Si:H layer multiple times, with the light being scattered each time it reaches one of the interfaces. Additionally, the large thickness reduces correlation between the layer boundaries due to scattering into large angles, so effects of surface features can influence the absorption at positions beyond the vicinity of the features. While the features in absorption are harder to correlate to a certain surface feature, this can lead to better understanding of the absorption in the layer.

discussing the quality of surface features for absorption in solar cells, for the absorption plane and surface texture can be directly compared.

4.5 SPECTRAL HAZE

A often used quantity to judge the quality of a textured surface in respect to light scattering is the spectral haze, which is defined as the fraction of light intensity scattered into angles above $0°$, divided by the total transmitted light intensity, or

$$H = \frac{I_{diff}}{I_{diff} + I_{spec}}, \tag{4.7}$$

with I_{diff} and I_{spec} being the diffusely and specularly scattered intensities, respectively. This spectral haze can be calculated for transmission as well as reflection.[45]

4.6 ANGULAR INTENSITY DISTRIBUTION

With light scattering being of crucial importance for the performance of a thin-film solar cell, another quantity is needed to describe it. One quantity often used for this is the spectral haze, as introduced earlier (Sec. 4.5), the fraction of the total transmitted/reflected light which is scattered into angles $> 0°$. However, this single value yields little information[46], since it does not distinguish between light scattered into an angle of $5°$or into an angle of $65°$.[47] The haze would be the same for both cases, with the latter case likely being much more beneficial for solar cell performance. This, however, depends on the exact layer stack and interface textures. Therefore, light scattering will be investigated mainly using the so-called angular intensity distribution (AID), discussed in detail in [48], which shows the amount of light scattered as a function of the angle into which the light is scattered. An example for this is shown in Fig. 4.7.

This quantity is calculated from a two-dimensional array of the electric field (FDTD) or phase (PM) from the plane of interest†. This calculation is done using a Fast Fourier Transform (FFT), with the result including both the AID and the light scattered into evanescent waves[49, 50]. If only the AID is of interest, limiting this result to the propagating part yields the AID.

The resolution of the AID depends on two factors: Firstly, the size of the area used in the FFT, and secondly the refractive index of the material in to which light is scattered. The latter is defined by the sample details, while the former can be increased by measuring a larger area for PM calculations. However, for FDTD simulations, the are is limited to $10\mu m \times 10\mu m$ due to limitations in resolution of the surface measurement as well as limitations in the simulation software.

† usually perpendicular to light propagation

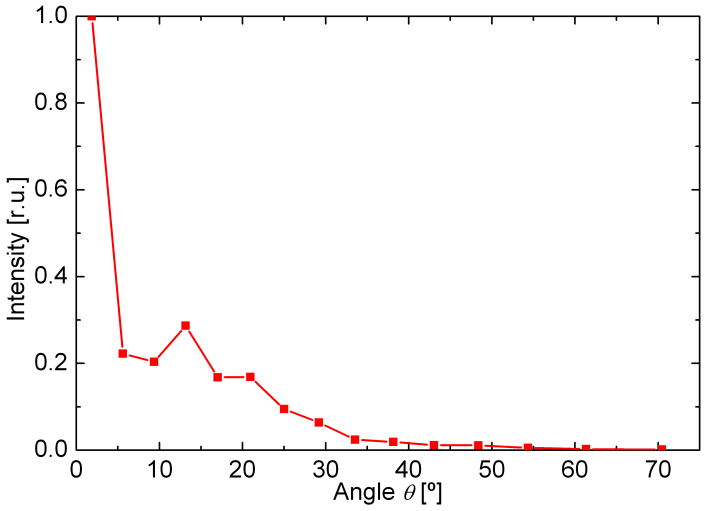

Figure 4.7.: Example of a calculated AID, which is equivalent to angular resolved scattering measurements (Sec. 5.2) for a textured ZnO:Al layer at an ZnO:Al/air interface at a wavelength of 700 nm. This is an example calculated from PM, using a wet-etched ZnO:Al layer as input. However, since the AID is calculated from a FFT, its resolution is limited by the area over which the FFT is performed and the refractive index of the material into which the light is scattered. The low angular resolution is an effect of the comparably small sample area ($10\mu m \times 10\mu m$) and the small refractive index of the material ($n \approx 1.7$).

5

EXPERIMENTAL METHODS

As final chapter of the fundamentals, it is necessary to introduce the experimental set-ups which were used during this thesis. The first and most important is the atomic force microscope, which was used to obtain the topography data for all real interfaces which were used in simulations. Afterwards, the measurement of angular resolved scattering will be explained, since it proved a valuable tool to investigate light scattering properties of different surface morphologies. The last experiment introduced is the scanning near-field optical microscopy, which is used to investigate near-field effects of structured surfaces. This last experiment was also to be modelled using simulations, with the results of this work being shown in Chap. 8.

5.1 ATOMIC FORCE MICROSCOPY

The most important experimental method utilised in this thesis is the atomic force microscopy or AFM[51]. It is used to obtain information about the surface morphology of a sample with a sub-nanometer resolution in height, and a lateral resolution of a few nanometres[51]. The principle is illustrated in Fig. 5.1, taken from [52].

A scanning probe with a very small tip radius mounted on a cantilever is used to scan across the surface of the sample. This scan can be performed in several ways, with the three most common described here:

- Scanning in "contact mode": In this mode, the tip is pulled over the surface of the sample. This leads to a high z-resolution, but the physical contact results in a degradation of both the tip and the sample. This means that not all materials are suitable for this approach.[52]
- Scanning in "non-contact mode": This measurement is performed with a feedback-loop, exciting the tip at a given frequency to induce small variations in the tip position. Since the strength of the forces between surface and probe are strongly dependent on the distance, the frequency will be shifted when the tip is close enough to the surface. Using appropriate electronics and software, the height of the sample at any given point can be calculated.[52]

In both cases, the cantilever on which the probe is mounted is flexed depending on the height of the sample at a given measurement point. A laser is

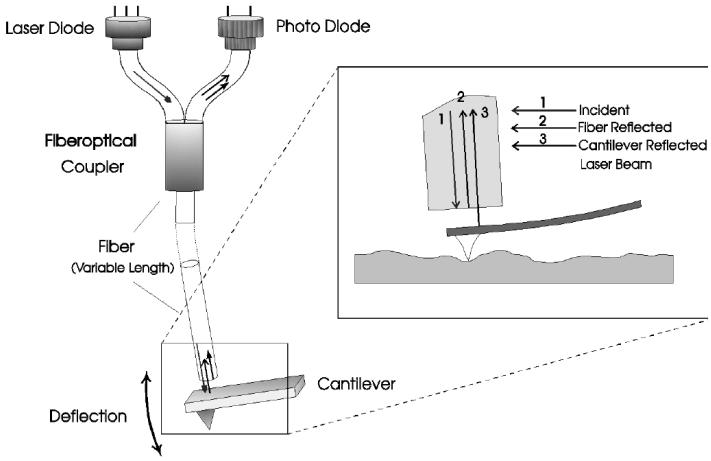

Figure 5.1.: Working principle of the AFM: A very fine tip (typical tip radius: 10 nm), which is mounted on a cantilever, is either pulled over a surface in contact mode or kept at a certain distance, both using a feedback system. The cantilever is illuminated by a laser, and the reflection measured with a spatially resolved detector. Due to the flexing of the cantilever and the resulting shift in the position of the reflection on the detector, the position of the tip can be calculated.[52]

deflected off the back of this cantilever and the reflection is measured via interferometry. The flexing of the cantilever changes the signal, so the position of the tip can be calculated from this position. This is also illustrated in Fig. 5.1, taken from the manual of the AFM used in this study[52]. Additionally, a feedback system modifies the z position of the tip based on the interferometry signal using a piezo.

5.2 ANGULAR RESOLVED SCATTERING

To investigate light scattering of a surface, which is the central point of Chap. 6, the AID was the analysis of choice. The equivalent experiment for comparison is the angular resolved scattering, or ARS, discussed in detail in the PhD thesis of M. Schulte[48]. It has been used to quantify the quality of textures for thin-film solar cells before[46], and has proven a reliable tool. Essentially, a photo diode is mounted on a moveable arm that can be rotated around a central point, at which the sample is located. This sample is illuminated with a laser of a specific wavelength, with the optical axis being perpendicular to the sample plane. By moving the detector arm around the sample, the scattered light intensity can be measured for any angle, both in transmission and reflection, with the limits being the path of the incident light. A sample graphic of this measurement is shown in Fig. 5.2. Additionally, corrections are necessary due

to the finite size of the detector. The details of this experiment have been discussed in [53, 48].

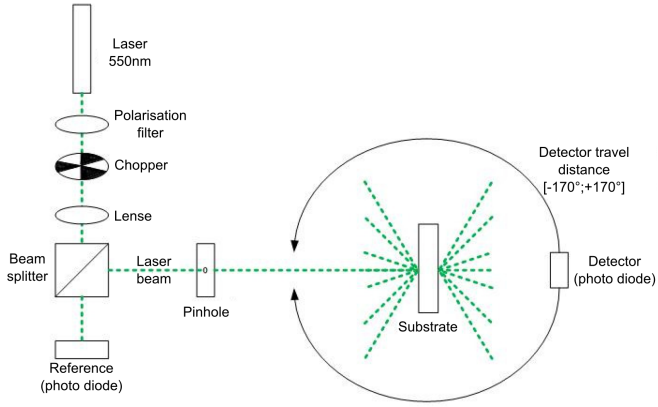

Figure 5.2.: Working principle of the ARS measurement: A sample is illuminated using a laser, and a detector moves around the sample at constant distance, measuring light intensities at different angles. These result in an angular distribution of measured intensities, both in transmission and reflection. Illustration taken from [53].

5.3 SCANNING NEAR-FIELD OPTICAL MICROSCOPE

The last experiment introduced is the scanning near-field optical microscope or SNOM[54]. The SNOM, as AFM, uses a scanning probe to investigate samples at a lateral resolution beyond the wavelength of the incident light (Abbe limit,[55]). In contrast to the AFM, however, using a metal coated glass fibre tip enables the SNOM to measure collected light intensity as well as topographical information. The principle of this set-up is shown in Fig. 5.3. The SNOM used for this thesis was purchased and modified, with the setup described in [54] as a template. This set-up uses probes with an aperture, fabricated from glass fibres and coated with a metal layer. For the investigations in this thesis, SNOM measurements were performed using collection mode; for this, the probe is illuminated with a laser and the light is collected locally through the probe. Since the probe can be positioned with a resolution of tens of nanometres, and in a distance of down to 20 nm above the surface, this can be used to investigate the near-field effects of a sample as well as propagated light.[49]

In both cases, however, the assumption of the probe being 20 nm over the surface at the measure point is not necessarily correct, as will be demonstrated in Sec. 8.1. The tip with an aperture has the additional disadvantage of a rather large size, since the aperture has to be large enough to collect or emit sufficient light for detection. Also, the metal coating adds to this thickness. An example

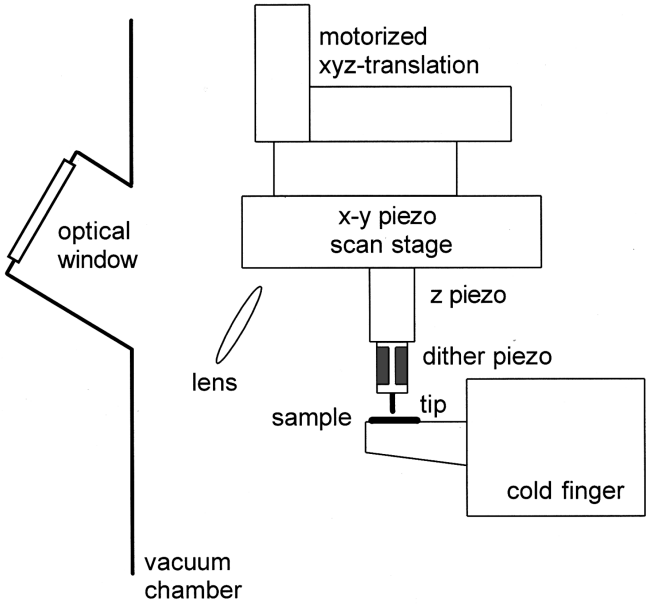

Figure 5.3.: Sketch of a typical SNOM system. The sample can be illuminated with lasers through the optical window and lens. The tip can be positioned using both motors for coarse and piezo elements for fine movement. The tip is kept at a constant distance above the surface using a feedback system based on a ceramic tuning fork. Illustration taken from [54].

of such a tip is shown in Fig. 5.4, which shows a scanning electron micrograph (SEM) of a typical SNOM tip.

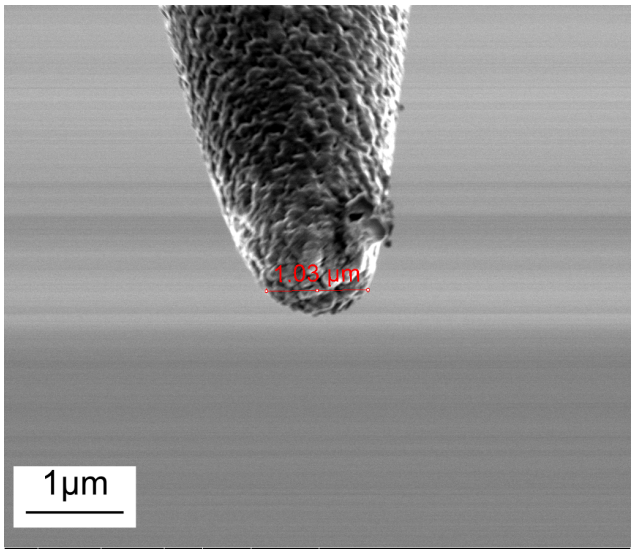

Figure 5.4.: SEM image of a SNOM tip. The shape is nearly conical, which will be used later on (Chap. 8). This example also shows a rather large tip with a thick metal coating and a total diameter at the front of about 1 µm.

Part II

RESULTS

6

FAR-FIELD SCATTERING

One of the most important and best ways to improve performance of Si-based thin-film solar cells is light scattering at different interfaces to increase the effective light path inside the absorber layer(s). In this first results chapter, the focus lies on this light scattering. Other works have shown the correlation between light scattering properties of textured front TCOs and cell performance[2, 31, 9, 32]. However, there is no detailed understanding of the exact mechanisms, making an optimisation of the structure difficult. Additionally, FDTD simulations are extremely time consuming, other approaches to investigate light scattering are looked at. The first part of this chapter compares the results of a recent model* at single interfaces with FDTD simulations to validate the results from this new model. The good agreement between both calculation methods for a single interface have lead to a more thorough investigation of the improved scalar scattering model and its predictive power for multi-layered systems, which it was not originally designed for.

6.1 FDTD VS. SCALAR MODEL

First investigations of light scattering properties in layers were focused on single interfaces between different materials using different interface morphologies to compare the calculated scattering properties as obtained by FDTD and an improved scalar scattering model[43], which has shown very good agreement with experiments, as investigated by various groups[56, 57, 58]. This model is referred to as the phase model (PM), and the comparison is composed of three major parts:

1. A comparison of the spectral haze: This is an integral quantity giving indicating how much light was scattered diffusely.
2. Comparison of the angular intensity distribution (AID) for two wavelengths exhibiting little and strong difference between the haze obtained by FDTD and PM.
3. A comparison of the intensity scattered into evanescent modes: This quantity is, in general, not easily accessible via far-field experiment and is included to show the major difference between the two mathematical approaches.

* introduced in the fundamentals part of this thesis, Sec. 3.2

The samples investigated consisted of textured transparent conductive oxides (TCO). For four of five samples, the materials at the interface were assumed to be ZnO:Al/air. The interface of the last sample was modelled to be ZnO:Al/µc-Si:H. The topographies of the samples, as obtained by AFM measurements, are shown in Fig. 6.1, while the simulated structure is shown in Fig. 6.2. The

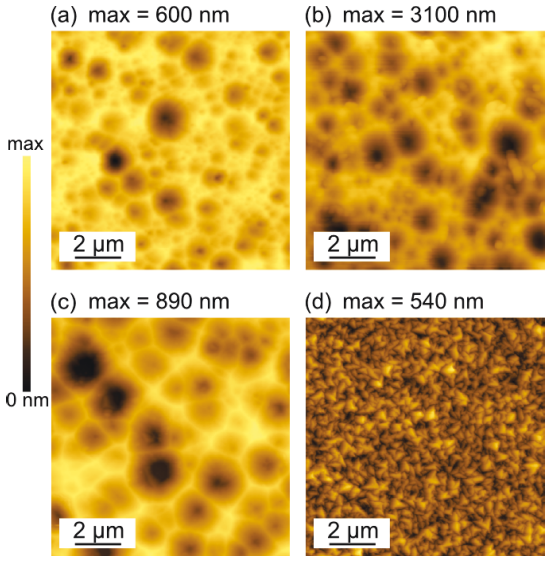

Figure 6.1.: Topographies of small feature sample (a) with heights up to 600 nm, stretched sample (b, heights up to 3100 nm), and large feature air and µc-Si:H sample (c) with heights up to 890 nm as measured by AFM. (d) shows the surface of the LPCVD-grown ZnO:B layer (heights up to 540 nm).

samples were prepared as following:

- A 30 setched ZnO:Al structure with a ZnO:Al/air interface ("small feature sample", Fig. 6.1(a)).
- An artificial structure created by stretching the height of a different 40 setched ZnO:Al surface by a factor of three to obtain steep flanks, interface materials ZnO:Al/air ("stretched sample", Fig. 6.1(b)).
- A 50 setched ZnO:Al structure with a ZnO:Al/air interface ("large feature air sample", Fig. 6.1(c)).
- The same texture with a ZnO:Al/µc-Si:H interface ("large feature µc-Si:H sample").
- A ZnO:B structure obtained by LPCVD, also with a ZnO:B/air interface ("LPCVD sample").

While the optical properties of the ZnO:B are different from those of the ZnO:Al, there are several reasons for using the same set of optical data as for the ZnO:Al samples. For one, differences in refractive index can be expected to be small, with differences in the extinction coefficient also being minimal. Also, the light scattering properties of the sample are dominated by the surface texture with the differences in optical data being so small. This combination of different surface morphologies and material combinations cover a wide set of parameters important for the light scattering. For both calculation methods, the same surface profile from AFM is taken as the input. The FDTD simulation was modelled with the "sample"-plane equivalent to the (flat) substrate surface. The texture was applied to a ZnO:Al layer on top of that surface. The incident light was modelled as a plane wave propagating in perpendicular to the sample-plane, linearly polarised in z-direction. The rigorous solution of Maxwell's equations by means of FDTD simulation used periodic boundary conditions. One of the major differences between FDTD and PM calculations is the fact that, while in the FDTD simulations, all materials are assumed to be absorbing as based on previously determined[4] optical data, the PM does not include absorption in any material. The resulting quantities of the PM and FDTD simulations are the phase shift as described in Sec. 3.2 and electric field of the incident wave modified by the topography, respectively. These complex functions are then used to calculate wavelength-dependent haze as well as AID and light intensity scattered into evanescent modes.

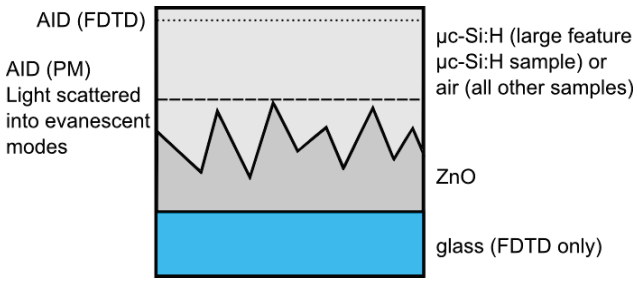

Figure 6.2.: Sketch of the system used in FDTD simulations. The dashed and dotted lines show the planes used for calculation of the AID (dashed: PM, dotted: FDTD) and light scattered into evanescent modes (dashed line).

The pupil function obtained by the PM is shown in the yz-plane at the absolute maximum of the texture, due to the nature of this model (see Fig. 6.2). Because the PM is used to ascertain the far-field scattering of a texture, the results of the haze and AID calculations are compared to FDTD simulations at a longer distance from the sample of about 3.5µm, whereas light intensity scattered into evanescent modes were calculated from the yz-plane at the absolute maximum point of the texture for both models.

Figure 6.3(a) shows the AFM image of the large feature air sample. It exhibits the typical crater-like structures of randomly distributed sizes. Figure 6.3(b) displays the real part of the pupil function obtained by PM for the

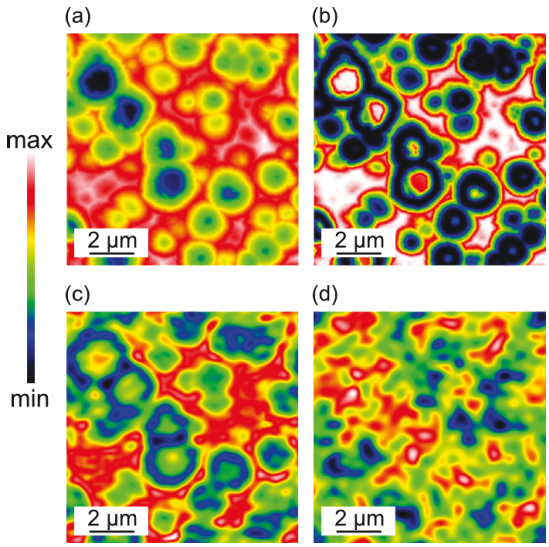

Figure 6.3.: Topography, PM and FDTD results for the large feature air sample: Original topography (a), real part of the pupil function as obtained by PM (b), real part of the electric field in polarisation direction obtained by FDTD at the highest peak of the topography (c) and 3.5 µm above the surface (d). All calculations were performed at a wavelength of 600 nm.

large feature air sample. The real part of the electric field is shown at the absolute maximum of the topography and 3.5 µm above that position in Fig. 6.3(c) and (d), respectively. Both the pupil function of the PM and the electric field at the top of the topography reflect the shape of the topography. The electric field obtained by FDTD far away from the surface, however, shows little resemblance with the topography.

The first comparison between both models will be performed for the spectral haze.

6.1.1 *Spectral haze*

The haze of all five samples was calculated for wavelengths between 300 nm and 1300 nm in 50 nm steps. Figure 6.4(a) and (b) show the results from both models for the small feature and large feature air sample, respectively. While for both samples a nearly perfect agreement is found, there is a slight difference for the small feature air sample at 300 nm which results from numerical errors in the FDTD simulation; due to high absorption in the ZnO:Al layer at 300 nm, which is included in FDTD simulations, the transmitted light intensity is very small. This intensity cannot be resolved in the FDTD simulation due to numerical limits. Therefore, the intensity used to calculate the haze is essentially a numerical artefact. Since the PM does not include absorption in

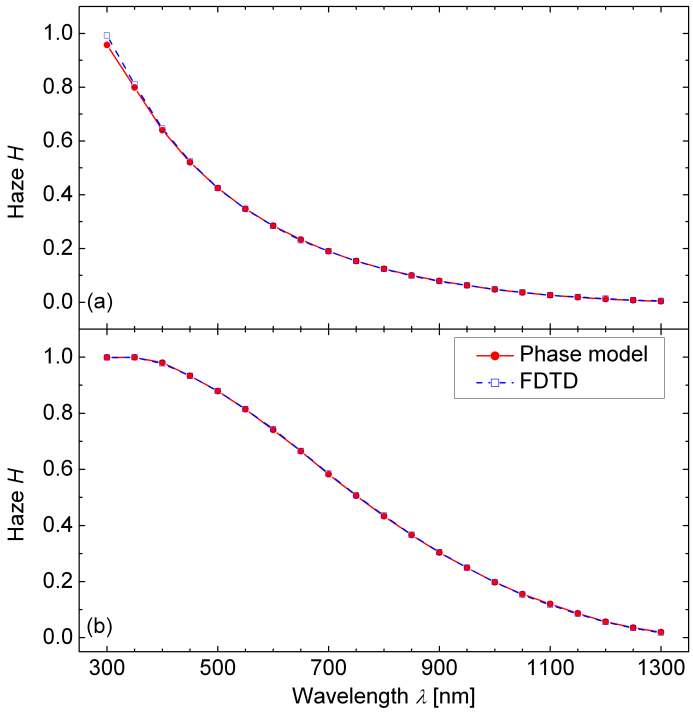

Figure 6.4.: Spectral haze of the small feature (a) and large feature air (b) sample calculated from PM and FDTD. Both models show an excellent agreement.

the TCO layers, a haze value can be calculated for this wavelength. But due to the aforementioned results from FDTD, a comparison is not feasible.

Figure 6.5(a) and (b) show the spectral haze calculated for the large feature µc-Si:H sample and the stretched sample, respectively. Again, the haze calculated with both methods shows good agreement for the most part of the spectrum. However, there is a small but clearly visible difference between PM and FDTD between 700 nm and 1250 nm for the large feature µc-Si:H sample and between 850 nm and 1200 nm for the stretched sample, resulting in a higher haze in the PM.

For the LPCVD sample (Fig. 6.6 the haze calculations by FDTD and PM show very good agreement, with a visible deviation between 400 nm and 800 nm. The largest difference is visible at a wavelength of 600 nm.

Overall, a higher refractive index difference (large feature µc-Si:H sample) or steep flanks on the surface (stretched and LPCVD sample) lead to a stronger difference between PM and FDTD.

A deeper investigation of this difference will be discussed in the next section by looking at the AID. Since the haze is calculated by the integrated diffuse intensity and the specular intensity, changes in the AID influence the haze.

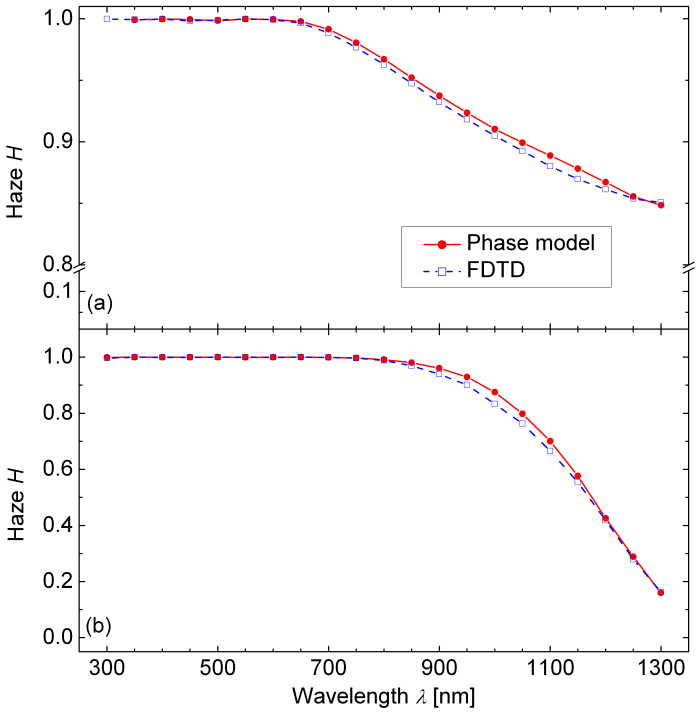

Figure 6.5.: Spectral haze of the large feature µc-Si:H (a) and stretched (b) sample. Both models show a very good agreement, but with visible differences between 700 nm and 1250 nm (a) and between 850 nm and 1200 nm (b).

This is caused by the fact - as explained in Sec. 4.6 and Sec. 4.5 - that the AID and the spectral haze are interrelated. A change in the AID can lead to a larger or smaller fraction of the light being scattered into angles beyond 0°, resulting in a larger or smaller haze, respectively.

6.1.2 *Angular intensity distribution*

Now, the AID of all samples is investigated for wavelengths of 600 nm and 1000 nm, obtained by both models. For comparison with the haze values calculated in the previous section, the first point of the AID is assumed to be the specular portion of the transmitted light intensity. However, this is only an approximation, since, depending on the angular resolution, this value also includes a portion of the light intensity scattered into small angles. This is also valid for the haze calculations, as smallest angle of the diffusely transmitted intensity is limited by the resolution of the FFT. The calculations at 600 nm show a good agreement of haze values for all samples, while at 1000 nm, the strongest deviation of the large feature µc-Si:H sample and the stretched sample is found, with the PM exhibiting a higher haze. However, the LPCVD

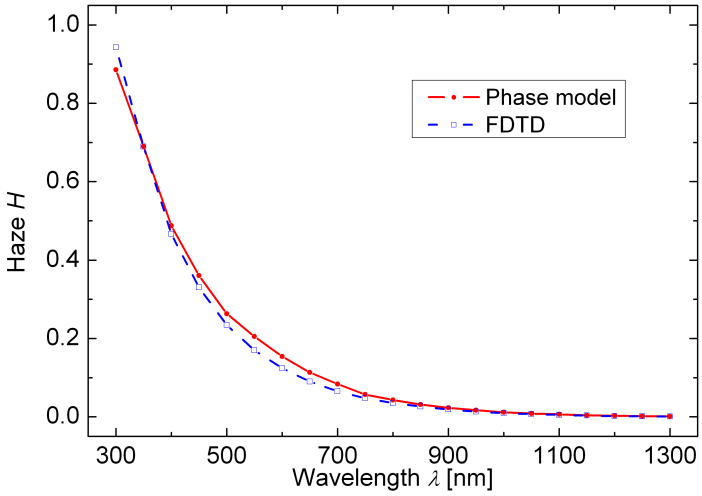

Figure 6.6.: Spectral haze of the LPCVD sample. Agreement between both models is again very good, with similar differences between the models as for the stretched sample, but shifted to shorter (400 nm to 800 nm) wavelengths.

sample showing the opposite behaviour: excellent agreement at 1000 nm and worse agreement at 600 nm. With the exception of the LPCVD sample, all graphs are normalised to their respective maxima. The LPCVD sample graphs are normalised to their values at 23° and 40.5° for 600 nm and 1000 nm, respectively. This is done because of the large difference of the first point of the AID; similarities in the scattering into larger would be harder to investigate.

Figure 6.7(a) and (b) show the AID for the small feature and large feature air samples, respectively. For both samples, the agreement of AID from PM and FDTD is nearly perfect, therefore validating the good agreement of the haze calculations as well. Figure 6.8(a) and (b) show AID calculated from PM and FDTD for a high refractive index difference (large feature μc-Si:H sample) and a topography with steep flanks (stretched sample), respectively, for wavelengths of 600 nm and 1000 nm. For the large feature μc-Si:H sample (Fig. 6.8(a)), the agreement between PM and FDTD is very good for both wavelengths, although haze calculations showed their maximum difference at 1000 nm.

The stretched sample (Fig. 6.8(b)) shows larger differences between PM and FDTD. Agreement for a wavelength of 600 nm is very good, with differences only visible at large angles. However, at a wavelength of 1000 nm, the values exhibit some differences while general trends in the curve are still similar for both calculations. Especially the difference in the first point, which includes the specular portion of the transmitted light, explains the difference observed in haze calculations.

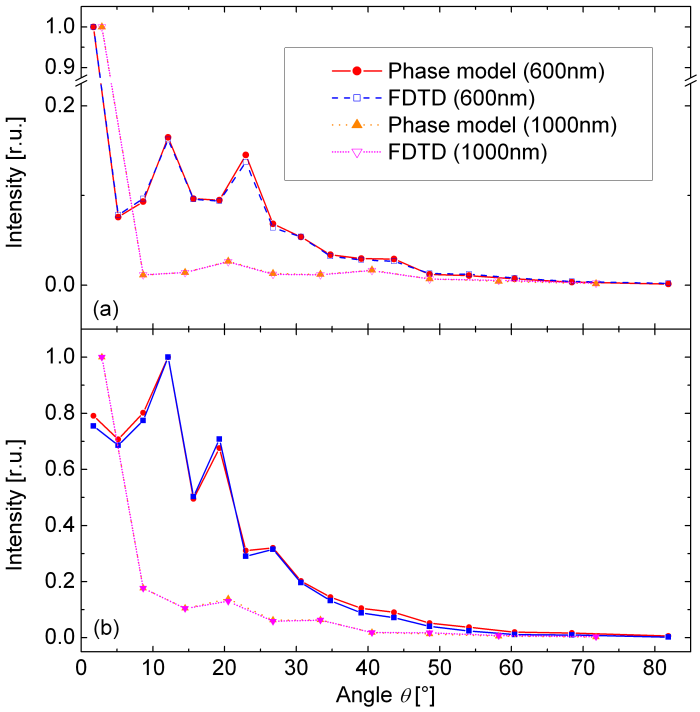

Figure 6.7.: Angular intensity distribution of the small feature sample (a) and large feature air sample (b), calculated using PM and FDTD. AID is shown for 600 nm and 1000 nm. All curves are normalised to their respective maxima.

Looking at the LPCVD sample (Fig. 6.9, we see an excellent agreement between the calculations of PM and FDTD for the diffuse part of the AID (angle $\alpha > 0°$) except for large angles at 600nm. Also, the PM calculation show a stronger specular peak (angle $\alpha = 0°$), agreeing with the haze calculations.

Overall agreement of AID calculations are very good, the AID of the large feature µc-Si:H and LPCVD samples show a good but not perfect agreement of AID calculations, similar to the agreement of haze calculations.

While the angular resolution is identical for both approaches, and therefore the amount of information gained from both models is identical for AID and haze calculations, a higher angular resolution can resolve the features of the AID better, resulting in a better comparison between both models.

A higher resolution, is only accessible through larger domains or a higher refractive index of the surrounding material, the first of which is not feasible due to the computational complexity of FDTD simulations; the time needed for calculation increases linearly with an increasing number of points, proportional to $n_x \cdot n_y \cdot n_y$, with n_x, n_y, n_z being the number of points in the respective direction. Using a material with a higher refractive index as ambi-

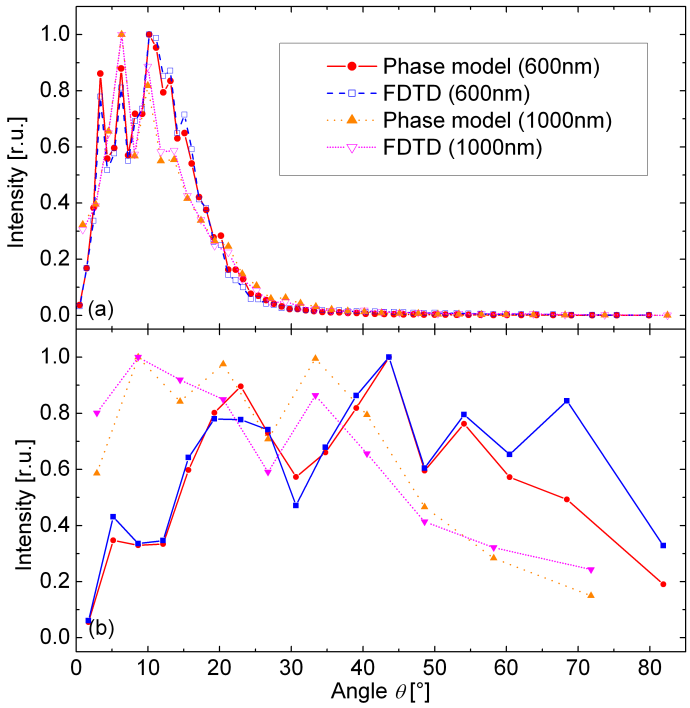

Figure 6.8.: Angular intensity distribution of large feature µc-Si:H sample (a) and the stretched sample (b). AID is shown for 600 nm and 1000 nm. Both curves are normalised to their respective maxima.

ent is presented in the large feature µc-Si:H sample, which also results in a higher angular resolution (s. also Sec. 4.6.

6.1.3 *Near-field effects*

To gain additional information about the predictive power of the PM, especially for light trapping investigations, the near-field effects (i.e. light scattered into evanescent modes) will also be checked for all samples at wavelengths of 600 nm and 1000 nm to examine the impact of the sharp features in the pupil function obtained by PM. Due to the nature of the evanescent modes, these are only visible very close to the surface.

In thin-film solar cells, these evanescent modes are of great importance,[49] since thicknesses and surface features are in a range in which near-field effects are present. In these models, however, a slice perpendicular to the propagation direction is taken into account. For the PM, this is the only accessible plane. To have a direct comparison between FDTD and PM, the equivalent plane is considered in FDTD simulations (see also Fig. 6.2).

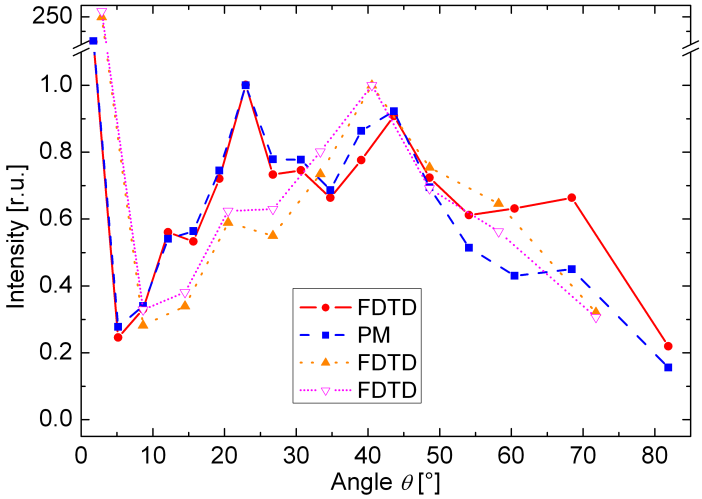

Figure 6.9.: AID of the LPCVD sample. The curves at wavelengths of 600 nm and 1000 nm are normalized to the values at 23° and 40.5°, respectively, with the PM showing a lower peak at 0°.

Figure 6.10(a) and (b) show the scattered light intensity as a function of the reciprocal lattice constant† of the small feature sample and the large feature air sample, respectively. The start of the evanescent modes, indicated by vertical dashed and dotted lines for wavelengths of 1000 nm and 600 nm respectively, shows an extreme overestimation of the evanescent part by the PM. Results of both samples show a faster decline of evanescent modes in FDTD, resulting in one to two orders of magnitude offset while the shape of the curve is very similar for both calculations.

Figure 6.11(a) and (b) show the light scattering of the large feature µc-Si:H sample and the stretched sample, respectively. The scattered light intensity exhibits the same behaviour as for the samples shown in Fig. 6.10, but with an even faster decline of the near-field modes for FDTD simulations. This results in an even larger difference between PM and FDTD of at least 1.5 orders of magnitude. Looking at the light scattered into evanescent modes of the LPCVD sample (see Fig. 6.12), we see the same trends with an even larger difference of up to 3.5 orders of magnitude. It is to be noted that both wavelengths of 600 nm and 1000 nm show nearly identical light scattered into evanescent modes when using the PM.

The reason for the difference between PM and FDTD lies in the nature of the PM. The evanescent modes decay exponentially with increasing distance from the interface. In FDTD simulations, this is taken into account, since it is a rigorous solution of Maxwell's equations. Looking at the pupil function obtained by PM, however, it is obvious that near-field effects cannot be described

† obtained by FFT and equivalent to the k-vector in momentum space

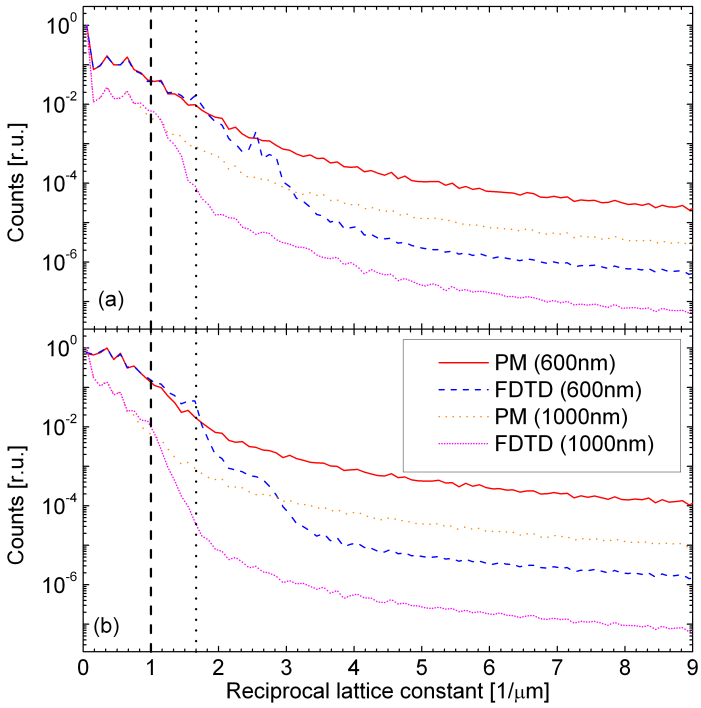

Figure 6.10.: Light scattered into evanescent modes for the small feature sample (a) and large feature air sample (b). The dashed and dotted vertical lines represent the beginning of the evanescent modes for 1000 nm and 600 nm, respectively.

correctly. Calculating the pupil function from a plane further away from the interface results in a constant phase shift of all points with respect to a plane at the maximum height of the topography. Using this new pupil function to calculate the intensity scattered into evanescent modes results in an identical distribution, so it does not depend on the distance from the surface, which contradicts the behaviour of evanescent modes. For features with steep flanks, this effect is very pronounced due to the large distance between the minima of the topography and the actual position of the plane from which the light scattering is calculated in the PM. A high-index material at the transmitted side of the interface shows very similar behaviour; while the distance between the actual height of the topography is the same as for a low-index material, the high refractive index leads to a much faster decay of evanescent modes. This explains the difference between PM and FDTD in these cases and demonstrates that the PM cannot be used for investigations of near-field effects.

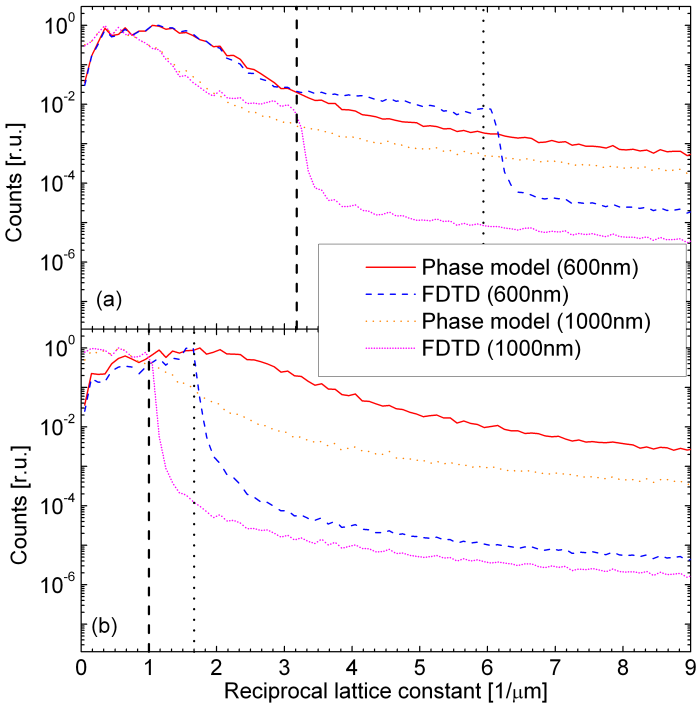

Figure 6.11.: Light intensity scattered into evanescent modes for the large feature μc-Si:H sample (a) and stretched sample (b). The dashed and dotted lines indicate the beginning of the evanescent modes for 1000 nm and 600 nm, respectively.

6.1.4 *Remarks about the use of the phase model*

As was shown in this section, the PM is a powerful tool to estimate the scattering properties of different surface types for different material combinations. This can be used as a test to see if FDTD simulations, which can be very time consuming, are justified.

However, a rigorous solution of Maxwell's equations is necessary for the optical modelling of a solar cell device. First of all, the PM is limited to a single interface. But there are several interfaces in a typical solar cell, which lead to different and/or additional scattering as well as interferences. With some of the layers in these systems being only a few nanometres thick, near-field effects also play a role. And finally, each layer in a solar device exhibits absorption, which is crucial for the cell, whereas the PM does not include any absorption at all.

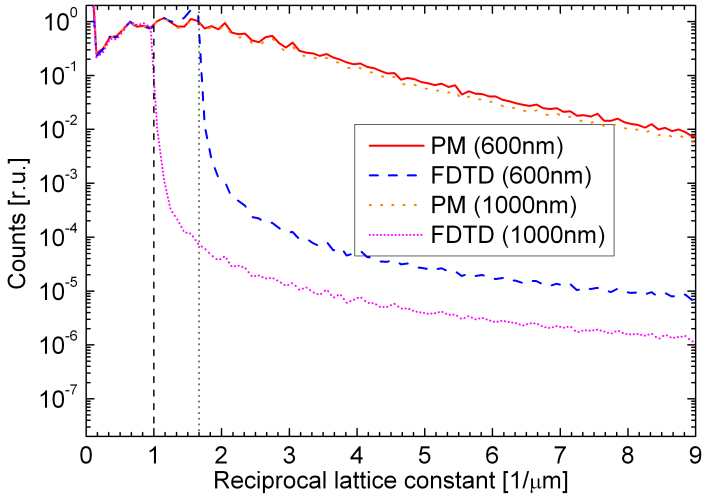

Figure 6.12.: Light intensity scattered into evanescent modes for the LPCVD sample. The dashed and dotted vertical lines indicate the beginning of the evanescent modes for 1000 nm and 600 nm, respectively.

6.2 SCATTERING AT FLAT FRONT SIDE AND TEXTURED BACK SIDE

To gain more insight into the light scattering properties of the front and back side texture of a microcrystalline silicon solar cell and its impact on the cell performance, a series of samples was created, which included very different surface morphologies. In total, three different substrates were used:

- A 6s wet-etched ZnO:Al substrate; the short etching time leads to fewer, very small (300 nm) craters and is generally not considered to be a good light scatterer. (Fig. 6.13(a))
- A 40s wet-etched ZnO:Al substrate; this substrate exhibits crater-like structures with varying radii and depths, and has been shown to be beneficial for light trapping[2, 31]. (Fig. 6.13(b))
- A commercially available SnO_2:F based Asahi-U type substrate; this substrate is dominated by small pyramid-like structures and is a common substrate for thin-film silicon solar cells. (Fig. 6.13(c))

On each substrate, a nip-type μc-Si:H cell was deposited, consisting of an Ag/ZnO:Al back contact. The nip-stack consisted of 20 nm n- and p-doped layers surrounding a 2300 nm thick intrinsic μc-Si:H layer. 80 nm of ZnO:Al was used as a front contact. AFM measurements were taken after deposition of the back contact, shown in Fig. 6.13, and after the deposition of the nip-stack, shown in Fig. 6.14, at the same spot on the sample.

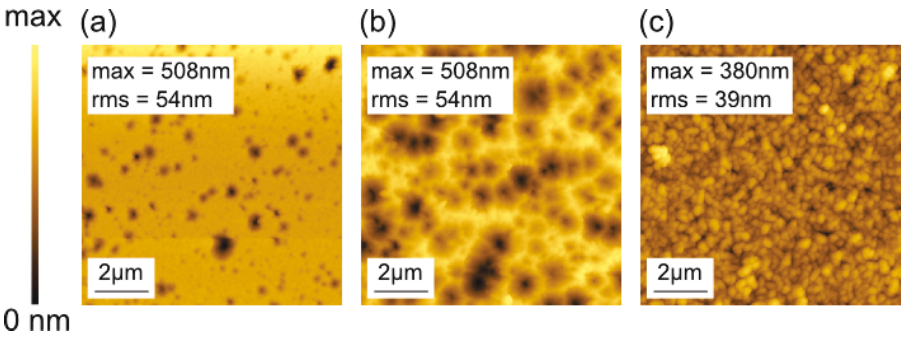

Figure 6.13.: Textures of the different substrates used for sample preparation. A 6 s etched ZnO:Al (a), a 40 s etched ZnO:Al (b) and a commercial Asahi-U type substrate (c). The 6 s etched ZnO:Al shows isolated craters of sizes between 50 nm and 500 nm, with only a small rms roughness. The 40 s etched ZnO:Al substrate exhibits many creates, most of them adjacent to each other, with sizes between 200 nm and up to 2000 nm. The peak-to-peak roughness is 842 nm and the rms roughness 140 nm. The Asahi-U type structure exhibits many pyramid-like structures, with a maximum height of 380 nm and a rms roughness of 39 nm.

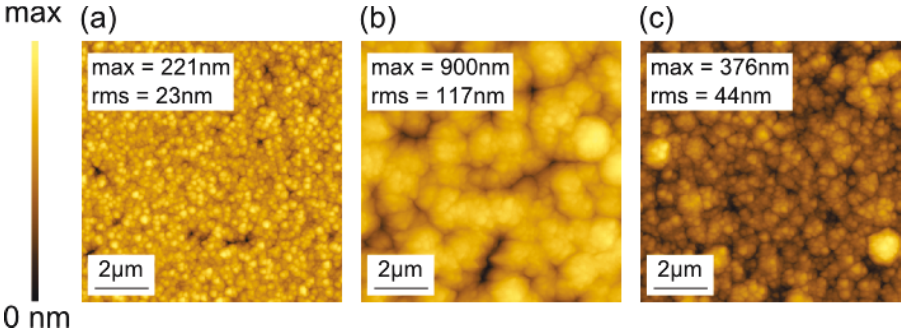

Figure 6.14.: Textures of µc-Si:H cells deposited on the different substrates with a thickness of 2300 nm. For all three depositions, the growth of the crystallites can be seen. For the 6 s etched ZnO:Al (a), the rms roughness is reduced, while the surface structure shows the small crystallites and retaining some of the larger craters. For the 40 s etched ZnO:Al (b), The large craters from the previous AFM scan (Fig. 6.13(b)) are still visible while much of the structure has been changed by the µc-Si:H growth. The same is true for the Asahi-U structure (c), where distinct features, as the "bulges" at the left and right side of the scan, are still visible. However, the structure shows more similarities with the original AFM scan (Fig. 6.13(c)).

To ascertain the light scattering and its impact on performance, both reflection AID and EQE measurements were taken. However, since the AID measurements are influenced by both textures, parts of each cell were polished by an external company to obtain a flat front side. In total, approximately 700 nm of material were removed, resulting in a smoother front side texture. To ascertain the quality of the polishing, additional AFM measurements were performed, the results of which are shown in Fig. 6.15. Due to the fact that the front contact and p-doped layer were also removed, a new, identical front contact was deposited on the polished parts of the sample.

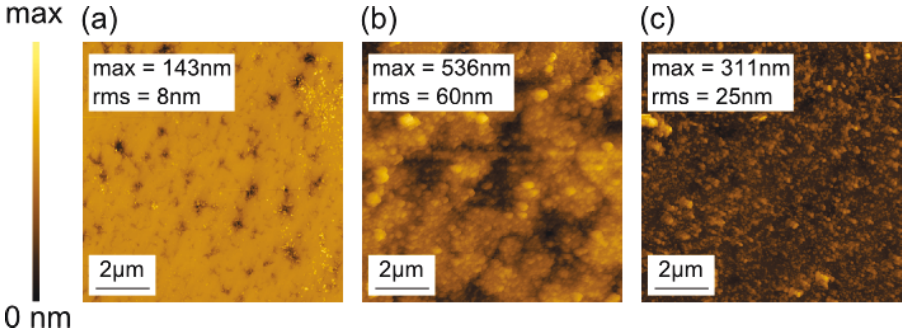

Figure 6.15.: Samples after polishing. The polishing of the 6 s etched ZnO:Al substrate (a) shows the best results with a remaining rms roughness of 8 nm and a peak-to-peak height of 143 nm. The 40 s etched ZnO:Al sample (b) still shows characteristic features of the original surface, which indicates a non-optimal polishing. The peak-to-peak height was reduced to 536 nm and the rms roughness was reduced to 60 nm. The Asahi-U type sample (c) exhibits a smoother surface with a rms roughness of only 25 nm, while peak-to-peak height remained at a relatively high 311 nm. This can be attributed to a small number of high features, possibly remains of the polishing or AFM artefacts.

As can be seen in the AFM scans, the polishing was not perfect, with the best results obtained for the shortly etched ZnO:Al(Fig. 6.15(c)). For the other systems, the reduction in roughness was less, but still very significant. The overall roughness was reduced as follows:

- 40s wet-etched substrate: The rms roughness was reduced from 117 nm after deposition of the nip stack to 60 nm (Fig. 6.14 and 6.15(a)).
- 6s wet-etched substrate: rms roughness was reduced from 23 nm to 8 nm (Fig. 6.14 and 6.15(b)).
- Cell deposited on the Asahi-U type substrate: Roughness went from 44 nm after deposition of the nip stack to 25 nm after polishing (Fig. 6.14 and 6.15(c).

This leads to a set of six samples: Three substrates with a polished and unpolished front contact. An overview of the modelled systems is displayed in Fig. 6.16.

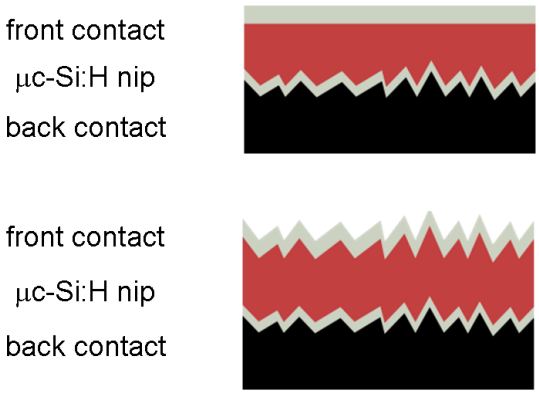

Figure 6.16.: Sketch of the model used for FDTD simulation. (a) shows the sample after polishing, with a reduced average thickness of the absorber layer and a flat front contact. For the real device, this is only a rough approximation, as indicated by the AFM scans after polishing (Fig. 6.15). The unpolished sample is sketched in (b). The interfaces assumed at the back side are shown in Fig. 6.13 and the front side texture assumed for the non-polished samples in Fig. 6.14.

The results of the different measurements and simulations will be presented step-by-step with a final discussion of the interdependance of the different results.

6.2.1 *AID measurements, PM and FDTD*

Firstly, the AID measurements will be compared to the different simulation approaches at different interfaces (PM) or differet stack configurations (FDTD).

The AID measurement can only reflect the response of the whole system, with either the front side texture (FST) and back side texture (BST) (unpolished) or BST and near-flat FST (polished). However, for the FDTD simulations, the front side of the polished samples is assumed to be perfectly flat. For the PM, any measured interface can be taken into account.

When looking at the AID of the unpolished cells (Fig. 6.17), measurements performed at a wavelength of 532 nm (black dots) were compared to FDTD simulations (blue, solid line) and PM in reflection at the front side, taking into account the front side texture (Fig. 6.14).

For all three samples, the unpolished cell shows good agreement between the experiment and either simulation method. Looking at small scattering angles, FDTD and PM show excellent agreement, while at larger angles, there are significant differences - especially for the wet-etched samples. With the previously shown excellent agreement between PM and FDTD and the fact

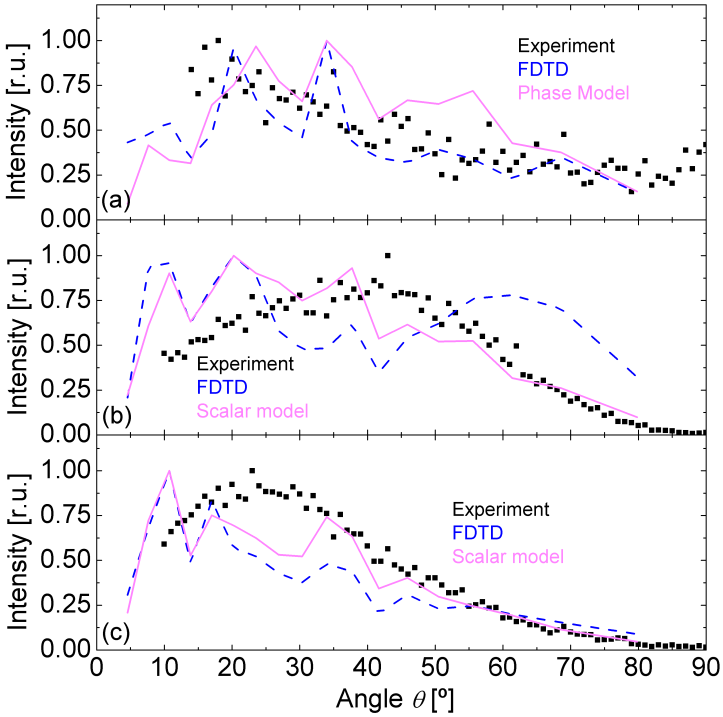

Figure 6.17.: AID in reflection of the unpolished samples deposited on 6 s etched ZnO:Al (a), 40 s etched ZnO:Al (b) and Asahi-U (c) at a wavelength of 532 nm. FDTD simulations consisted of measured back side texture (Fig. 6.14) and front side texture (Fig. 6.13). For PM calculations, only the front side texture is considered. Agreement between experiment and FDTD simulation is good for all samples, except for the large angle portion of the 40 s etched ZnO:Al substrate. Agreement with PM is also very good.

that the PM only takes into account the front side texture, it is assumed that the difference at large angles result from an influence of the back side texture, albeit small due to the high absorption in the μc-Si:H layer. An additional influence, leading to significant differences between the experiment and FDTD simulations, is the fact that, while front interfaces are assumed to be perfectly flat in the simulation, this is not the case for the real samples, as has been shown in Fig. 6.15.

The polished sample, however, shows very different behaviour. The measured AID only shows good agreement with both simulation methods for the short etched ZnO:Al substrate. For both the long etched ZnO:Al and the Asahi-U type substrate, agreement is good with the PM, but FDTD simulations show very different results. When looking at the AFM scans of the textures (Fig. 6.15) after the polishing, it is apparent that the approximation of a perfectly flat front interface is only good for the short etched ZnO:Al substrate. Since agreement with PM - which takes into account the texture after polishing - is good

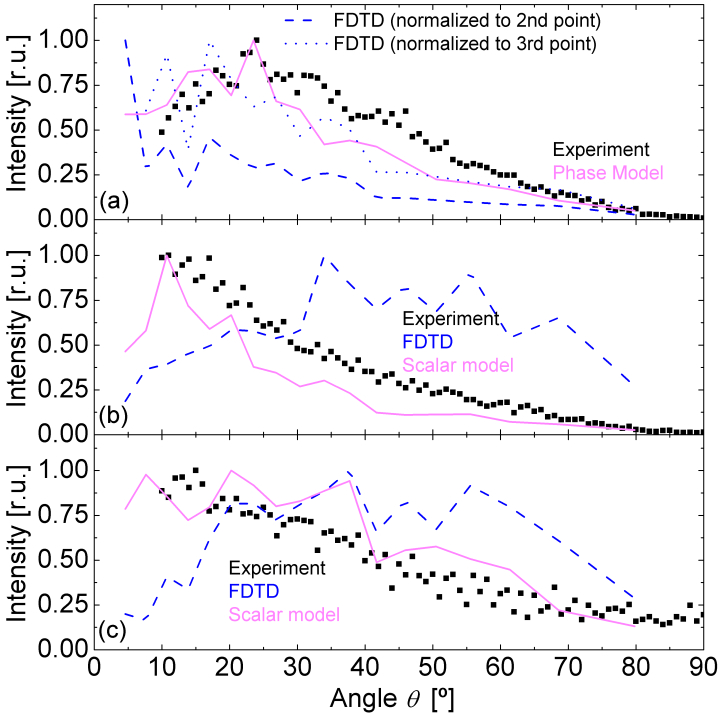

Figure 6.18.: AID in reflection of the polished samples deposited on 6 s etched ZnO:Al (a), 40 s etched ZnO:Al (b) and Asahi-U (c). Agreement between experiment and FDTD simulations is good for the 6 s etched ZnO:Al substrate, but much worse for the other two samples. while agreement with PM is good for all samples. With the only difference lying in the front side texture, this is the dominating influence on AID for short wavelengths.

(Fig. 6.18), it is safe to assume that at a wavelength of 532 nm, the reflection at the front side dominates the AID in reflection.

Since measurements could not be performed with a longer wavelength, investigations of the scattering properties in that wavelength region are limited to simulations using both PM and FDTD. The results of these simulations are shown in Fig. 6.19. Both results shown for PM were calculated in reflection, while the FDTD calculations consider the whole layer stack as closely to the real-life device as possible.

When looking at the 6 s etched ZnO:Al substrate (Fig. 6.19(a)), both simulation methods show stronger scattering into large angles. This agrees with other investigations in this area [31]. When comparing the two simulation methods, the PM indicates stronger light scattering into large angles than results of the FDTD simulations. This is likely to result from the combination of the light scattering in transmission at the front side and scattering in reflection at the back side, while results shown for PM only include the scattering properties of a single interface.

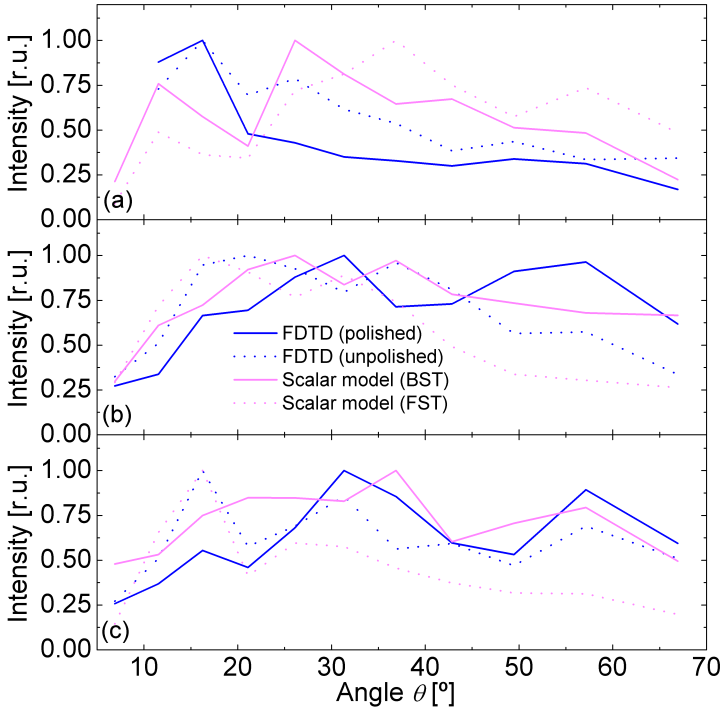

Figure 6.19.: AID for a wavelength of 800 nm as obtained by FDTD and PM for the 6 s etched ZnO:Al (a), 40 s etched ZnO:Al (b) and Asahi-U. For all samples, large angle scattering is apparently dominated by the back side texture, while small angle scattering is dominated by the front side texture.

The AID of the 40 s etched ZnO:Al substrate (Fig. 6.19(b)) exhibits better agreement between both models, especially when comparing the FDTD simulations with the PM results for the back side texture. However, in the small angle region of the AID, the front side texture appears to be stronger, as the FDTD simulation of the unpolished sample bears similarities with the PM results for both the front and the back side texture. Looking at the AFM scan of the sample after deposition and after polishing (Fig. 6.14 and 6.15(b)), this can also be explained by a worse polishing of the surface when compared to the 6 s etched ZnO:Al substrate (Fig. 6.14 and 6.15(a)).

The sample fabricated on the Asahi-U type substrate (Fig. 6.19(c)) shows similar results as the 40 s etched ZnO:Al sample; large-angle scattering is dominated by the back site texture, while small-angle scattering is strongly influenced by the front side texture.

6.2.2 *Quantum efficiency and absorptance enhancement*

After investigation of the light scattering influence of front and back side texture, we also investigated cell performance as a whole; EQE was measured

with a high bias voltage of 5 Vfor all six samples. In the FDTD simulations, the absorptance per area, which is proportional to the EQE, was considered for the polished relative to the unpolished sample. To have a beter comparison, the same relative value was calculated for the EQE measurements.

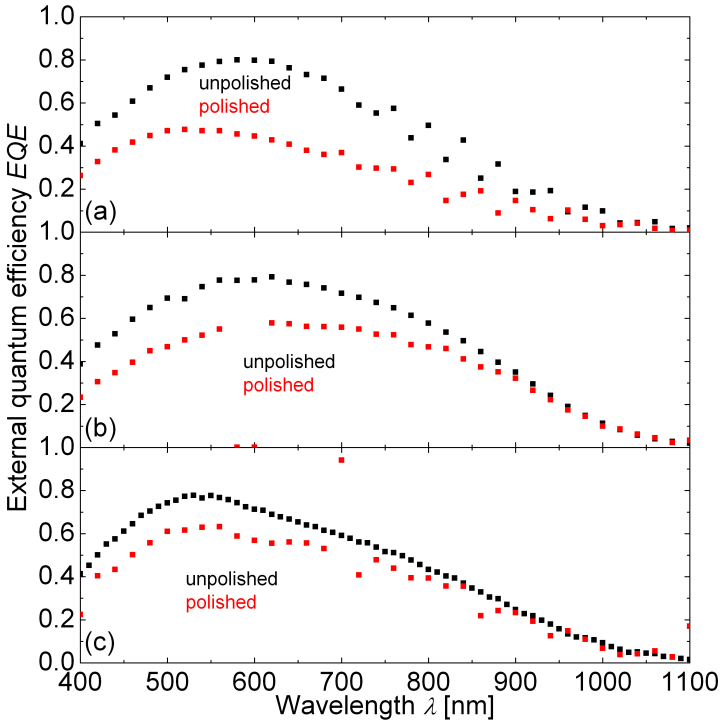

Figure 6.20.: Measured EQE of the unpolished (black) and polished (red) samples on 6 s etched ZnO:Al (a), 40 s etched ZnO:Al (b) and Asahi-U. For all samples, the EQE is strongly decreased by polishing for the short wavelength region. However, this effect is reduced at long wavelengths, indicating the influence of the front sided texture on cell performance in the short wavelength region. Additionally, the polishing has induced defects into the front contact, which also contribute to the reduced performance. For long wavelengths, however, the back side texture has a far stronger influence.

When looking at the measured quantum efficiencies, as shown in Fig. 6.20, a strong loss in EQE is visible at short wavelengths due to polishing. However, for longer wavelengths, the loss in EQE is significantly less pronounced or non-existent for the 6 s etched sample and both the 40 s etched sample and the Asahi-U sample, respectively. To pinpoint the main cause for this change in EQE, one has to compare the difference in EQE with the difference in absorptance obtained by FDTD simulations. The main difference between the two should lie in the electrical properties of the cell, since these are completely neglected in the FDTD simulations. The comparison of the EQE/absorptance difference between FDTD and measurement are shown in Fig. 6.21.

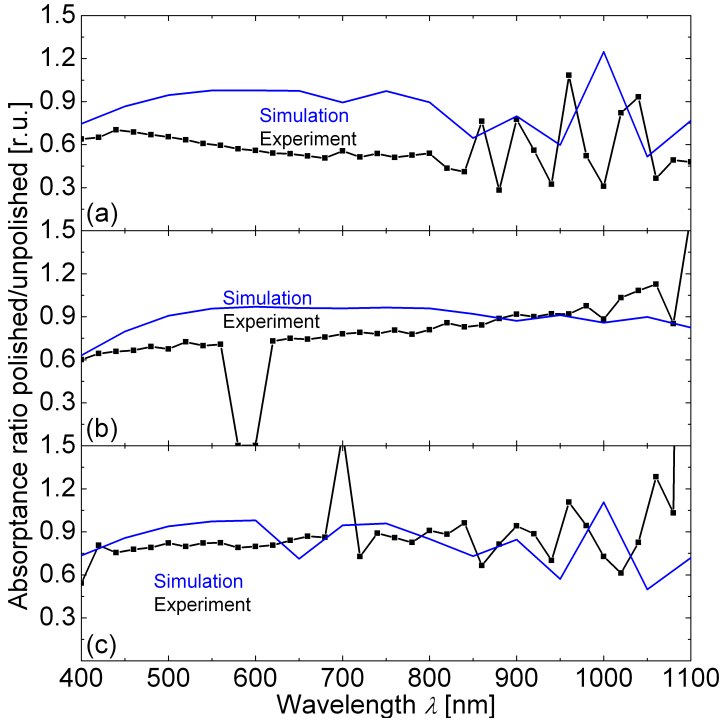

Figure 6.21.: Relative increase/decrease in EQE (experiment, black) and absorptance (simulation, blue) of the polished sample compared to the unpolished over wavelength for 6 s etched ZnO:Al (a), 40 s etched ZnO:Al (b) and Asahi-U. In the short wavelength region, simulation and experiment only agree for the Asahi-U cell, while for both ZnO:Al cells, agreement only gets better at longer wavelengths. This is attributed to the neglecting of electrical influences in the simulation and non-perfect polishing. At long wavelengths, agreement becomes better, indicating the dominance of the back side texture for cell performance at long wavelengths.

Looking at this comparison, it is obvious that the simulation significantly underestimates the effect in the short wavelength region between 400 nm and 800 nm for both ZnO:Albased samples (Fig. 6.21(a) and (b)). For the Asahi-U based sample, the agreement is much better, but still simulation underestimates the loss in QE. In the long wavelength region, the agreement for the rougher samples (40 s etched ZnO:Al and Asahi-U, Fig. 6.21(b) and (c), simulation and experiment show a good agreement, while the comparatively flat sample, 6 s etched ZnO:Al, Fig. 6.21(a), shows stronger differences while still showing the same trend.

6.2.3 *Conclusion*

The results obtained from AID measurements and calculations lead to the conclusion that in the short wavelength region, the front side texture is clearly dominant, since most if not all of the light does not reach the back side texture. However, as will be introduced later in Sec. 7.2, the front side texture has a strong influence on light incoupling, which influences absorption *especially* in the short wavelength region. In the long wavelength region, however, the back side texture is far more important for cell performance. This conclusion is supported by several facts: Firstly, the similarities in the AID at a wavelength of 800 nm for large angles when comparing FDTD and back side texture PM. Secondly, the influence on EQE *and* absorptance calculated from FDTD show little decrease in cell performance at long wavelengths for the polished sample, the latter completely ignoring electrical effects.

Additionally, we found out that the mechanical polishing performed to flatten the front side texture was not as perfect as hoped for due to previous experience [59], and introduced strong electrical defects at the front side of the cell, indicated by the loss in EQE surpassing the loss in absorptance found in FDTD simulations.

7

ABSORPTION AND QUANTUM EFFICIENCY

7.1 NON-CONFORMAL INTERFACES

After looking at different back side materials to model single junction devices and approximate the top cell of a tandem device, another important factor has to be taken into account: While simulations in the previous section (...) assumed the same texture at all interfaces, as is often done[60, 61, 62], silicon growth in our deposition systems does not perfectly reproduce the texture of the substrate. Depending on the material deposited and the layer thickness, the original texture can be unrecognisable after the deposition.[63] This strong difference in texture is investigated as to the influence of the non-conformal growth on the absorptance in a silicon layer. The goal is to ascertain if the effect of the texture difference on cell performance has to be taken into account in simulations or if the (common) assumption of identical textures at all interfaces is justified.

For this investigation, two materials have to be investigated very thoroughly: a-Si:H and μc-Si:H, since both are used either as single junction devices or, in combination, as tandem solar cell. The growth mechanism of these two materials is very different:

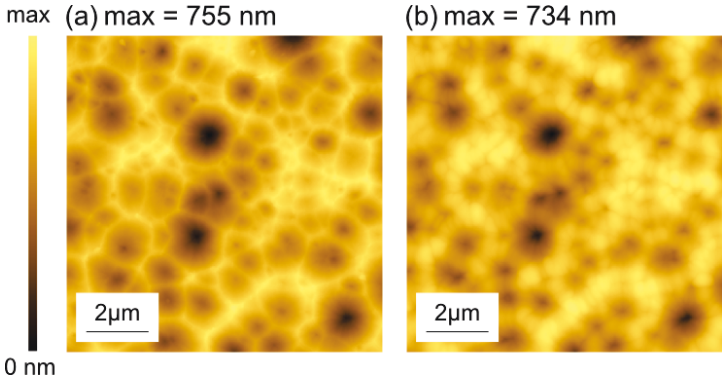

Figure 7.1.: Topography before (a) and after (b) deposition of a 500 nm thick a-Si:H layer. The a-Si:H-deposition rounds of the sharp crater rims.

For a-Si:H, as is shown in Fig. 7.1, the sharp features of the original texture are rounded off by the amorphous material. The research group of Knipp[57]

has developed a model to describe this behaviour very well. Therefore, while the a-Si:H systems presented in this section have been measured by AFM at the same position, it is generally also possible to calculate the texture after growth.

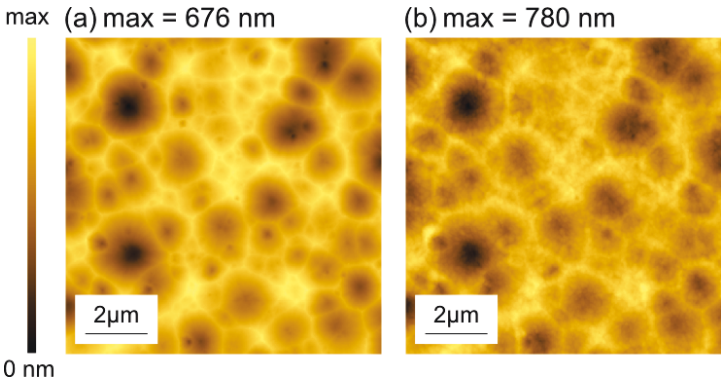

Figure 7.2.: Topography before (a) and after (b) deposition of a 1000 nm thick µc-Si:H layer. The µc-Si:H-deposition adds small protrusions to the whole surface due to the growth of Si crystallites.

µc-Si:H, on the other hand, modifies the texture in a very different, seemingly random way, as is shown in Fig. 7.2. The original features are superimposed by sharp smaller features, which represent the crystallites of the µc-Si:H. This growth behaviour has not yet been successfully described by a model, therefore obtaining the texture before and after growth by AFM is extremely important.

The surface textures shown in Fig. 7.1 and Fig. 7.2 were obtained using AFM before and after silicon deposition at the same spot.

The investigation will focus on two systems:

- A 500 nm a-Si:H cell on a wet-etched ZnO:Al substrate (Fig. 7.1)
- A 1000 nm µc-Si:H cell, also on wet-etched ZnO:Al (Fig. 7.2)

The simulations were performed using a spatial resolution of 20nm for a lateral size of 10 µm x 10 µm, with periodic boundary conditions in lateral direction and open boundaries, obtained by perfectly matched layers (PML), in propagation direction. At the interfaces between TCO and Si and between Si and the back contact, modelled using a PEC, different textures can be incorporated. With two different interfaces and two measured textures for each sample, there is a total of four possible configurations, as shown in Fig. 7.3. The permutations shown in that figure are as follows:

- Front TCO structure at both interfaces: This is the approach used in the previous sections and by many others, as mentioned earlier[50, 60, 61, 62]. This combination will be referred to as "conformal TCO device" (Fig. 7.3(a)).

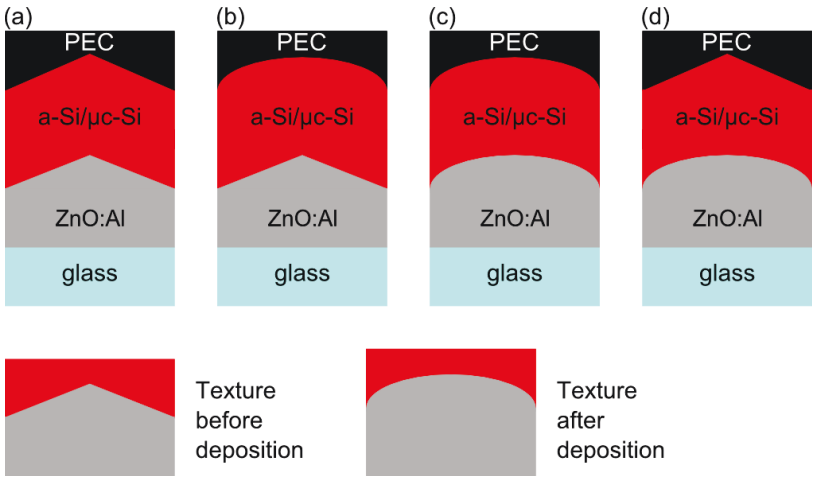

Figure 7.3.: All possible permutations for the measured textures before and after deposition: Reference structure with front TCO texture at both interfaces (a), the textures positioned as in the real-life device (b), the post-deposition texture at both interfaces (c) and the "inverse real-life structure" (d).

- Front TCO structure at the TCO/Si interface and Si structure at the Si/PEC interface: This represents the structure of the real device, and will therefore be referred to as "real-life device" (Fig. 7.3(b)).
- Si structure at both interfaces: The third possible combination, using the Si texture at all interfaces, referred to as "conformal Si" (Fig. 7.3(c)).
- Si structure at the TCO/Si interface and TCO structure at the Si/PEC interface: The real-life device upside-down, therefore referred to as "inverse real-life device", shown in Fig. 7.3(d).

While the first two combinations are sufficient to ascertain if the silicon growth has an impact on cell performance, the two remaining texture permutations are investigated for two reasons: First, the non-conformal samples (real-life device and inverse real-life device) introduce a thickness variation across the sample surface, changing light-guidance inside the sample. A change in this quantity can be assumed in wavelength regions where the non-conformality of the interfaces dominate the cell performance. Second, the influence of different light scattering properties of the different textures can be discerned in more detail when all permutations are taken into account. This is assumed to be the main impact on cell performance if the texture and its position in the cell are dominating absorption behaviour. These light scattering properties also depend on the position of the interface on the cell. At the front side, the light in-coupling is affected, leading to less reflexion losses, as well as possible scattering in transmission. At the back side, only light scattering in reflection takes place.

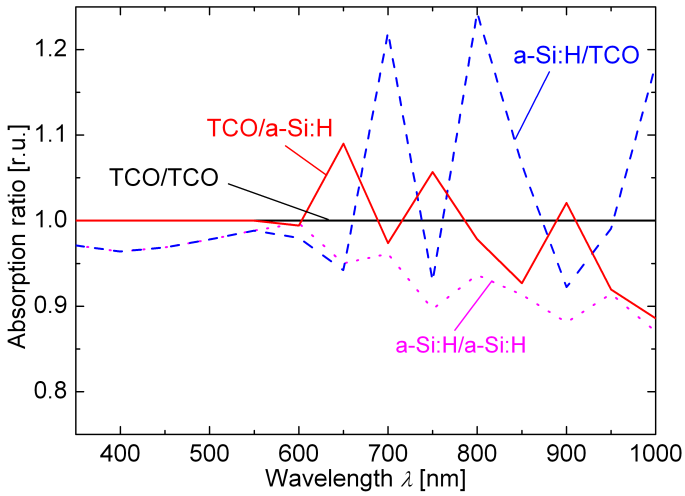

Figure 7.4.: Spectrally resolved increase/decrease in absorptance of a 500 nm a-Si:H cell for different interface texture combinations. The a-Si:H texture shows detrimental influence on light incoupling in the short wavelength region (a-Si:H/a-Si:H and a-Si:H/TCO), while the thickness variation introduced by silicon growth has a positive influence on absorptance in the long wavelength region (TCO/a-Si:H and a-Si:H/TCO).

Looking at the relative changes in absorptance of the a-Si:H cell in detail, as shown in Fig. 7.4, we can discern different influences; the short wavelength region between 400 nm and 600 nm is apparently dominated by the structure of the TCO/a-Si:H interface. No matter the texture at the a-Si:H/PEC interface, the absorptance does not change for a specific TCO/a-Si:H interface texture. This can be attributed to the light incoupling properties of the first interface. In the case of a-Si:H, the TCO texture shows a better light incoupling - when weighted with an AM1.5 spectrum, the a-Si:H texture at the front side leads to a decrease in absorption between 400 nm and 600 nm of 1.68% and 2.14% for an a-Si:H and TCO back side texture, respectively. This is in accordance with the fact that at a wavelength of 600nm, the light reaches the back contact and is also influenced by the back side texture. In the long wavelength region above 600 nm, the conformal a-Si:H device shows the worst performance, with a total loss of 5.48%. When taking into account the increase in performance of the real-life device in this wavelength region, as well as the (lower) increase in performance of the inverse real-life device, the effect of non-conformality shows a strong (positive) impact on cell performance as opposed to the position of the individual textures, when weighted with the solar spectrum.
The fringes in relative absorptance differences, especially visible for the real-life and inverse real-life devices, but most pronounced for the inverse real-life device, can be attributed to shifts in the Fabry-Perrot interferences in absolute absorptance. Note that relative absorptance changes at wavelengths

$\lambda > 750$nm have little impact on the overall performance due to the small absolute absorptance in this wavelength region.
This means that for the (thin) a-Si:H cell, light guidance effects seem to be dominating the performance in the long wavelength region, since the textures themselves and their position have little influence on absorption.

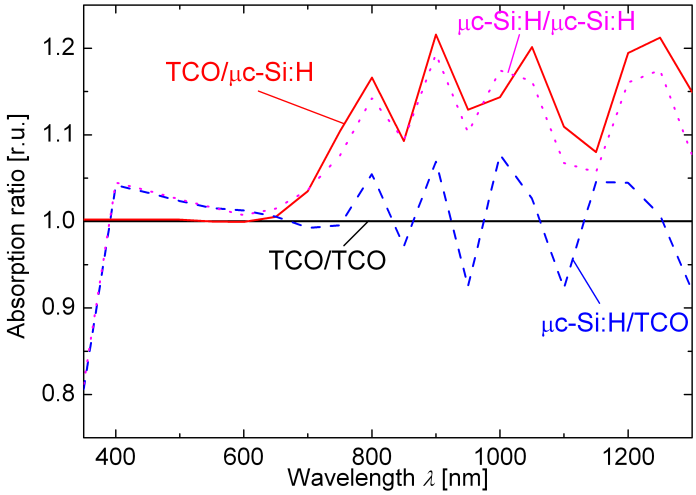

Figure 7.5.: Spectrally resolved increase/decrease in absorptance of a 1000 nm μc-Si:H cell for different interface texture combinations. The μc-Si:H texture shows better performance as both the front side texture in the short wavelength region (μc-Si:H/TCO and μc-Si:H/μc-Si:H) and as the back side texture in the long wavelength region (TCO/μc-Si:H and μc-Si:H/μc-Si:H).

The spectrally resolved differences in the absorptance of μc-Si:H show different behaviour, with the differences shown in Fig. 7.5. The performance in the short wavelength region between 400 nm and 600 nm is dominated by the TCO/μc-Si:H interface texture, the same as the a-Si:H cell. In this device, however, the texture after the deposition shows an increase in absorptance. This can be explained when looking at the topographies before and after deposition, as shown in Fig. 7.2. While the overall texture is still clearly visible, there are small additional features caused by the growth of crystallites in the μc-Si:H. These lead to a less pronounced refractive index gradient between the two adjacent materials, i.e. TCO and μc-Si:H. This again cause better light incoupling and therefore higher absorptance in the short wavelength region. In the long wavelength region, however, the behaviour of the μc-Si:H sample is quite different from that of the a-Si:H cell; the absorptance is clearly dominated by the back side texture, as both the real-life device and the conformal μc-Si:H sample show very similar absorption enhancements in the long wavelength region, totalling at an increase of 6.86% abd 6.74%, respectively. In contrast to this, the inverse real-life device shows the same fluctuations as observed for

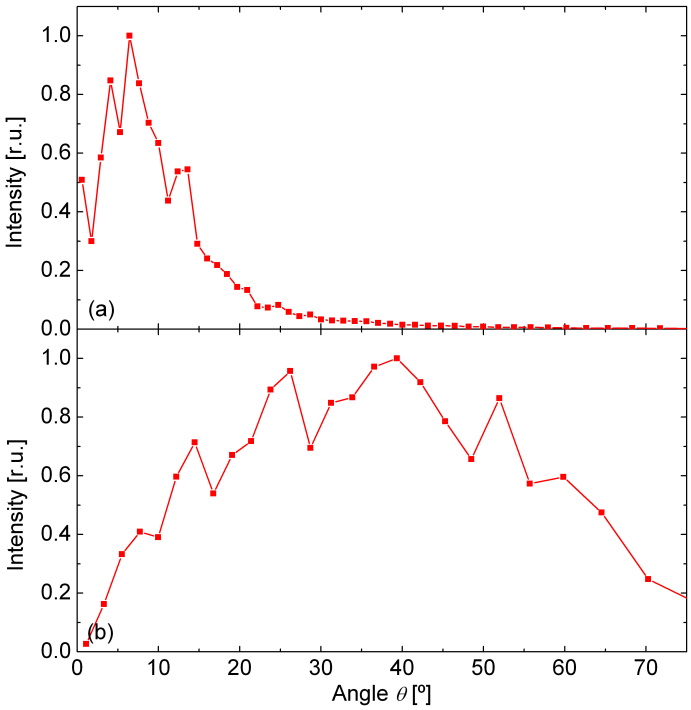

Figure 7.6.: AID of the µc-Si:H-texture in transmission (a) and reflection (b) at a wavelength of 700 nm at a TCO/µc-Si:H interface. Most of the light is scattered in angles smaller than 15° in transmission. In reflection, most of the light is scattered into large angles beyond the angle of total internal reflection.

the a-Si:H cell, with a total increase of only 0.67%, indicating that thickness inhomogeneities and the resulting influence on light guidance are negligible. With a total absorber thickness of 1 µm, this is a feasible result. The highest total increase in absorptance is observed for the conformal µc-Si:H cell, utilising both the good light incoupling *and* the good light scattering properties of the µc-Si:H texture.

Since for the µc-Si:H samples, the absorptance in the different wavelength regions is clearly dependant on the front and back side textures, it is also of interest to investigate the AID of the different textures in both transmission and reflection. This can help to explain the significantly better absorptance caused by the µc-Si:H texture. These AIDs, as calculated by PM, are shown in Fig. 7.6(a) and (b), respectively for a wavelength of 700 nm. These figures show the AID for the TCO (a) and µc-Si:H texture (b).

As can be seen, the µc-Si:H texture shows much better light scattering in transmission as well as reflection. Overall, the light is scattered into larger angles for the µc-Si:H texture. This explains the better absorptance when both interfaces are assumed to be as they are after the µc-Si:H deposition.

Overall, these investigations have shown that the non-conformal growth of layers has to be included in simulations to correctly describe a Si-based thin-film solar cell.

7.2 SIMPLE TEXTURE MODIFICATIONS

After looking at non-conformality of real-life devices and its influence on different solar cell structures, an additional field of interest in this work is the investigation of artificially generated structures, the results of which extend the work of Eockstuhl et al.[50]. Due to the good performance already obtained by using randomly textures TCOs obtained by wet-chemical etching, which is widely documented [31, 2], investigations of artificial structures are also based on these. In the first section investigating these structures, very simple modifications by stretching or compressing a TCO texture in both lateral and height direction are considered. The original texture used for these modifications is shown in Fig. 7.7.

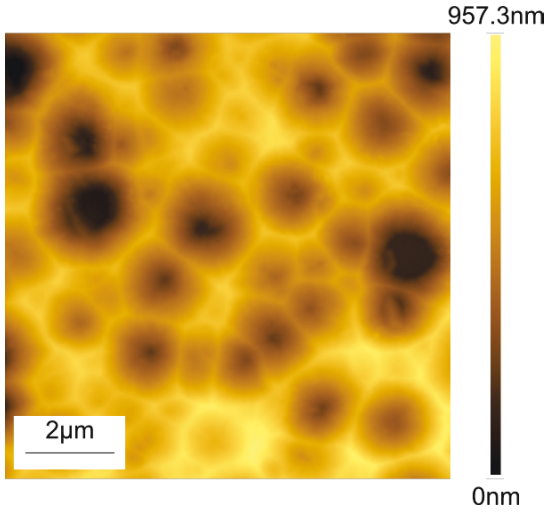

Figure 7.7.: 10µm × 10µm AFM scan of original texture; a standard wet-etched ZnO:Al layer was used as basis for all texture modifications investigated here. The typical, random crater-like structures of various sizes are clearly visible

This texture was stretched in lateral direction by factors between $f_{lat} = 0.5$ and $f_{lat} = 2.0$, with higher resolution between $f_{lat} = 0.5$ and $f_{lat} = 1.0$ due to preliminary results showing good performance increase in this area. The stretching in growth-direction was performed with factors between $f_h = 0.5$ and $f_h = 3.0$, with more investigations between $f_h = 1.0$ and $f_h = 1.5$ due to a high difference between the results for $f_h = 1.0$ and $f_h = 1.5$.

The system to which the texture modifications were applied is shown in Fig. 7.8: A glass half-space was assumed as substrate, covered by a TCO

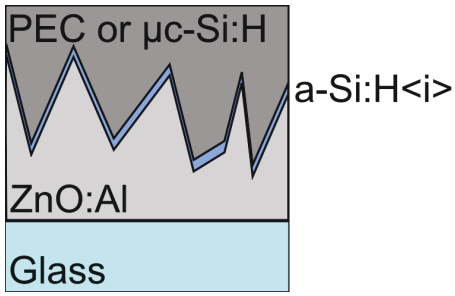

Figure 7.8.: Model of the simulated system: The light enters the system through a glass half space. This "substrate" is covered with a rough ZnO:Al layer, the interface roughness obtained from the AFM scan (Fig. 7.7). On top of this TCO, a 300 nm thin a-Si:H layer is assumed with a conformal texture at the back side. The back contact consists of either a PEC (for the single junction model) or µc-Si:H to model the top cell in a tandem device.

(ZnO:Al) with the respective texture. The layer for which the absorptance is calculated is a 300 nm thin a-Si:H layer on top of this TCO. The back side of the model consisted of either a PEC or a µc-Si:H half-space. The former shows the influence of the texture on a single junction device, while the latter allows for an investigation of the second interface (a-Si:H/µc-Si:H) in a tandem device; this is an important aspect in respect to current matching between top and bottom cell.

The total absorptance in the a-Si:H layer was compared to an equivalent system using the original texture. In all cases, the absorptance was corrected according to the total absorbing volume of the a-Si:H layer. For the lateral

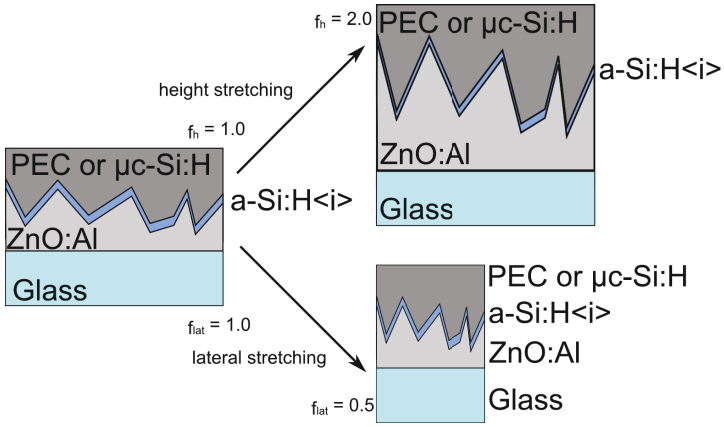

Figure 7.9.: Sketch of the modifications performed on the original texture (Fig. 7.7). Depending on the type of stretching (lateral: bottom, height: top), either the AFM scan was laterally modified to obtain the same resolution (f_{lat}) or the height was multiplied with a given factor (f_h).

Table 7.1.: Overall change in absorptance between 350 nm and 800 nm of the a-Si:H single-junction device for different scaling factor f_{lat} and f_h. These overall changes are absorptance changes weighted with an AM1.5 spectrum. For lateral stretching, a value of $f_{lat} = 0.6$ is optimal, while for height stretching, $f_h = 2.0$ shows the best overall improvement. Both changes lead to very similar steepness of crater flanks, indicating these as dominating the absorptance. However, height stretching is less effective due to larger effective thickness of the front TCO and resulting higher parasitic absorption.

(a)

f_{lat}	Δ_{Abs}
0.5	13.7%
0.6	**15.4%**
0.7	11.5%
0.8	7.2%
0.9	3.3%
1.0	0.0%
1.5	-12.5%
2.0	-13.9%

(b)

f_h	Δ_{Abs}
0.5	-10.2%
1.0	0.0%
1.1	1.6%
1.2	3.5%
1.3	4.9%
1.4	6.4%
1.5	5.2%
2.0	**6.5%**
2.5	6.3%
3.0	5.2%

modifications, the lateral resolution of the original measurement was modified to compensate the smaller area, according to f_{lat}, if $f_{lat} < 1$. In the case of $f_{lat} > 1$, a part of the topography was stretched to a size of $10\mu m \times 10\mu m$ with a resolution of 20 nm. For the height stretching, the measured height at each point was simply multiplied with f_h. A sketch of this is shown in Fig. 7.9. As for most simulations, periodic boundary conditions and a resolution of 20 nm were used due to calculation time limitations.

7.2.1 *a-Si:H cell with PEC back contact*

Firstly, the thin a-Si:H single junction device is described, a sketch of the model being shown in Fig. 7.8.

Looking at the absorption enhancements relative to the of the a-Si:H single junction cell with lateral stretching in detail, shown in Fig. 7.10, an actual compression ($f_{lat} < 1$) shows an increase over the whole spectral range, while larger values ($f_{lat} = 1.5$ and $f_{lat} = 2.0$) lead to a decrease in absorptance compared to the original texture ($f_{lat} = 1.0$) of up more than 13%. In the short wavelength region, this is attributed to a better light incoupling due to the steeper crater flanks and smaller feature sizes; while for the original texture, some features can be assumed to be an effective medium[64] with a refractive index gradient*, many of the larger features cannot be described in such a way. When laterally compressing the textures, more of the features exhibit

* leading to less reflection losses

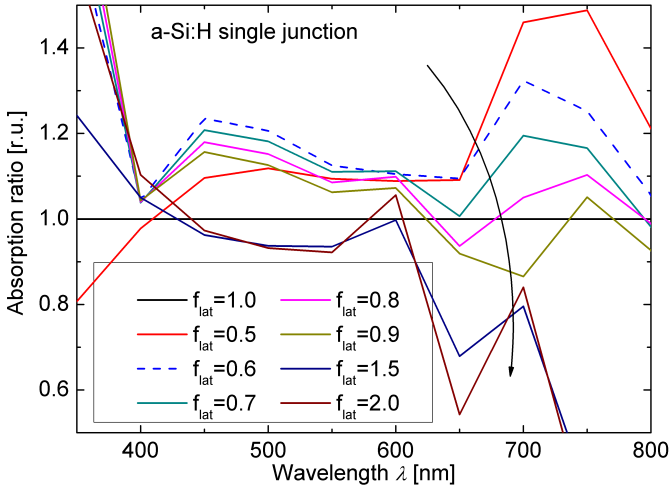

Figure 7.10.: Spectrally resolved relative absorptance difference for lateral stretching for multiple values of f_{lat}. The best enhancement in this case is shown as dashed line, which can be observed for $f_{lat} = 0.6$.

sizes which make an effective medium approach valid, suggesting better light incoupling. In the long wavelength region, the same steeper crater flanks lead to better light scattering, as shown in the AID of a texture with steep and shallow flanks in Fig. 7.11 (a) and (b), respectively.

When looking at the lateral modification with the strongest decrease in absorptance ($f_{lat} = 2.0$), we see the opposite effect in the long wavelength region, which again can be explained using the AID, shown in Fig. 7.11. The specular peak of the AID is much higher, meaning worse light scattering and trapping in the device.

Additionally, the absorption planes, as described in Sec. 4.4, were calculated for all modifications and wavelengths. Figure 7.12 shows these planes for wavelengths of 450 nm (Fig. 7.12(a)), 550 nm (Fig. 7.12(b)) and 650 nm (Fig. 7.12(c)) for the lateral stretching with the best results ($f_{lat} = 0.6$). The first plane representing a spectral area where light-trapping has negligible influence, the second showing the shortest wavelength at which a measurable portion of the light reaches the back contact and therefore light-trapping starts to influence performance of the device. The longest wavelength represents the spectral area where light-trapping is dominating absorptance and therefore cell performance. For the two shorter wavelengths, the original texture (Fig. 7.7) can still be identified, and the highest absorptance is observed in the centre of craters with radii of about 500 nm. This has also been observed in previous works in both experiment and simulation [49] and is called "microlensing". It is also clearly visible that above the sharp crater rims, absorptance is minimal. For the longest wavelength of 650 nm, the original texture is not as clearly visible any more, but the local absorptance appears to be more random. However,

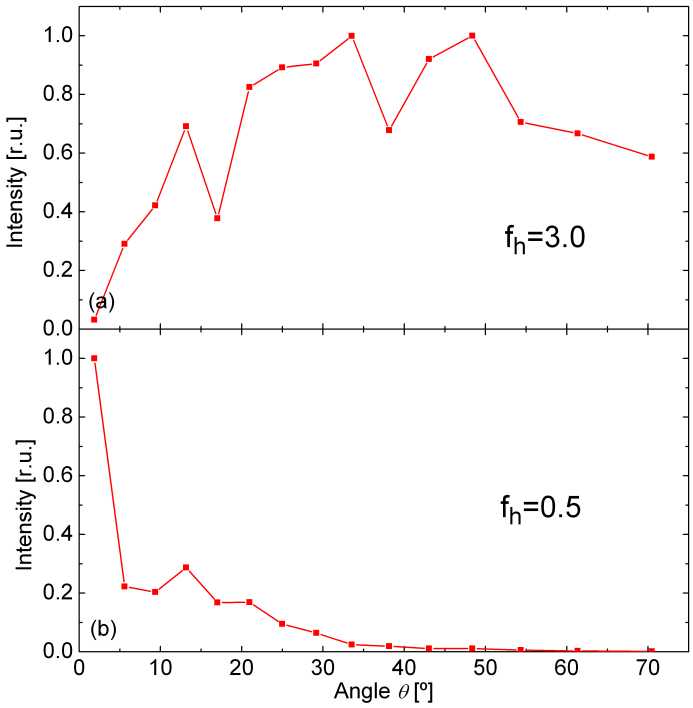

Figure 7.11.: AID of a texture with steep flanks ($f_h = 3.0$) (a) and shallow flanks ($f_h = 0.5$) (b). As can be seen, much of the light is scattered into large angles for a texture with steep flanks, with a maxima at about 35° and 48°. For shallow flanks, most of the light is not scattered at all, with the rest scattered only into small angles.

the areas with absorptance "hotspots" can still be identified above some of the crater centres.

When looking at this absorptance over the whole spectral range, weighted with an AM1.5g spectrum and shown in Fig. 7.12(d), the shape of the original texture (Fig. 7.7) is again clearly visible, hinting at a stronger influence of the short wavelengths. Additionally, the microlensing effect can be seen for all craters with a radius above 200 nm which leads to a strong increase in light intensity above certain craters. This also supports the often observed, very strong positive influence of randomly textured ZnO:Al on cell performance observed in other works[2, 3].

The white squares visible in all graphs in Fig. 7.12 mark the areas of highest total absorption of all areas of that size for squares between 500nm × 500nm and 2µm × 2µm. The position of these areas can shift slightly depending on square size and wavelength, but mostly appear in areas including craters with a radius of about 500 nm. When looking at the total absorption plane (Fig. 7.12(d)), the area of highest absorptance is approximately the same for all area sizes and again includes craters with a radius of about 500 nm.

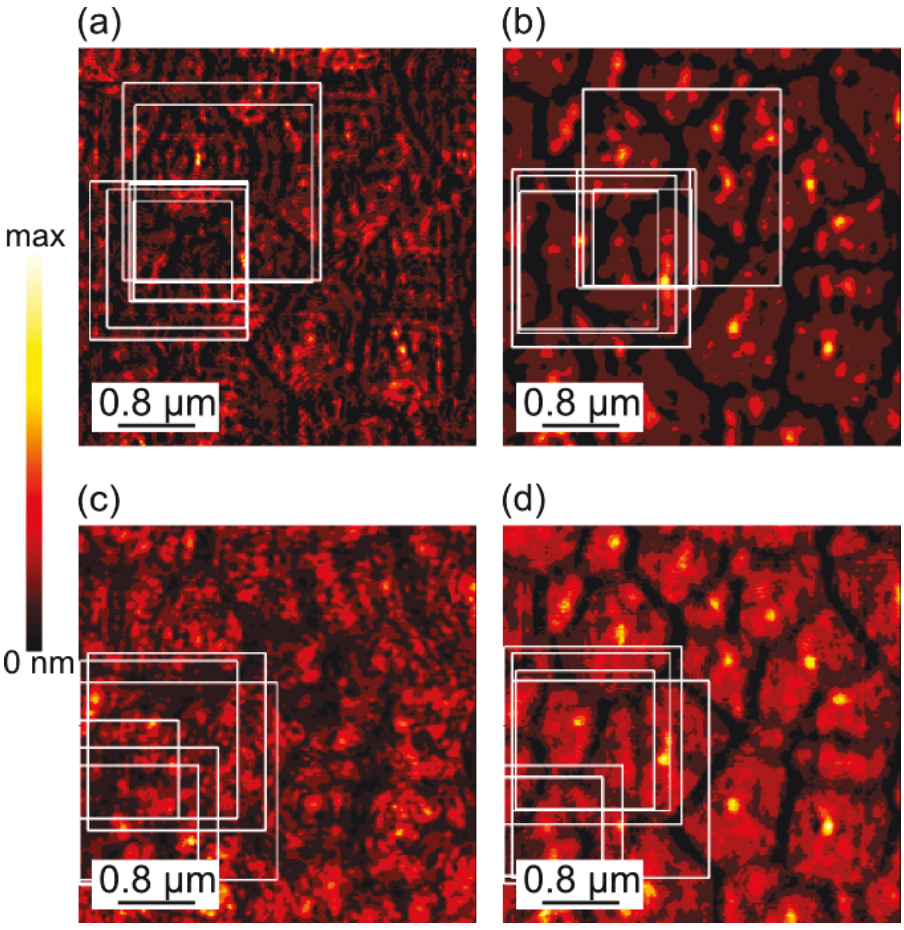

Figure 7.12.: Absorption planes (as described in Sec. 4.4) of the best lateral stretching ($f_{lat} = 0.6$) for wavelengths of 450 nm (a), 550 nm (b) and 650 nm (c). An integrated absorption plane over all wavelengths weighted with an AM1.5g spectrum is shown in (d). The white squares indicate areas with the highest integrated absorptance of all areas of that size.

Looking at the same quantities for the height stretching, very similar conclusions can be drawn; as shown in Fig. 7.13, the absorptance enhancement in the long wavelength region is very similar to that obtained by lateral compression. For the best modification ($f_h = 2.0$), the absorption enhancement shows a nearly identical behaviour to that obtained for the best lateral stretching ($f_{lat} = 0.6$). Considering that the modification of the texture obtained by those two modifications leads to the same surface angles, this indicates the importance of this ratio. The total absorption enhancement of the height stretched sample, however, is smaller than that obtained by lateral compression. This can be explained when looking at the absorption difference in the short wavelength region. In this area, the absorption, especially below 450 nm, is strongly

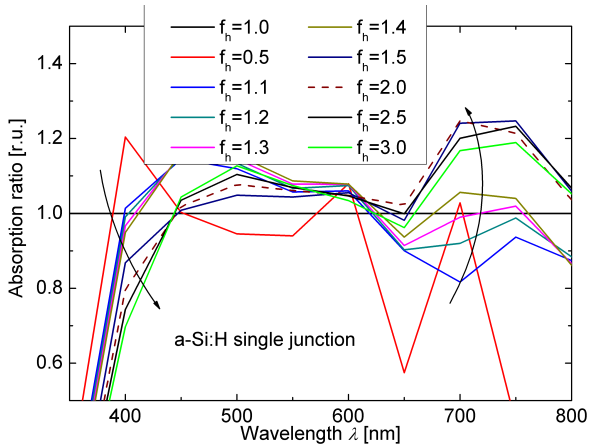

Figure 7.13.: Spectrally resolved absorptance enhancement for height stretching for multiple values of f_h. The best enhancement is shown as dashed line, with a factor of $f_h = 2.0$.

reduced, where for lateral compression ($f_{lat} = 0.6$) absorptance is increased. This can be explained by the larger effective layer thickness of the front TCO obtained when height-stretching the sample. Since in this wavelength region, the TCO is strongly absorbing, less light even reaches the scattering interface, therefore decreasing overall intensity and absorptance in the a-Si:H layer.

The absorption planes, as shown in Fig. 7.14, show similar results as the lateral stretching, further supporting the theory that the ratio between lateral dimension and height of a crater is most important. Again, for short wavelengths (Fig. 7.14(a)), the texture is easily identified while interference effects can be seen inside the craters. for an intermediate wavelength of 550 nm (Fig. 7.14(b)), the topography is also recognisable, with microlensing effects above the crater centres, while for long wavelengths (650 nm, Fig. 7.14(c)), only the crater rims are visible in the integrated absorption. When weighted with an AM1.5g spectrum (Fig. 7.14(d)), the texture is again clearly visible with a microlensing effect above many craters, with the areas of highest absorption above craters with a radius of about 500 nm.

7.2.2 *a-Si:H cell with a μc-Si:H back side*

Additionally, as a preparation for investigations of a-Si:H/μc-Si:H tandem devices, these texture modifications were applied to an a-Si:H cell identical to the one investigated in the previous section, but adjacent to a μc-Si:H half space instead of a PEC. This is used as an approximation for the top cell of a tandem device, since the thickness of the μc-Si:H bottom cell is significantly larger than the top cell. Of special interest in this model is the wavelength region between 500 nm and 850 nm, since here, both top *and* bottom cell contribute to cell performance and the transmission into the bottom cell can be investigated.

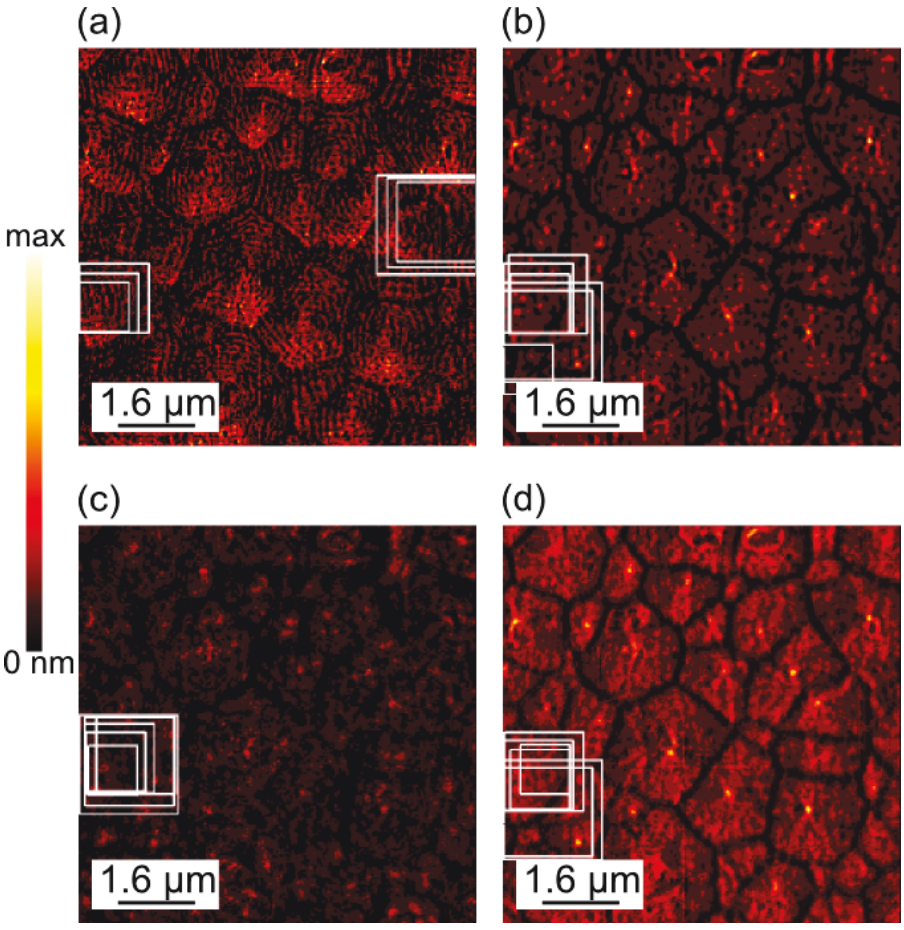

Figure 7.14.: Absorption planes (as described in Sec. 4.4) of the best height stretching ($f_h = 2.0$) for wavelengths of 450 nm (a), 550 nm (b) and 650 nm (c). An integrated absorption plane over all wavelengths weighted with an AM1.5g spectrum is shown in (d). The white squares indicate areas with the highest integrated absorptance of all areas of that size.

The relative absorptance enhancements are shown in Tab. 7.2. While the best absorptance enhancement for lateral stretching is observed for a value of $f_{lat} = 0.5$, this value is not taken into account due to strong edge effects. While there are enhancements visible, the effect is far less pronounced than for the PEC back side. The reason for this is the transmission into the µc-Si:H back side, where for the PEC back side, perfect reflection occurred. While another explanation could be different light propagation and more parasitic absorption in the TCO, this was checked by looking at the absolute absorptance values inside the TCO integrated over the whole layer. The results were identical for both the PEC and the µc-Si:H back side.

Table 7.2.: Total absorptance enhancement for lateral (a) and height (b) stretching in the a-Si:H top cell of a simplified tandem device. Best results are shown in **bold**, while worst results are *italic*. These values result from absorptance calculations, weighted with an AM1.5g spectrum. The value $f_{lat} = 0.5$ is not taken into account due to strong edge effects.

(a)

f_{lat}	Δ_{Abs}
0.5	11.2%
0.6	**6.4%**
0.7	5.1%
0.8	3.4%
0.9	1.8%
1.0	0.0%
1.5	*- 4.0%*
2.0	- 3.8%

(b)

f_h	Δ_{Abs}
0.5	1.7%
1.0	0.0%
1.1	0.9%
1.2	1.5%
1.3	1.9%
1.4	**2.2%**
1.5	1.3%
2.0	0.8%
2.5	0.0%
3.0	*-1.1%*

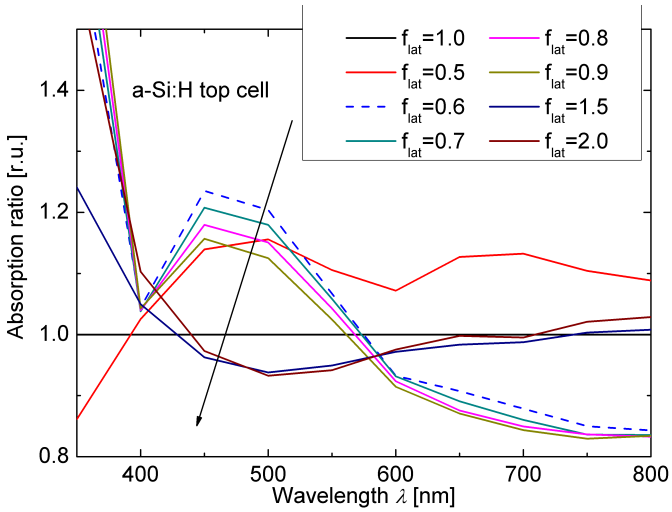

Figure 7.15.: Spectrally resolved absorptance increase/decrease for the simplified tandem device for multiple values of f_{lat}. While in the short wavelength region is similar to that obtained with a PEC back side (Fig. 7.10), those modifications showing the highest increase in the short wavelength region (and overall) show a strong decline in absorptance in the long wavelength region. Due to the identical parasitic absorptance in the front TCO layer, this must be transmitted into the μc-Si:H back side.

Looking at the absorption increase/decrease as a function of the wavelength for lateral stretching, as shown in Fig. 7.15, there are two distinct regions:

- The short wavelength region up to 550 nm, where the increase in absorptance for the best modifications is very similar to that of the single junction simulations, and
- The long wavelength region from 600 nm upwards, where the absorptance in the a-Si:H layer is actually reduced. However, this "lost" light must be transmitted into the μc-Si:H half space.

When taking both into account, the short wavelength region is clearly dominant for cell performance. Since the μc-Si:H half space is an approximation of the bottom cell of a tandem device, the higher transmission into the μc-Si:H at wavelengths above 550 nm would benefit the bottom cell in a tandem device, while the better absorptance in the short wavelength region still increases overall performance of the top cell (s. Tab. 7.2.

The absorption planes for the lateral stretching of the simplified tandem device, shown in Fig. 7.16, are slightly different from that of the single junction device (Fig. 7.12); in this case, the original texture (Fig. 7.7) is even clearly visible for the wavelength of 650 nm, as shown in Fig. 7.16(c), due to the fact that there is much less reflection at the a-Si:H/μc-Si:H interface and therefore less scattering which would blur the features. Additionally, the area of highest absorptance, marked in Fig. 7.16 as white squares, shifts around much more with size than for the single junction device (Fig. 7.12), which is also attributed to the higher transmission.

Looking at the height stretching (Fig. 7.17), the results are very similar, with the same limitations as the single junction device: In the short wavelength region below 450 nm, the larger effective TCO layer thickness leads to higher parasitic absorptance and reduced performance of the device. Above 600 nm, less light is absorbed in the a-Si:H layer and more transmitted into the μc-Si:H half space. However, the strong increase in the intermediate wavelength region leads to a small increase in total performance. The best increase is obtained for $f_h = 1.4$, as shown in Tab. 7.2.

The absorption planes for the best height stretching ($f_h = 1.4$), displayed in Fig. 7.18, are slightly different from those obtained for lateral stretching ($f_{lat} = 0.6$); while for the longest wavelength (650 nm), the original texture (Fig. 7.7) is as clearly visible as for the lateral stretching (Fig. 7.16), the areas of highest absorptance are much less size dependant, especially when looking at the overall absorption plane, as shown in Fig. 7.18(d).

7.3 TEXTURES OPTIMISED FOR LIGHT SCATTERING

During this thesis, the results from the simple texture modifications and the application of the phase model, another approach to optimise the surface texture of a TCO was investigated, in close cooperation with Dr. K. Bittkau.[65] Due to the fact that the AID is calculated from PM via FFT, it is also possible to

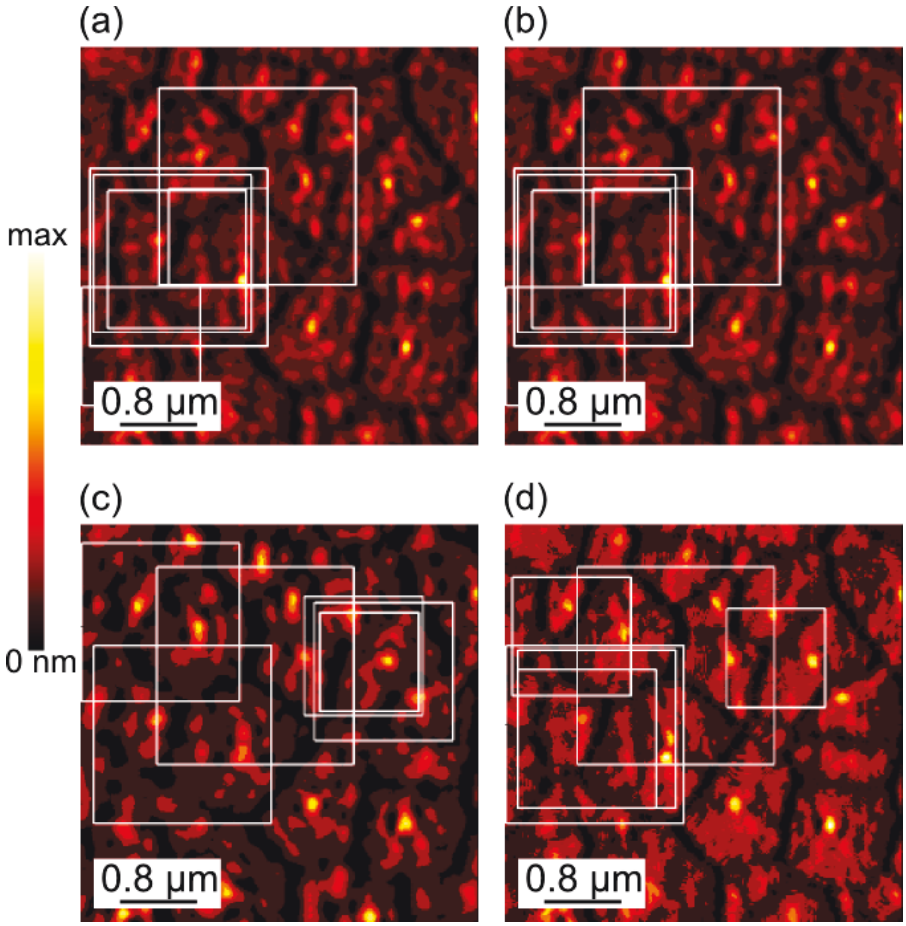

Figure 7.16.: Absorption planes (s. Sec. 4.4) of the best ($f_{lat} = 0.6$) lateral stretching for 450 nm (a), 550 nm (b) and 650 nm (c). Weighted with an AM1.5g spectrum, the results are displayed in (d). Unlike the PEC-covered a-Si:H layer, areas of highest absorptance are much more size-dependant, especially for the overall absorptance (d). This is caused by the low reflection at the a-Si:H/µc-Si:H interface.

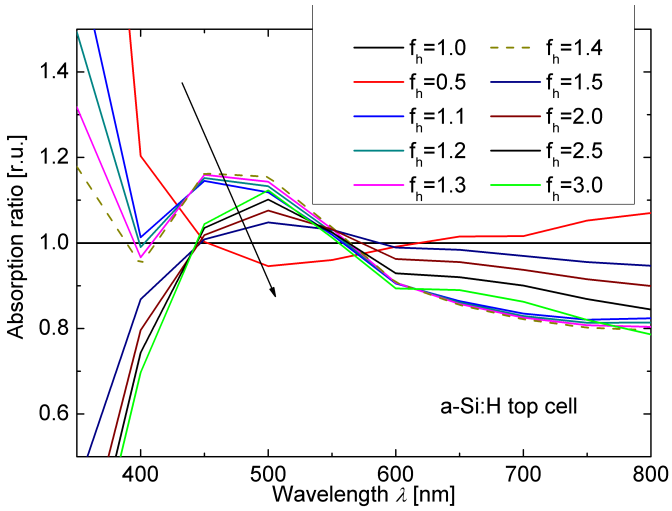

Figure 7.17.: Spectrally resolved absorptance increase/decrease for the simplified tandem device for multiple values of f_h. While in the short wavelength region is similar to that obtained with a PEC back side (Fig. 7.14), those modifications showing the highest increase in the short wavelength region (and overall) show a strong decline in absorptance in the long wavelength region. Due to the identical parasitic absorptance in the front TCO layer, this must be transmitted into the µc-Si:H back side. Again, when compared to the lateral stretching (Fig. 7.15), there is a decline in absorptance in the very short wavelength region due to higher effective thickness of the TCO layer and therefore more parasitic absorptance.

reconstruct a texture from a given phase shift image. By applying a Gaussian filter with a given width (σ) to the FFT, the scattering into small angles can be suppressed. Applying an inverse FFT (iFFT) to this modified Fourier image, the phase shift at each point can be calculated. This process of FFT, Gaussian filter and iFFT acts as a high pass filter for the AID. In a final step, the formula of the phase model (Eq. (3.11)) is inverted to regain a topography, modulo the period of 2π. By choosing the phase in each point in a way that the difference to the neighbouring points is minimised, this periodicity can be included. This results in a new topography, which exhibits the light scattering properties as tailored by the high-pass while still showing a strong resemblance to the original texture. This procedure is displayed in Fig. 7.19.

This optimisation can be performed for any given texture in two different ways: Either the light scattering in transmission is taken for the optimisation or that in reflection. However, both kinds of modification have an impact on light scattering in transmission *as well as* reflection. The optimised texture is, as expected, very similar to the original texture, with a few important differences, which are the following for a crater-like structure:

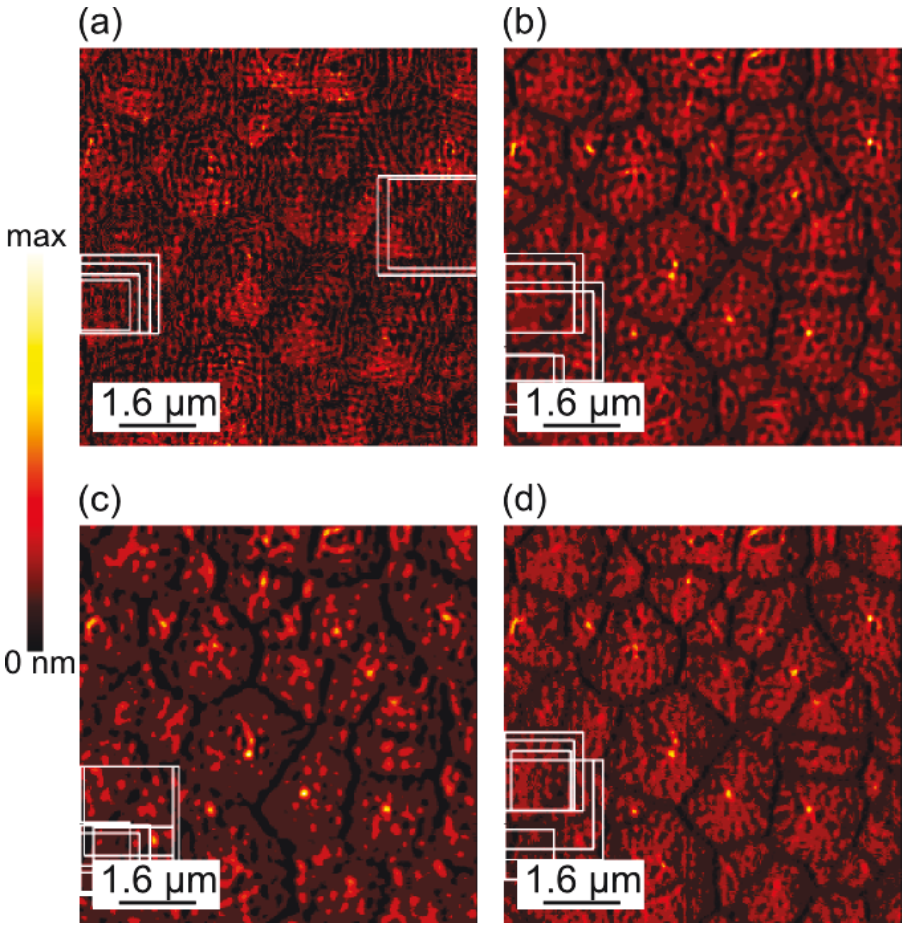

Figure 7.18.: Absorption planes (s. Sec. 4.4) of the best ($f_h = 1.4$) lateral stretching for 450 nm (a), 550 nm (b) and 650 nm (c). Weighted with an AM1.5g spectrum, the results are displayed in (d). In this case, areas of highest absorptance are very similar to that of the single junction device (Fig. 7.14).

- The crater flanks are deeper due to higher crater rims, leading to slightly steeper flanks at the inner boundary of the crater. The positive effect of steeper crater flanks on absorptance in a cell has been shown previously, in Sec. 7.2, as have been the effects of deeper craters.
- Small, sharp features are visible inside the craters. These are present in the original topography as well, but much less pronounced and hardly visible. These features might also be artefacts of the original AFM measurement, but - at least in theory - have a non-negligible influence on light scattering.
- For strong modifications of the AID, FFT artifacts become visible due to the periodicity of the FFT, which is not present in the sample.

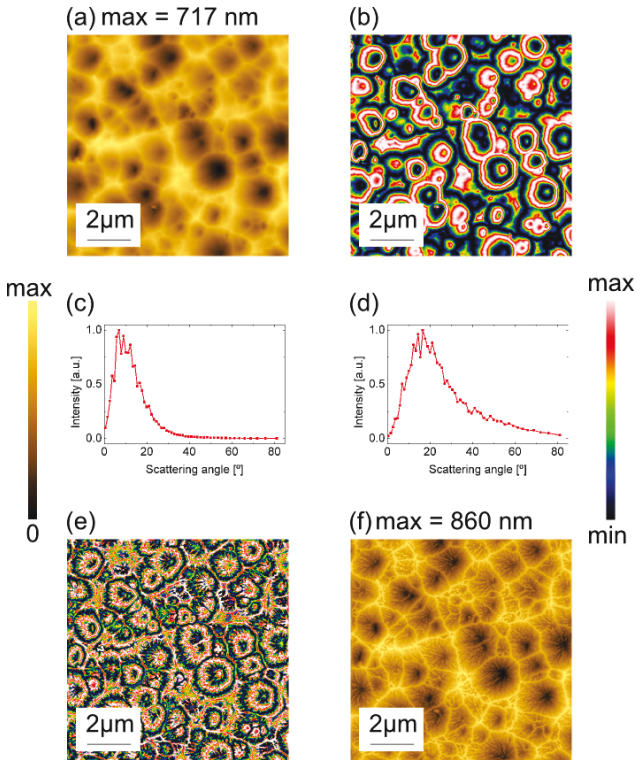

Figure 7.19.: Sketch of the topography optimisation by using FFT and PM. (a): The original texture that should be optimised. (b): The real part of the phase as obtained by PM. (c): The resulting FFT and AID. (d): FFT and AID after applying the high-pass filter. (e): The real part of the phase image obtained by iFFT. (f) The final result: An optimised texture calculated from the phase image. The structure is still very similar to the original texture, with smaller additional features inside the craters and the craters generally deeper and steeper. The additional features are rooted in small features which are small but present in the original texture. Also, some FFT artefacts can be seen, but these are not strongly pronounced.

With the aforementioned two possibilities of optimisation in mind, two textures were optimised: A typical ZnO:Al surface texture and a different texture obtained by wet-etching ZnO:Al which usually results in worse cells[31], referred to as "standard TCO" and "non-optimal TCO". The non-optimised textures are shown in Fig. 7.20. To quantify the effect of the modifications, two methods were combined: For one, the modified textures were used in FDTD simulation as both front and back texture and the EQE of a 1 µm thick µc-Si:H cell was calculated. The other approach was to calculate the amount of light scattered into angles larger than the angle of total internal reflection at the µc-Si:H/ZnO:Al interface, as obtained by PM.

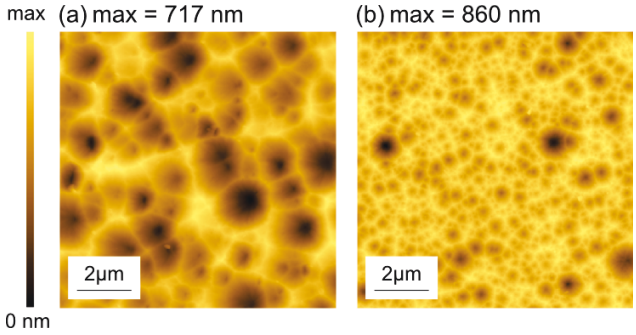

Figure 7.20.: Original textures used in the optimisation. Two etched ZnO:Al surfaces of type 2 (a) and type 3 (b) as described in [31].

Figure 7.21 shows the original and optimised textures for different cut-off angles of the Gaussian filter optimised for transmission (a) and reflection (b). The trend seen in the first example is also visible here: The optimised texture is still very similar to the original texture, with the craters being showing slightly higher rims and a few additional features in the crater centres.

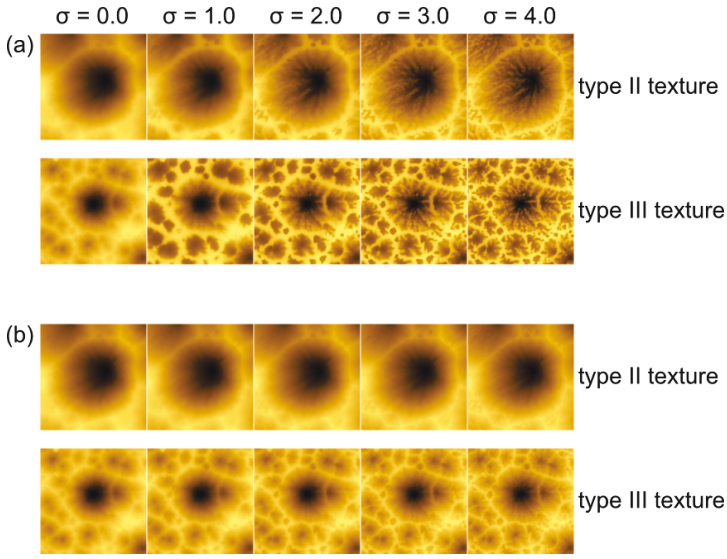

Figure 7.21.: Textures optimised for different limits of the high-pass filter. (a) shows the textures optimised for light scattering in transmission, (b) the ones optimised in reflection. The trends of the differences to the original texture are the same as seen for the example in Fig. 7.19. It is noteworthy that the optimisation in reflection leads to a smaller difference through the optimisation, mainly due to the fact that the original texture is already an excellent scatterer in reflection.

7.3.1 *PM results*

Firstly, the results of the simple PM calculations will be discussed. In this section, the focus lies on the amount scattered into angles larger than the angle of total internal reflection at a wavelength of 700 nm. The results are shown in Fig. 7.22 for both the standard TCO (a) and the non-optimal TCO (b). For the standard TCO, the tuning of the scattering in reflection shows only a slight increase in the scattering in reflection, since the original texture already provides a high scattering efficiency into large angles. However, the light scattering in transmission is hardly affected at all by these modifications. When optimising the scattering in transmission, the portion of light scattered into angles larger than the angle of total internal reflection is strongly improved, while the scattering in reflection shows little change and is nearly as good as the texture optimised for this scattering in reflection. This indicates that for this type of structure, the optimisation of light scattering in transmission is more effective.

Looking at the non-optimal TCO, which usually leads significantly worse cell performance (Fig. 7.22(b)), the results are very similar; tuning the reflection properties of the texture leads to an increase in the portion of light scattered beyond the angle of total internal reflection which is stronger than for the standard TCO. Also, the improvement in light scattering in transmission is more pronounced than for the standard TCO. Tuning the transmission shows an even stronger improvement than for the standard TCO in both transmission and reflection scattering. For weaker high passes, the improvement of the transmission scattering leads to an even better scattering in reflection than for the same optimisation in reflection. However, this scattering in reflection is reduced again for larger angles of the high-pass filter. These results nicely show that the influence of both types of scattering is of similar importance.

7.3.2 *FDTD results*

To decide, for which structures a whole spectrum should be simulated using FDTD simulations, the absorption enhancement in a 1 µm thick µc-Si:H layer covered by a PEC was considered at the wavelength used for the optimisation (700 nm). The modification showing the highest enhancement at that wavelength was then used for simulating a whole spectrum. The results of this first investigation for a wavelength of 700 nm is shown in Fig. 7.23 for the non-optimised TCO and the graphs also compare results from PM and FDTD simulations. As this graph shows, the strongest enhancement in absorption is observed for the tuned transmission with a width of the high-pass filter of $\sigma = 2.5$.

For the standard TCO, the optimum is assumed to be the strongest optimisation ($\sigma = 3.5$) in transmission, since the loss in reflection scattering is *much* smaller than the gain in transmission scattering.

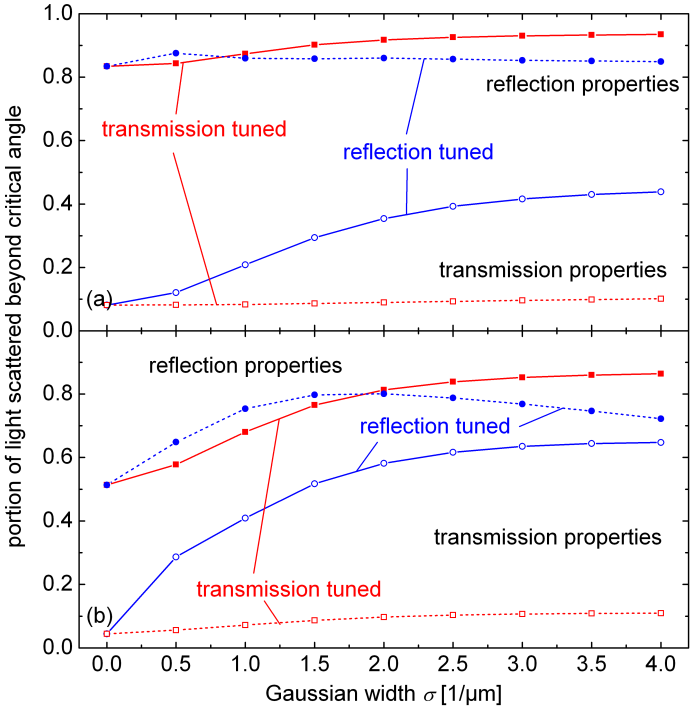

Figure 7.22.: Portion of light scattered into angles larger than the angle of total internal reflection at a TCO/µc-Si:H (T) or µc-Si:H/TCO (R) interface as a function of the width of the high-pass filter for the type 2 (a, 800_40s) and type 3 (b, ipv_100-119_45s) textures. The tuning of light scattering in reflection only leads to a slight improvement of light scattering in reflection and to even less increase in transmission for both textures. Tuning the transmission, however, has a serious impact on the performance in transmission while also slightly improving light scattering in reflection. This effect is more pronounced for the originally worse type 3 texture.

When looking at the EQE and absorption enhancement for these structures, shown in Fig. 7.24 (a) and (b), respectively, one can see the strong influence on optical cell performance of the optimisation. Most surprising is the fact that the originally worse non-optimal TCO shows a higher EQE when optimised than the standard TCO. This is even more pronounced when looking at the relative absorption enhancements.

7.3.3 *Conclusion*

Looking at the combination of PM and FDTD results, we have shown that a simple mathematical modification of existing textures by Fourier analysis show a strong improvement in optical performance. Combining both calculation methods, the EQE at the optimisation wavelength of 700 nm can be

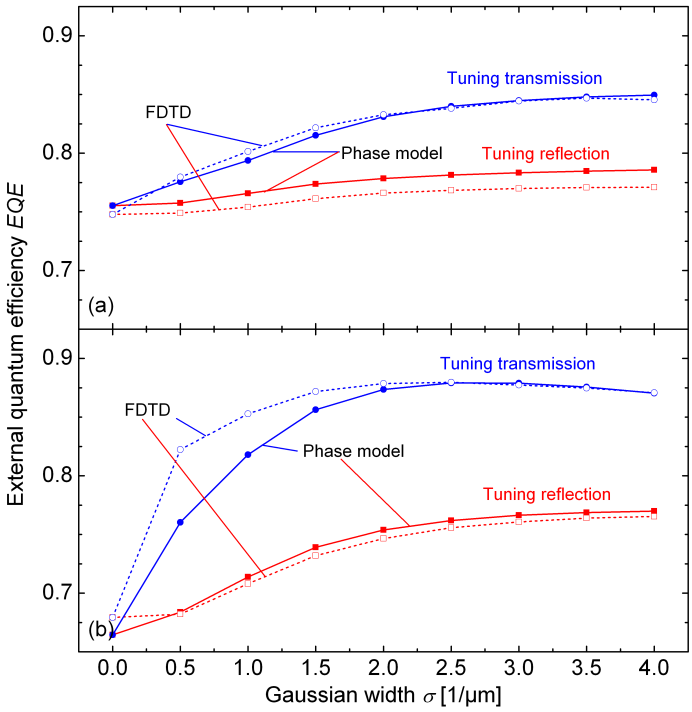

Figure 7.23.: Improvement in EQE as obtained by FDTD (dashed) and an empirical formula using PM results (solid) for the type 2 (a, 800_40s) and type 3 (b, ipv_100-119_45s) textures at a wavelength of 700 nm. The combination of light scattering in transmission and reflection allow for a good prediction of the FDTD results, with deviations originating from the thin layer thickness of the absorber layer and the multiples reflections at both interfaces of the absorber layer.

approximated by a linear correlation. The resulting parameters can then be used to calculate the EQE at all wavelengths.

However, this formula is purely empirical and is only tested for a 1 µm thick µc-Si:H cell on the modified textures. Additional influences of substrate structure, film thickness and absorption coefficient of the absorber layer have to be investigated further.

7.4 A COMPLETE TANDEM SOLAR CELL

In this final section about absorption in solar cells, a complete a-Si:H/µc-Si:H tandem solar cell is simulated and compared to experimental results. This comparison is used to investigate limitations of the simulations and the influence of the approximations made, such as the glass half space and the PEC back contact. Additionally, there are always uncertainties about the exact opti-

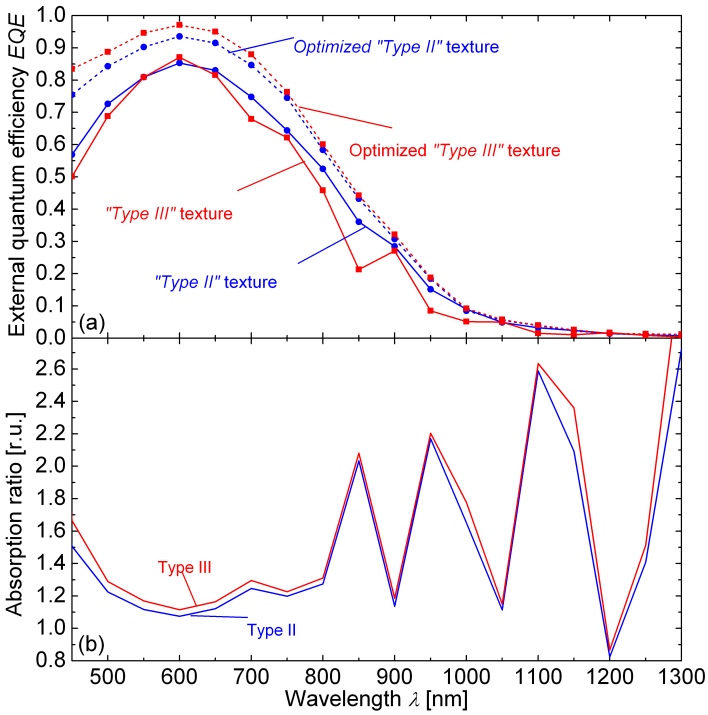

Figure 7.24.: EQE before (solid) and after (dashed) optimisation for both textures as obtained by FDTD (a) and relative enhancement (b) for both type 2 (blue) and type 3 (red) textures. The relative enhancement is very similar for both structures, since the optimisation was performed identically for both. And in both cases, the improvement, especially in the long wavelength region, is significant.

cal data of the materials and the layer thicknesses. The systems simulated and measured are shown in Fig. 7.25(a) and (b), respectively.

In addition to the structure of the layer stack, it is important to mention that these simulations were performed with a resolution of 10nm, since absolute values are investigated, for which the highest resolution possible should be used (s. App. B). Due to the resolution of 10nm, the layer thicknesses are only accurate to within 10 nm. Also, the doped layers in the device are not explicitly defined as individual layers, due to a special behaviour of the MEEP software; the output of the dielectric properties from the software show a slight averaging between different materials, which however are not present in the simulation itself. This averaging is present for one or two pixels, which correspond to 10 nm to 20 nm, is approximately the same as the doped layers in the real device. This, combined with the fact that the optical constants of the doped layers are very similar to those of the intrinsic layers, makes these assumptions feasible.

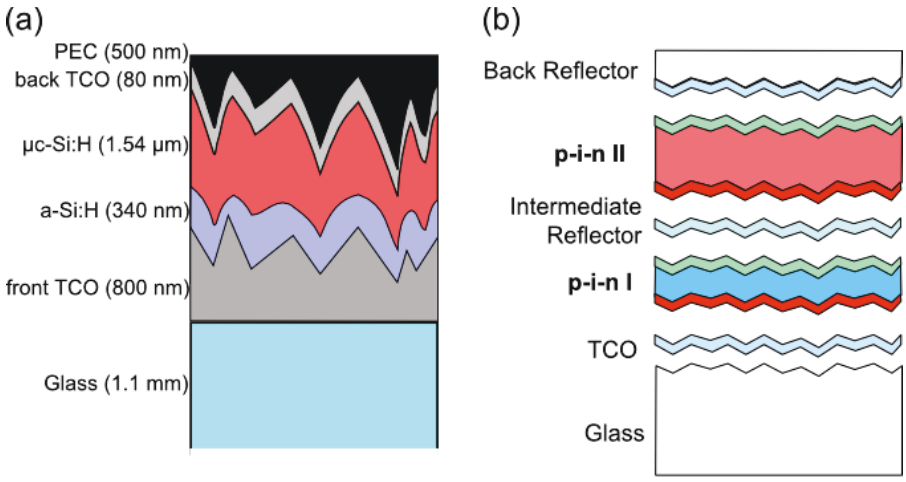

Figure 7.25.: Comparison of the layer stacks as assumed in simulation (a) and present in a real-life device (b). The simulation omits the doped layers of the p-i-n structures, since they are optically very similar to the intrinsic layer and are not recognisable in the output from the simulation software. Additionally, neither the simulation nor the real device had any intermediate reflector between top and bottom cell.

The comparison with the experiments is based on several quantities. Data from the simulation shows the EQE of both the top and bottom cell of the tandem device, while experimental data includes EQE measurements as well as reflection measurements for two different tandem cells. Using two different cells makes it possible to investigate the influence of the inaccuracies in both optical constants and layer thicknesses. Including the reflection measurement helps ascertain the influence of the glass halfspace in the simulation as opposed to a 1.1mm thick glass substrate in the real device. The results are shown in Fig. 7.26.

Looking at these results, there are three distinct wavelength regions to investigate: Firstly, in the short wavelength region, below 550 nm, we see some difference between simulation and experiment, which are mainly caused by the resolution, as discussed in App. B. Despite the comparably low resolution, however, the simulation shows very similar behaviour to the experiment.

Secondly, in the wavelength region between 550 nm and 750 nm, the agreement is very good for the a-Si:H top cell, while the μc-Si:H bottom cell shows a significantly lower EQE in the simulation.

Finally, at long wavelengths, the simulation again significantly underestimates the EQE of the bottom cell. This is caused by three effects: For one, the layer thickness assumed for the bottom cell is calculated from the deposition speed and time. While this method of obtaining a layer thickness is fast and simple, it is quite error-prone due to different deposition parameters. For example, in this case, the layer thickness is likely to be larger, which would

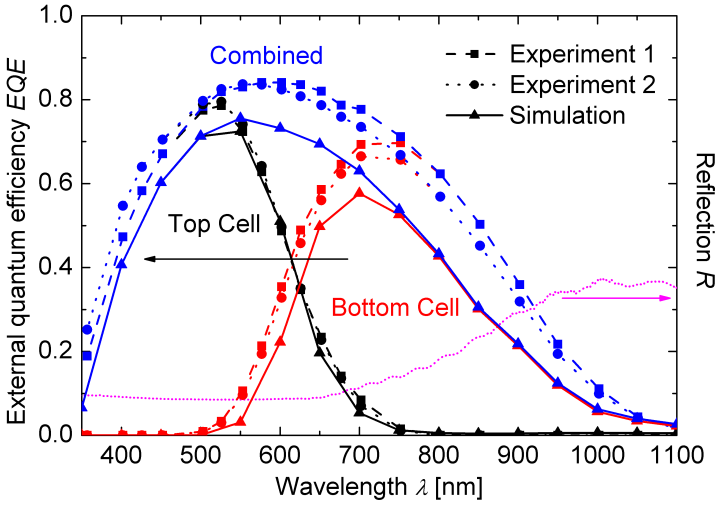

Figure 7.26.: Comparison of simulated EQE (solid line) to two measured EQEs (dashed and dotted line), as well as measured reflection data, The simulation modelled the device represented by the dashed line. Also, the reflection measurement was performed on that cell. In the short wavelength region (350 nm to 550 nm), there is an wavelength-dependent difference between experiment and simulation, which can be explained by the low resolution of 10 nm. In the middle wavelength region (600 nm to 800 nm), the agreement with the a-Si:H top cell is very good. However, the bottom cell shows strong differences in this wavelength region as well as in the long wavelength region between 850 nm and 1100 nm. The simulation significantly underestimates the EQE of the µc-Si:H bottom cell. This is caused by three effects: The real-life device is likely to have a thicker bottom cell, the optical data used in the simulation is not of the exact same layer, but taken from a different layer deposited on glass in a different deposition system, and the air/glass interface at the front of the cell is neglected in the simulation, leading to less light trapping in the long wavelength region, where the measurement shows high reflection from the device.

lead to more absorption than for the thinner simulated cell. Another factor, and likely to be the most important here, is the uncertainty in the absorption coefficient of the µc-Si:H layer. The optical data used in the simulations was obtained from a thinner µc-Si:H layer from a different deposition system. Additionally, it also shows a different crystalline volume fraction† and was deposited on glass instead of a silicon layer. The difference in crystalline volume fraction alone can lead to a factor of 1.5 difference in the absorption coefficient at wavelengths of 700 nm and above. Combined with the high number of times the light passes the bottom cell, this can show a significant impact on the EQE. The last influence on the performance of the bottom cell in the

† obtained by measuring Raman scattering

long wavelength region results from the absence of the air/glass interface at the very front of the cell. While the air/glass interface leads to low reflection losses for light incoupling, it has a much stronger impact for the light reflected from the back of the cell; the light reflected at the back contact, which can reach the glass/air interface typically does so at large angles, as investigations of light scattering have shown (Sec. 7.3. These large angles are larger than the angle of total internal reflection at that interface, therefore this light is reflected back into the device and trapped there.

These different regions are of different importance in the simulation; the short wavelength region, light incoupling and absorption in the TCO and doped layers plays a significant role. However, the trends are similar for experiment and simulation, so qualitative investigations of the performance and light incoupling at a rough surface are still valid.

In the middle wavelength region, the agreement is very good when considering all approximations for the a-Si:H top cell.

The results for the μc-Si:H bottom cell show worse agreement, which can be attributed to uncertainties of the layer thickness, assumed optical properties and neglecting of the glass/air interface.

In conclusion, the comparison for a complete tandem device has shown the validity of the assumptions made previously for the top cell, while the bottom cell needs further investigations. The next logical step would be to vary the uncertain parameters at a single wavelength to find an optimum and then apply these parameters to a whole spectrum.

8

FDTD SIMULATIONS AND NEAR-FIELD MICROSCOPY

8.1 POST-PROCESSING ALGORITHM FOR TOPOGRAPHY ARTEFACTS

As was described in the fundamentals section, SNOM measurements can be used to investigate the light intensity above a sample at a very close distance, therefore including near-field effects. The idea is that the measuring probe is at a constant distance of about 20 nm above the surface. In reality, however, the probe has a finite size and - depending on the feature sizes and shapes of the surface - cannot be placed that close above the surface at the point of measurement, lest it causes a tip crash. This effect of the offset of the real tip position from the ideal position is known as "topography artefacts" and has been examined experimentally previously.[66, 67, 68]

This is an effect also visible when comparing SNOM measurements with FDTD simulations above a textured TCO, as was shown by Rockstuhl et al.[50]. An example for this is shown in Fig. 8.1, which shows the original surface texture in (a), the SNOM measurement in (b) and the light intensity as obtained by FDTD simulations 20 nm above the surface in (c), which is equivalent to the idealised assumption of the SNOM measurement. In this case, FDTD simulation and experiment show strong differences, especially in the center of the craters. While the intensity obtained by SNOM is much smaller in the craters than at their rims, in FDTD simulations, these intensities are equally strong. This can be attributed to near-field effects, which are still clearly visible at such short distances. Figure 8.1(d) shows the light intensity from FDTD simulation at a distance of 160 nm above the surface and shows a better agreement between FDTD and SNOM, supporting the assumption that the probe is actually further away from the surface than hoped for. However, just using an empiric value for the distance between the surface and the measurement plane is both unsatisfying and hardly justifiable from a scientific point of view.

The approach closest to reality to include this effect would be to include the measurement probe in the FDTD simulation and calculate the intensity collected by it. However, a typical SNOM measurement consists of 300×300 points, and for each of these points, a simulation would have to be performed where the probe is positioned at that point in the xy-plane. This would lead

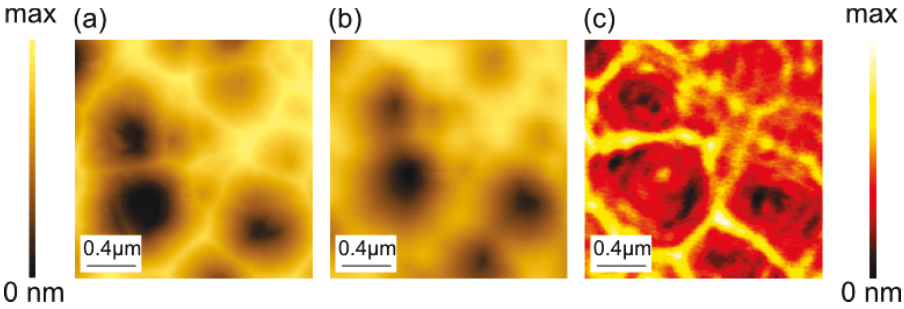

Figure 8.1.: Examples of a topography measured by AFM (a) and SNOM (b), as well as the intensity measured simultaneously by SNOM (c). The topography as measured by SNOM is blurred compared to the (sharp tip) AFM measurement. In the intensity measurement, the crater rims show a much higher intensity than the crater centres.

to a total of 90000 simulations for a complete scan and is neither feasible nor possible with today's computing performance.*

8.1.1 *The post-processing algorithm*

To address this issue, a post-processing algorithm was developed to calculate the actual distance of the probe from the surface using an idealised probe geometry and calculating the "measured" intensity from the FDTD simulation with the calculated distance. It works as follows, with (currently) all input data taken from FDTD simulation:

1. Create three-dimensional (binary) arrays of both the surface and the probe geometry. The latter can either be obtained by calculating it from a set of parameters (i.e. aperture radius, coating thickness and angle of the tip) or recreated from a measurement of the tip, such as a scanning electron micrograph image or deconvolution of the topography, measured independently by e.q. a sharp tip AFM measurement (Fig. 8.2(a)).

2. Place the centre of the tip 20 nm above the measurement point in question, as shown in Fig. 8.2(b).

3. If there is an intersection, repeat step 2, but place the probe one pixel† above its previous position and repeat until the minimal distance between surface and probe is 20 nm (Fig. 8.2(c)).

4. At this point, store the offset of the probe for this point of the texture.

* Due to the high resolution requirements, one simulation would have taken 18 hours on 32 nodes, with a maximum of 15 concurrent jobs, leading to a total execution time of 12 years and 1.6 million node hours.

† or more pixel, depending on resolution

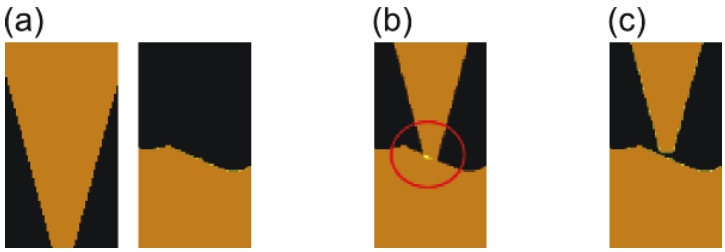

Figure 8.2.: Sketch of the algorithm used to calculate probe positions. Both the surface texture and the probe geometry, e.g. an idealised, calculated geometry (a), are stored in a three-dimensional array. At each point of the texture, the center of the tip is assumed to be 20 nm above the surface. Next, a part of the surface has to be defined in a way that adding the tip array would result in a distance of 20 nm between the center of the probe and the surface (b). Calculating the intersection of the arrays, marked with a red circle in (b), it is clear that the real position must be above this point, since anything else would result in a tip crash in the experiment. From now on, the tip is moved upward pixel by pixel, until there is no longer any intersection, as shown in (c). This point marks the offset between probe and surface. This procedure is repeated for every point of the texture. From the resulting two-dimensional array of offsets, the intensity at these offsets can be extracted from simulation data. These sketches also resemble the discretisation or pixels as used for the calculations.

Repeating this procedure for every point of the texture yields a two-dimensional array of probe offsets. These offsets can be used to extract the intensity values from the simulation, resulting in an array of intensities at the correct tip positions. This is a very simple and fast algorithm, taking between ten minutes and one hour of execution time.

But, in its simplicity with only a a few assumptions about the interaction of the probe and the surface[‡], it neglects several effects, which are encountered in the experiment:

- The offset is always calculated in a way that the distance between the probe and the surface in minimised in the direction of the probe axis, therefore the actual minimal distance between surface and probe might be slightly different.

- Any additional forces acting on the probe are neglected, such as shear forces.

- The possible influence of the probe on local light intensity is not taken into account.

‡ namely, no intersection and therefore no tip crash

We assume that, due to inaccuracies in both the experiment and the simulation model, the former two are negligible when compared to the last one. This effect has been investigated and will be discussed later.

8.1.2 *Samples*

After describing the algorithm in detail, we will describe the samples which the algorithm was applied to and which are shown in Fig. 8.3. These included two TCOs as used in thin-film silicon solar cells. A 50s etched ZnO:Al layer, the same texture being used for various other simulations (Fig. 8.3(a)), and a commercially available SnO_2:F-based AN10 substrate with pyramid-like structures, similar to Asahi-U, which is shown in Fig. 8.3(b).

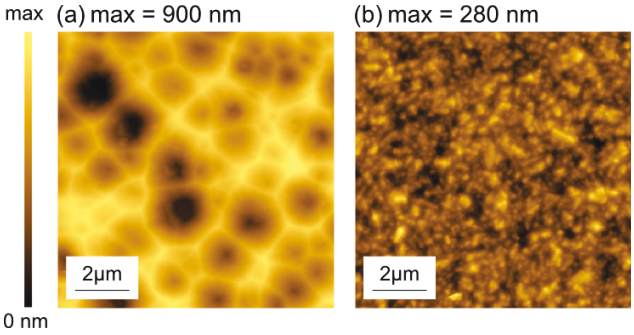

Figure 8.3.: Textures investigated with the tip algorithm. 50s etched ZnO:Al, shown in (a) and AN10 substrate, shown in (b). The former shows the known crater-like structures, while the latter exhibits pyramid-like structures, similar to Asahi-U.

The FDTD simulations were again simulated using a 10µm × 10µm AFM scan with a resolution of 20 nm.

For each of the samples, the algorithm was applied with two different probe geometries, approximating both a good and a bad tip. Figure 8.4(a) shows the approximation of a good tip, with an aperture radius 40 nm, a coating thickness of 80 nm and an angle of 15°, while the bad tip, as seen in Fig. 8.4(b) was assumed with an aperture radius of 80 nm, a coating thickness of 120 nm and an angle of 25°.

8.1.3 *Offset Maps*

As a first result and basis for all further investigations obtained with the algorithm, the maps of the offset between surface and probe will be investigated. The combination of original topography and offset maps will be compared to the SNOM topography signal, and the offset maps itself will be compared with the surface angle distribution of the samples.

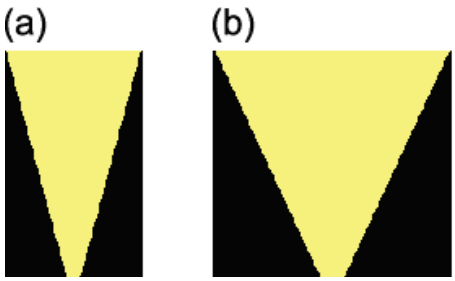

Figure 8.4.: Cross-sections of the tip geometries: The idealised shape of the probe is assumed to be a truncated cone. (a) shows an approximation of a good SNOM probe, with an aperture radius of 40 nm, a coating thickness of 80 nm and an angle of 15°. (b) shows a presumably bad tip, with an aperture radius of 80 nm, a coating thickness of 120 nm and an angle of 25°.

Firstly, the ZnO:Al sample was investigated using both probe geometries; the results are shown in Fig. 8.5. Figure 8.5(a) shows again the topography obtained by AFM. (b) shows the topography measurement of the SNOM. There is a noticeable difference in the height values obtained by AFM and SNOM, due to a non-perfect *z*-calibration of the SNOM at the time of the measurement. Figure 8.5(c) and (d) show the sum of the original topography and the offsets obtained by the algorithm for the good and bad tip geometries, respectively. As can be seen, the good probe geometry shows the best agreement between simulation and experiment, while the bad probe geometry blurs the measurement much further than the experiment.

Additionally, Fig. 8.5(e) and (f) shows the surface angle distribution of the sample and the offset of the probe for the good probe geometry, respectively. The offset correlates with the surface angle in a way that steep angles lead to a higher offset. This is clear due to the fact that the tip has to be positioned higher as to not crash into the surface at these positions.

Looking at the topography of the AN10 sample (Fig. 8.6, the first observation is that an exact mapping of the AFM measurement to the SNOM measurement is challenging due to the small features, which are all quite similar and thoroughly blurred by the SNOM measurement and the algorithm. For that reason, we focus on the qualitative agreement of the results. In Fig. 8.6(a), the original texture is shown as obtained by AFM, while *b(shows the topography as measured by SNOM. (c) and (d) show the topography after applying the algorithm for a good and bad tip, respectively. This time, the features of the original texture are strongly blurred and rounded off in the experiment. The results from the calculation show similar behaviour when applying the algorithm for both the good and bad tip geometry, with the bad geometry showing better agreement. However, the true probe geometry should again be between those two. This blurring, as expected, is due to the small feature size of this TCO and the comparatively large probe.

When comparing the surface angles with the obtained probe offset for the bad tip (Fig. 8.6(e) and (f), respectively(, this sample behaviour is clearly dom-

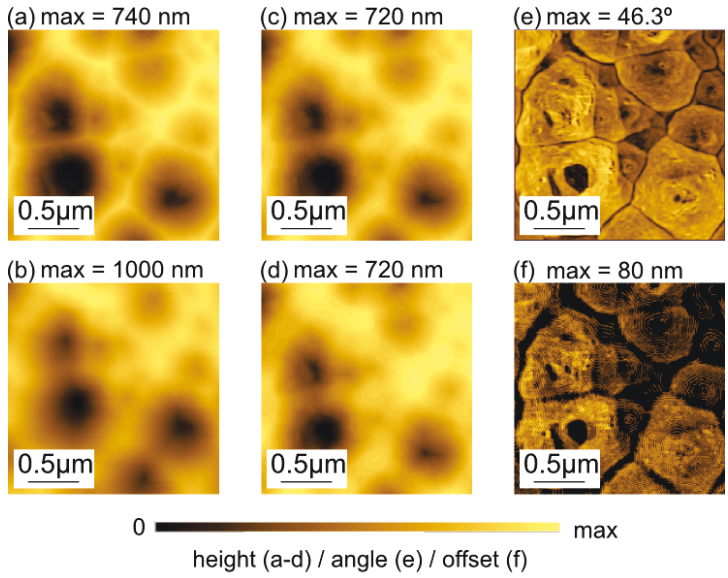

Figure 8.5.: Topographies, surface angle distribution and offsets obtained by the algorithm for the ZnO:Al sample. (a) shows the topography as obtained by AFM measurement, (b) is the topography signal of the SNOM. The offset between AFM and SNOM can be explained by a non-perfect z-calibration of the SNOM. (c) and (d) show the topography of the surface after application of the algorithm for the good and bad probe, respectively. It is visible that the good probe shows a slightly better resemblance to the SNOM than the bad probe geometry. However, an actual tip geometry is likely to be somewhere in between those two. (e) shows the surface angle distribution obtained from the AFM scan. (f) shows the offsets obtained for the good probe geometry. These offsets correlate well with the surface angle distribution.

inated by the dimensions of the tip; while in some areas, the correlation between surface angle and offset is visible, many of the smaller variations in the surface angle are not resolved with the bad probe geometry.

Taking all calculations into account, our algorithm results in realistic offsets from the sample surface and reproduces the topography measured by SNOM well. While this is still dependent on the assumed probe geometry, the algorithm is fast enough to optimize the tip geometry to give the best agreement with the experiment.

8.1.4 *Intensity Maps*

After comparing the measured topographies from SNOM with those obtained by adding the offset from the algorithm to the AFM scan, we now compare the

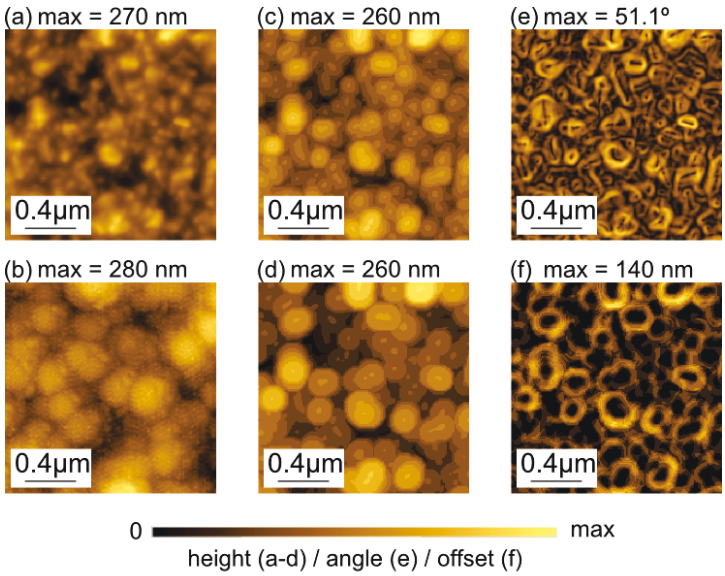

Figure 8.6.: Topographies, surface angle distribution and offset obtained by the algorithm for the AN10 sample. (a) shows the topography as obtained by AFM, (b) is the topography signal of the SNOM. (c) and (d) show the topography of the surface after the application of the algorithm for the good and bad probe geometry, respectively. It is visible that the general feature size is better represented by the bad tip. The strong discretisation results from the FDTD resolution of 20 nm. (e) shows the surface angle distribution obtained from the AFM, (f) shows the offsets obtained for the bad probe geometry. Again, the features are similar to those of the surface angle distribution. However, small features in the angle distribution are not visible due to the large dimensions of the probe.

light intensity at 750 nm measured via SNOM with that obtained by the FDTD simulation.

Looking again at the ZnO:Al sample, there are three quantities which need to be compared to the experiment:

- The intensity distribution as measured by SNOM, shown in Fig. 8.7(a). Ideally, this should be reproduced by using the algorithm.

- The intensity distribution 20 nm above the surface, as extracted from simulation, which is displayed in Fig. 8.7(b).
  This represents the measurement with an ideal, infinitely small tip and would include the most information about the near-field effects of the surface. As can be seen, the agreement between the experiment and the simulation is not very good. There are many interferences and near-field effects visible in the simulation, which are not to be seen in the actual measurement. Especially the contrast between the intensity of the crater

rims and the centres of the craters is much smaller directly above the surface. This lack of near-field effects in the measurement also indicates a higher position of the probe above the surface.

- The intensity distribution extracted from the simulation when including the offset from the algorithm for the good and bad tip geometry, shown in Fig. 8.7(c) and (d), respectively.
  Here, the agreement between experiment and simulation is much better than for the original assumption (Fig. 8.7(b)), exhibiting the same high intensities at the crater rims while showing some interferences in the crater centres. Additionally, as with the experiment, the intensity distribution at craters smaller than the probe are strongly blurred.

For the intensity distributions of the AN10 sample, which are shown in Fig. 8.8, obtained by SNOM and FDTD simulation after deploying the algorithm, it is hard to judge which intensity distribution is closest to the experiment, for several reasons:

- The experiment, shown in Fig. 8.8(a), shows quite a bit of noise.
- None of the intensity distributions show distinctive features which could be compared.
- The intensity distribution above the surface (Fig. 8.8(b)), as well as those obtained by the algorithm (Fig. 8.8(c) for the good and (d) for the bad tip geometry) are very similar in all aspects.

However, it can be stated that the agreement is still enhanced by using the algorithm. When also taking into account the tip aperture, shown in Fig. 8.8(e) and (f) for the good and bad tip geometry, respectively.

To quantify the agreement between simulation and experiment, a FFT analysis of the intensity distribution was performed. These are shown in Fig. 8.9.

In conclusion, we have shown the strong influence of topography artefacts on SNOM measurements, especially in the case of surface features smaller than the actual dimensions of the scanning probe, by using FDTD simulations combined with actual experiments. We also introduced a fast and simple algorithm to calculate the topography artefacts that can be expected from SNOM measurements. For this, only an AFM scan and a tip geometry are necessary, the latter being either calculated from a set of parameters using an idealised truncated cone as geometry, or imported from actual measurements of the probe geometry. The results from this algorithm can then be applied to an intensity distribution obtained by simulation. Since the agreement between the intensity distribution obtained by experiment and simulation combined with the algorithm is good for the investigated structures, one can assume the intensity distribution of the simulation to be correct in the area between the probe and the surface as well. Furthermore, it can be concluded that the impact of the tip on local light intensity is of minor importance, at least for the dielectric

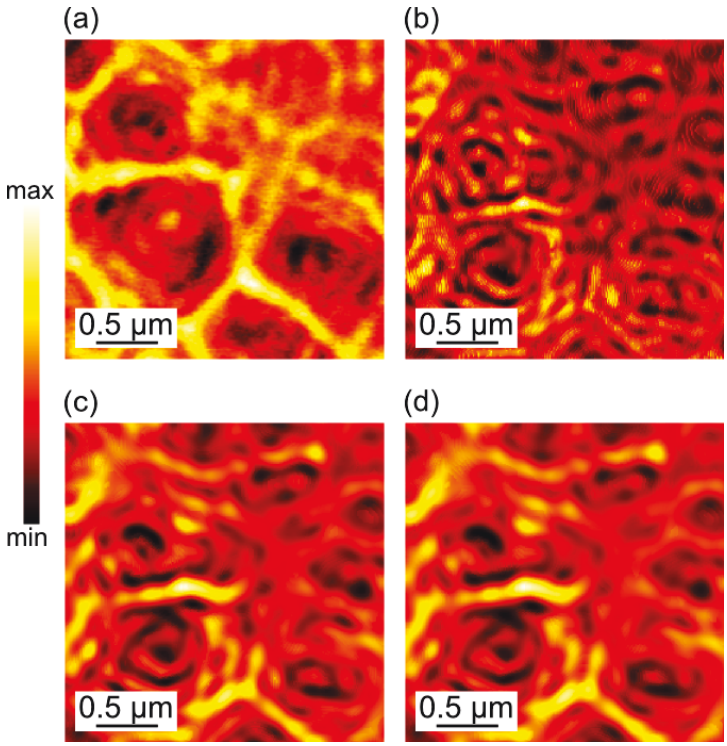

Figure 8.7.: Light intensity distribution from SNOM measurements and FDTD simulation of the ZnO:Al sample. (a) shows the intensity distribution as measured by SNOM. A high light intensity is observed at nearly all crater rims. (b) shows the intensity distribution from FDTD simulation at a constant distance of 20 nm above the sample surface. There are many interferences visible, as well as features that relate to near-field effects. In contrast to the measurement, the crater rims do not exhibit a much higher intensity than the crater centres. (c) and (d) show the light intensity distributions obtained when taking into account the offsets obtained from the algorithm (Fig. 8.5(f) for the good geometry), respectively. The agreement with the measurement is much better, especially for the good probe geometry, as can be seen for the features in the top right. The crater rims are better visible in the measurement as well as for the good probe geometry.

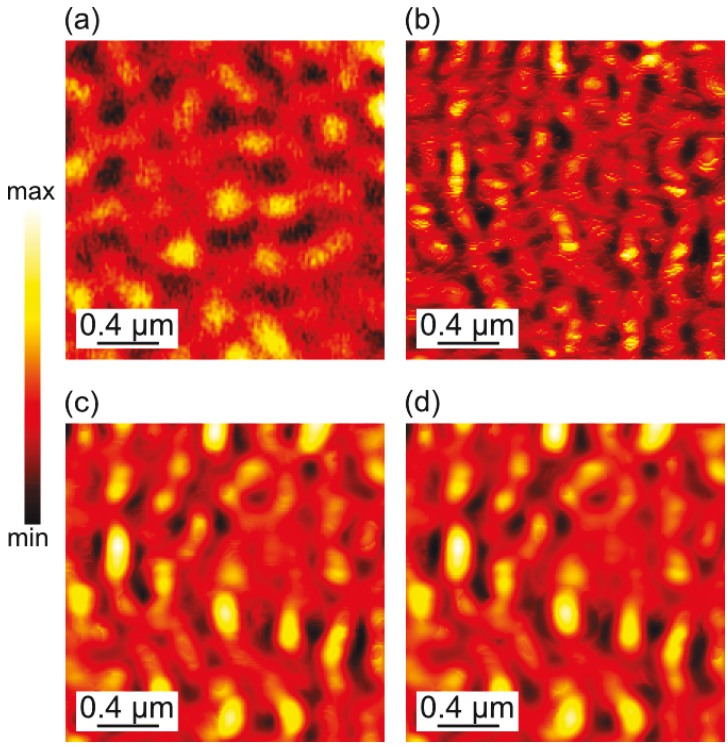

Figure 8.8.: Light intensity distributions from SNOM measurement and FDTD simulation of the AN10 sample. (a) shows the intensity distribution as measured by SNOM. The shape of the features in this distribution is similar to those seen in the topography measurement (Fig. 8.6(a)). (b) shows the intensity distribution from FDTD simulation at a constant distance of 20 nm above the surface. There are many smaller features visible, as well as features that relate to near-field effects. (c) and (d) show the light intensity distribution obtained when taking into account the offsets obtained by the algorithm (Fig. 8.6(f) for the bad geometry). The agreement with the SNOM measurement is better for both geometries.

materials investigated here. This again gives more insight into the near-field effects of the simulated sample than the measurement alone can do. Given the input data of this algorithm, it can be applied to various simulation methods, as long as the result is an intensity distribution of the system.

8.2 INCORPORATING THE NEAR-FIELD TIP INTO SIMULATIONS

8.2.1 *Collecting tip over an idealised crater*

As final part of the investigation of the SNOM tip on light propagation above a textured surface, an idealised crater structure was created, with planar illu-

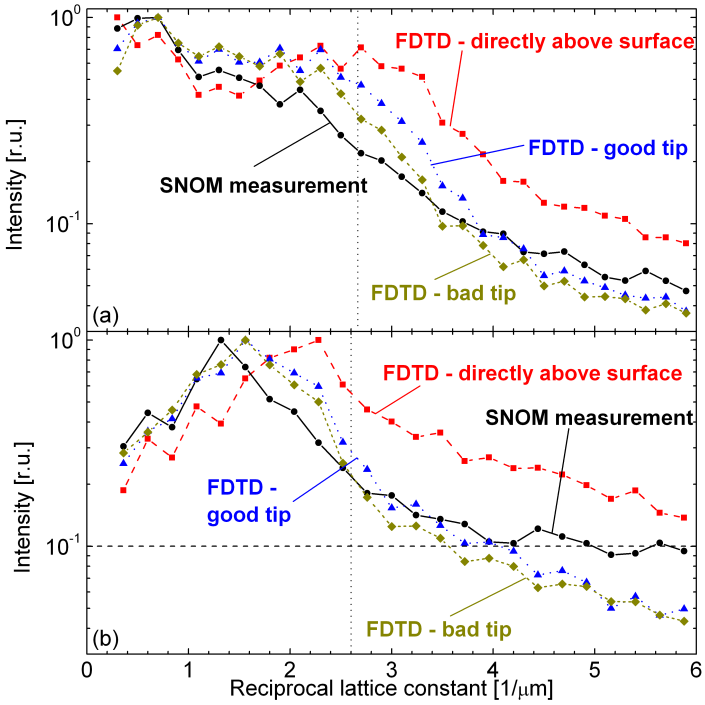

Figure 8.9.: Intensity vs. reciprocal lattice constant obtained by FFT of the intensity distribution of the ZnO:Al(a) and AN10(b) sample. The dotted line indicates the transition from propagating to evanescent intensity. For the ZnO:Al sample, the trends in the propagating part are very similar for the measurements as well as all intensity distributions obtained by FDTD. In the evanescent region, however, the inclusion of the tip significantly improves agreement with the measurement, while the intensity directly above the surface indicates a strong over-estimation of the evanescent intensity. For the AN10 sample (b), the overall result is similar. However, due to the small feature size and the comparatively large tip, the FDTD results directly above the surface lead to a shift of the propagating peak to higher reciprocal lattice constant. This can be explained by the fact that the sharp features are blurred by the large tip and lead to smaller angles when analysed by FFT. Additionally, the measurement only drops to 10^{-1} in the evanescent region due to high noise.

mination through the substrate and intensity collection through an idealised SNOM tip. The aim of this investigation is to look into the effects of light scattering at the SNOM tip and its influence on light collection through the tip. These collected light intensities were compared to a simulation without a SNOM tip, looking at the normalised intensities at different positions. A top-down view and a cross-section of the idealised crater are shown in Fig. 8.10(a) and (b), respectively.

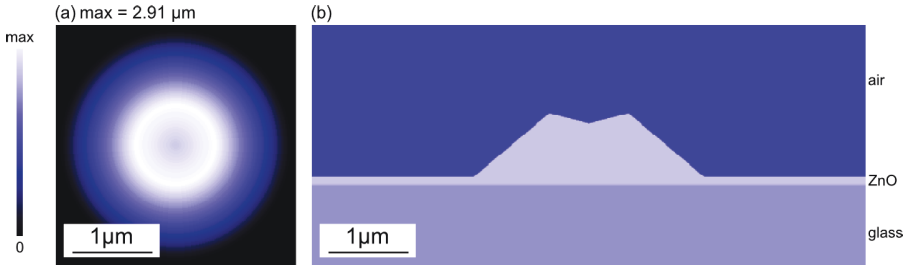

Figure 8.10.: Sketch of the crater used for investigating the influence of the SNOM tip; (a) shows a top-down view of the crater. It is assumed to be rotationally symmetric, with an inner (crater centre to rim) radius of 500 nm. (b) shows a cross-section of the crater. The inner and outer angles of the crater were set to 65° and 55°, respectively.

As shown in Fig. 8.10cd , the crater was described as perfectly circular, with a slope of 55° at the outside and 65° at the inner slope. The distance between the centre of the crater and the rim, or crater radius, was assumed to be 500 nm. This leads to a crater similar to those typically observed in a wet-etched ZnO:Al sample, as used in previous sections. The simulation itself was, as mentioned earlier, performed with a resolution of 10 nm due to the small tip aperture. Additionally, to suppress artefacts caused by periodic boundaries, open boundary conditions were assumed in all directions. To facilitate this, PMLs were added on each side. This additional thickness in all directions, along with the necessity to simulate at least 1 µm of SNOM tip, resulted in a computational domain of approximately 700x700x500 cells. Additionally, to address for possible polarisation effects, each simulation was performed for both cardinal polarisation directions (E_y and E_z), and the resulting *intensity* added and compared to each polarisation to investigate possible polarisation effects from the field distribution. However, investigations of the polarisation effects have shown that the simulation of a single polarisation direction (E_z) showed the best agreement. This is also supported by the fact that the algorithm presented in Sec. 8.1 yielded the best results when assuming the incident light to be linearly polarised.

To differentiate between the effects of the tip position as described in Sec. 8.1, the simulation was two-fold:

1. The baseline: The system was simulated without the SNOM tip included in the model. This simulation yielded results for light propagation undis-

turbed by the tip itself. This will also be referred to as the "undisturbed" system.

2. The simulations including the tip: These simulations represent the actual measurement with a SNOM as closely as possible. In a line between the centre of the crater and the outer flank of the crater, simulations were performed for points with a distance of 30 nm. At each of these points, a metal-coated glass tip was positioned in a way that the minimal distance between the surface and the tip was between 20 nm and 30 nm, in analogy to Sec. 8.1. The tip itself was also modelled in the same way as for the algorithm presented earlier. These simulations will also be referred to as "disturbed" system.

This lead to a total of 50 simulations, two for the baseline and 48 for the simulations including the tip. Intensity distribution in a cross-section through the centre of the crater (and tip) are shown in Fig. 8.11 for simulations without a tip (a), with the tip at the centre of the crater (b) and above the rim of the crater (c). It is clearly visible that the tip has a significant impact on light propagation and scattering in its close vicinity above the layer. This is especially visible for the "flare" visible above the centre of the crater in the undisturbed system. The presence of the tip above the centre, in the same position the flare is originally found, suppresses it completely (Fig. 8.11(b)). In the case of the tip being positioned above the crater rim (Fig. 8.11(c)), the flare is visible, but it is diverted along the side of the tip. This effects is caused largely by the metal coating of the tip; in these simulations, it is even more pronounced than would be expected in the experiment, since the PEC coating does not allow for any light propagation inside the coating.

However, the light intensity inside the layer shows little dependence on the presence of the tip. The same holds true for light propagation above the surface at even small distances from the tip. For example, the small features at the outer crater flank are hardly disturbed at all by the presence of the tip. While this supports the claims of the previous section (Sec. 8.1), some questions remain:

- Does the light, which is coupled into the tip, reach the optical fibre and therefore the detector?
- What influence does the presence of the tip have on the actual measurement?
- Are the relative ratios between the different measurement points influenced by the presence of the SNOM tip?

The answer to the first question essentially is an indicator if the measurement, and especially the tip, is modelled realistically in the simulation. For this, the total intensity in the three layers of the tip closest to the surface were compared to the total intensity at the three layers closest to the PML. These values were normalised to their respective maxima, and the results are shown

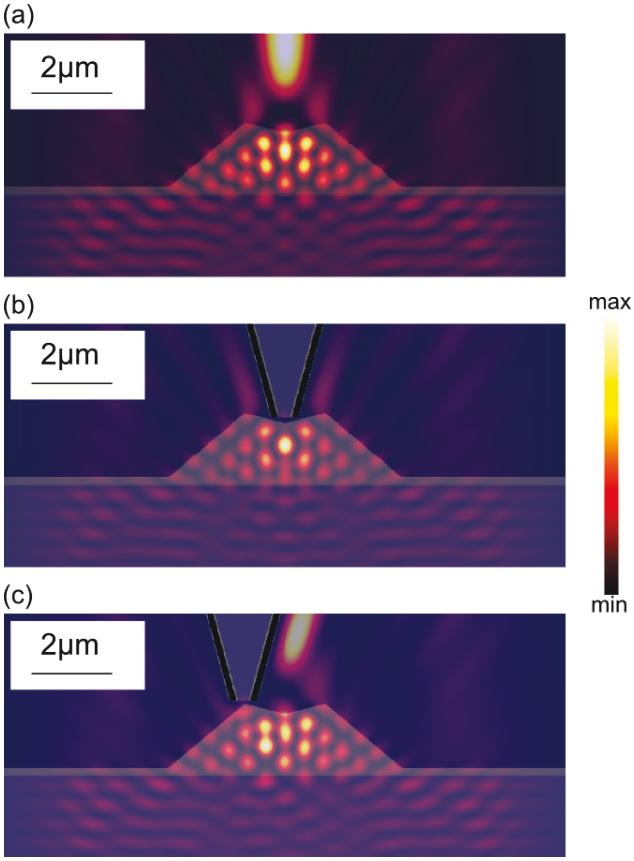

Figure 8.11.: Intensity distributions for an idealised ZnO:Al crater, without a SNOM tip (a), with a SNOM tip above the centre (b), and with the tip placed above the crater rim (c). The presence of the tip changes the light propagation in its close vicinity. For example, the flare above the crater centre is suppressed in (b) and diverted in (c). However, the intensity distribution inside the layer and further away from the tip is hardly affected at all. However, the "flare" visible above the centre of the crater in the undisturbed system is modified by the tip; in (b), it is not visible at all due to the tip being in its place, while in (c), the flare is diverted due to the metal coating of the tip.

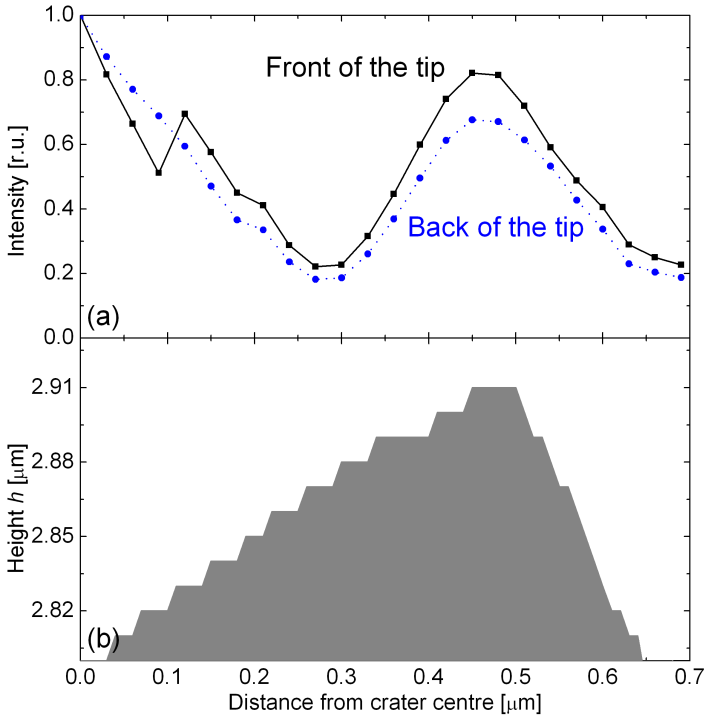

Figure 8.12.: Intensities at the front (solid) and back (dotted) of the SNOM tip for each position (a) and shape of the crater as approximated in FDTD simulation (b). The good agreement indicates a good light incoupling into the tip.

in Fig. 8.12. As can be seen, the relative intensity is nearly identical at all but the smallest distances from the surface at the front and the back of the tip. This indicates a good approximation of the measurement configuration as far as light incoupling is concerned. The differences at the crater centre can be explained by numerical noise in the simulation.

As to the second question, this was already discussed for Fig. 8.11. Another influence on this can be found in the difference between the intensity at the surface and the actual posittion of the tip, as obtained with the algorithm described in the previous section (Sec. 8.1). To investigate this influence, there are two possible comparisons, are shown in Fig. 8.13 and Fig. 8.14.

Figure 8.13 shows the comparison of intensities at the surface with a tip and the intensity inside the tip, both for the disturbed system. These curves are nearly identical for all tip positions, indicating that the tip actually measures the intensity directly above the surface. However, it cannot be ruled out that there might be differences on a smaller scale, since the point-to-point distance is 30 nm.

When looking at this good agreement, however, one has to keep in mind that the measured intensity only agrees with the intensity at the surface *when the*

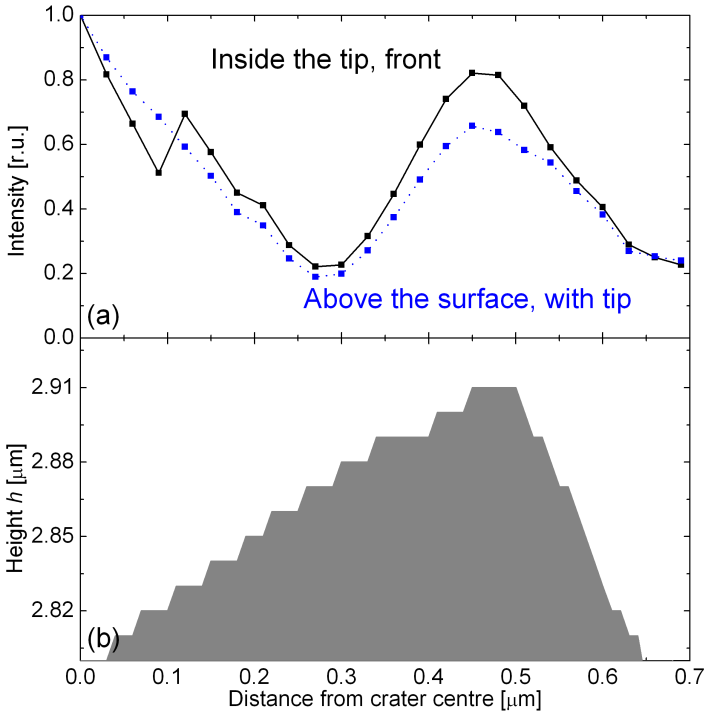

Figure 8.13.: Intensity directly above the surface (dotted) and inside the tip (solid) for simulations of the disturbed system (a) and shape of the crater as approximated in FDTD simulation (b). These curves are nearly identical. This indicated that the SNOM actually measures the intensity directly above the surface for the disturbed system. This, however, does not give any clues as to the results of the undisturbed system, which is shown in Fig. 8.14.

tip is present. The question arising is if the intended measurement should yield results for this system *including* the tip or if information about the *undisturbed* system is sought.

In the case of the thin films investigated here, the latter is the case, since the layers are incorporated in the solar devices without any metal tip. So a comparison is necessary between the intensity at the surface and the intensity at the position of the tip, both for the simulation of the undisturbed system, as well as the intensity inside the tip at the different positions (disturbed system). This is shown in Fig. 8.14.

When first comparing the intensities above the surface and at the tip positions for the undisturbed system, we see a significant difference between the intensity above the surface of the undisturbed system, and the intensity as collected by the simulated tip. This difference is in accordance with the results shown in the previous section (Sec. 8.1), which showed strong indications that the SNOM does not measure the intensity directly above the surface. The assumptions in the algorithm are also supported when looking at the agreement

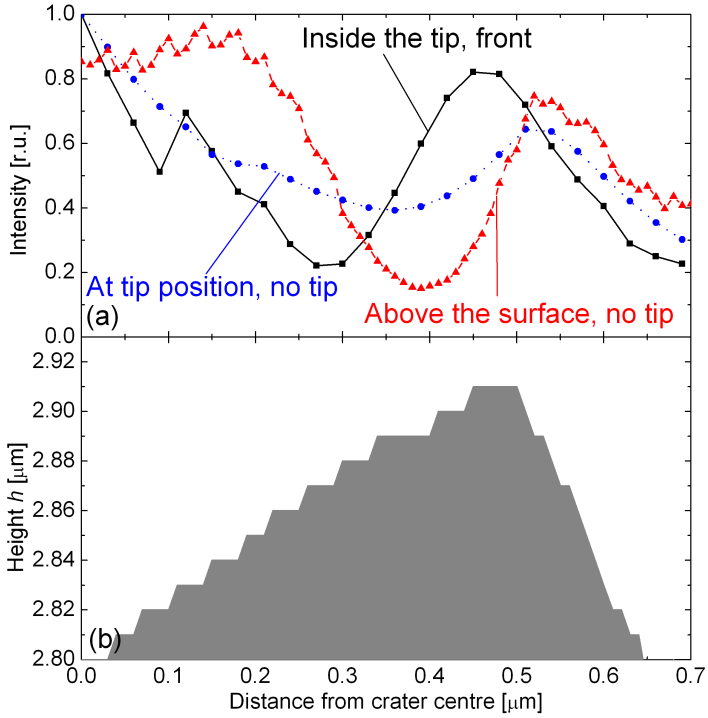

Figure 8.14.: Comparison between the measured intensity (solid), the intensity of the undisturbed system at the actual tip positions (dotted) and directly above the surface in the undisturbed system (dashed) (a) and shape of the crater as approximated in FDTD simulation (b). While there are similarities between the intensity at the tip positions and the intensity above the surface, the small features directly above the surface are not reproduced, since they result from near-field effects. Comparing the intensity at the tip positions with the actual (simulated) measurement, the shape is very similar, with a slight shift. This shift can be explained due to the aperture radius of 80 nm. Due to this, light can couple into the fibre approximately 80 nm before the centre of the aperture is above the point of interest, correlating very well with this shift.

between the intensity as collected in the tip (solid line) and the intensity of the undisturbed system at the position of the tip (dotted line). While the extrema are more pronounced in the disturbed system, the shape is very similar, with a small shift between 60 nm and 90 nm, with the tip registering the maximum before the tip is positioned directly above it. This is easily explained with the size of the aperture, which was assumed with a radius of 80 nm. Due to this radius, there is already a portion of the fibre above the maximum, so the light can couple into the fibre. Another difference is the shape of the maximum, which is much more symmetric in case of the tip. This is also caused by the finite size of the tip, since it collects intensity from a certain area.

Interestingly, even the small shoulder at a position between 0.18 µm and 0.21 µm is visible in both the simulation of the disturbed and undisturbed system, further supporting the claim that the inclusion of the tip is not necessary. When looking at the intensity directly above the surface (Fig. 8.14, dashed line), we see may smaller features, which are neither visible in the measurement nor in the undisturbed system at the actual tip positions. Since these small features are very likely to be near-field effects, this is to be expected. Due to the exponential decay of intensities, they are not visible at the actual tip positions. Additionally, the resolution of the measurement is on the same scale as the size of these smaller features. So in the experiment, these features are extremely difficult to measure.

However, while the agreement between undisturbed and disturbed system is very good in this example, there are still some assumptions in these simulations due to the limitations of the simulation software, which should be addressed in the future:

1. The resolution is limited to 10 nm, while a higher resolution would be beneficial, especially for approximating the structure of both the crater and the tip.

2. The tip is assumed to be coated with a perfect conductor. In a real-life experiment, this is of course not the case. A non-perfect metal can lead to additional disturbances in the light propagation as well as light guidance effects along the metal coating. This effect is especially important when also investigating the shape of the tip:

3. The shape of the real-life tip is not a perfect truncated cone. The front of the tip is in most cases rounded off, and the metal coating shows many protrusions in this area. Depending on size and wavelength of the incident light, this can lead to plasmonic effects modifying the intensity above the surface as well as light incoupling into the tip.

4. The structure investigated here is an idealised crater; it is rotationally symmetric and the outside of the crater lies much deeper than the centre of the crater. While the latter can be the case for specific areas of a typical wet-etched ZnO:Al, the former is hardly valid at all.

5. The exact incoupling into the fibre has been assumed to be equal at all points of the tip, while a weighted incoupling depending on the distance from the aperture centre is possible.

8.2.2 *Conclusion*

The investigation of the influence of the SNOM tip on light propagation and the measurement itself has shown a fast and easy way to compare simulations and measurements. The first part of this investigation, discussed in Sec. 8.1, which used a simple approach, has already indicated a strong influence of the tip *position* on the measurement, with the agreement between simulation and experiment improved significantly. This was the case both qualitatively, as shown in the topography and intensity plots (Fig. 8.5-Fig. 8.7, and quantitatively, as in Fig. 8.9.

These results led to the more computation intense approach of including the tip in the simulation domain, to check these results. It was found that light propagation at and in the vicinity of the tip is influenced by the presence of the tip. However, the intensity coupling into the fibre correlated very well with the intensity at the assumed tip position in the system *without* the tip. The only visible difference was a shift of the observer intensity maximum at the crater rim. This was shifted in the direction of the crater centre, which could easily be explained by the finite size of the tip. Due to this finite size, a part of the aperture is already above the maximum, while the assumed tip position (indicated by the centre of the aperture), is still closer to the crater centre. The surface features of a system *without* a tip could not be reproduced by the simulated measurement, which agrees well with the actual experiment, where far less near-field effects are visible than would be expected directly above the surface. All these results further supported the claim that taking into account the tip position in a post-processing step is sufficient to address the influence of the tip on measurements.

Part III

SUMMARY AND OUTLOOK

9

SUMMARY

The first results of light scattering simulations have shown a remarkable agreement between the rigorous, time- and memory-consuming simulations using the FDTD method and the simple and very fast phase model for single interfaces. To investigate its predictive power for multi-layered systems such as a solar cell, the light scattering of different interfaces in transmission and complete nip-type solar cells was performed. With the agreement of the light scattering calculations in reflection, a very promising way to reduce the amount of simulations necessary to find good textures for use in solar cells was found. The PM introduced by Dominé and extended by K. Bittkau has proven to give a good predictive power even for the performance of a whole solar cell, as long as the intrinsic layer is not significantly smaller than the wavelength of the incident light. For this case, investigations by J. Hinojosa [69], who implemented this model in a one-dimensional simulation software, have shown strong deviations for small layer thicknesses, such as observed in a-Si:H devices. Further investigations including the textures optimised by Fourier analysis, presented in Sec. 7.3 have supported this claim. With these investigations, compared with measurements of actual devices have shown the importance of light scattering at the back side of the absorber material for cell performance, since in the area of light trapping between 600 nm and 1100 nm, the polishing of the front side of a solar cell has shown little impact on the EQE.

An important aspect with impact on actual device deposition was the investigation of the influence of silicon growth on the texture at the back side of the cell. We have shown that the growth behaviour of amorphous silicon is not beneficial for cell performance, since the originally sharp features are getting significantly rounder with increasing film thickness, therefore not as good for scattering the light into large angles. The opposite effect has been shown for the growth of microcrystalline silicon. The additional small and sharp features obtained due to crystallite growth have proven beneficial, especially for the performance of the cell in the long wavelength region. It was also shown that this texture can improve light incoupling and therefore cell performance in the short wavelength region. It should be possible to investigate this effect in the future by replicating such a texture on the front side using nano-imprint lithography. The feasibility of using nano-imprint lithography in nip-type μc-Si:H single junction cells has been discussed by U. Paetzold[33] and should be investigated for nip-type tandem solar cells with the structures proposed in this thesis.

The investigation of absorption enhancements in various systems have further strengthened the results already likely from the investigation of light scattering. The simple texture modifications in Sec. 7.2 have shown the positive influence of sharp features and steep flanks for light trapping even in very thin structures. Looking at the absorption planes also identified certain features to lead to a generally higher absorption in the material. While at the time this research was done it was a purely theoretical problem, the progress in nanoimprint lithography could help to utilise these effects as well in the mid- to long-term.

With the positive influence of the simple modifications, a more sophisticated approach was considered and finally led to the texture optimised using Fourier analysis. While the light scattering effects have been mentioned above, it has to be stated again that the FDTD simulations have confirmed these effects in respect to the absorption enhancement inside the cell and have shown a linear relation between the light scattered into angles larger than the angle of total internal reflection in transmission and reflection, at least for certain structures. This predictive power of a very simple model can help to reduce computing time requirements and focus on only the most promising structures.

Simulations of the complete tandem cell have shown limitations of the simulation software; in the short wavelength region, the low resolution became clearly visible, while in the long wavelength region the consequences of neglecting the first air/glass interface (by assuming a glass halfspace) became apparent. In the intermediate wavelength region between 500 nm and 750 nm, however, the agreement was very good. This region is extremely important for the performance of a tandem device, since here the light absorption shifts from the a-Si:H top cell to the μc-Si:H bottom cell. Additionally, while absolute values showed some differences in the short and long wavelength region, the shape of the EQE was reproduced very well.

The last part of the thesis, the investigation of the near-field tip via simulation has also proven worthwhile, since it was possible to explain many effects seen in the experiment. While this research was only partly related to the performance of solar cells, its impact is not limited to this field.

The presented algorithm to reconstruct SNOM topography and intensity measurements via a fast and simple post-processing algorithm has proven to be a tool with which the differences between simulation (without tip) and experiment can at least be partially explained. Adding the SNOM-tip to the simulation domain has provided further insight into the fundamental processes of light propagation in the experiment.

Further investigations of the SNOM measurements via simulations have shown that the influence of the SNOM tip on the measured light intensity is dominated by the actual position of the tip during measurements. Addressing this position via the afore-mentioned algorithm proved to be sufficient to significantly increase agreement between the measurement and simulation. Even more importantly, the simulations including the SNOM tip have shown that the light propagation inside the investigated layers is hardly affected by the presence of the tip. This is extremely important, since for the application of

these layers in solar cells, the light intensity inside the layer is crucial, and the measurement allows for assumptions of the light propagation inside the layer.

10

OUTLOOK

For the future, the research presented in this thesis open up many possibilities; the investigation of light scattering can be extended to a myriad different textures various scientific areas. First and foremost it would be extremely interesting to investigate the validity of the phase model for multiple interfaces. It is important to find the layer thickness below which the far-field approximation reaches its limit and where it fails completely. It would also be intriguing if the results found in the course of this thesis are applicable for other devices in which light in- and out-coupling and light scattering play an important role, such as LEDs.

Adding in the results from the absorption enhancements from different textures and texture combinations, the question arises if there are other texture that can be optimised or even if there are more complex ways of optimising topographies even further. With ever-ongoing advances in the fabrication of specific textures, this can prove to be a way to further increase the efficiency of Si-based thin-film solar cells. While these fabrication methods are time-consuming and therefore expensive at this point in time, it is very likely that these methods will become faster in the future. The comparison of simulation and experiment for the complete tandem cell have shown some limitations of the simulation and the assumptions made therein; further investigations regarding the real film thicknesses, the optical data of the μc-Si:H bottom cell and the investigations of the glass/air interface are necessary. The next steps could include the variation of these parameters for a single wavelength. The resulting optimal parameters can then be used to simulate a whole spectrum and compare the results again.

While the investigations of the effect of the SNOM tip on measurements has shown that the effect of the tip on light scattering and propagation is negligible compared to the actual position of the tip, further investigations concerning the correct geometry of the tip as well as a realistic dielectric function of the metal coating are in order. This might improve the agreement even further. However, due to the high computational requirements of these investigations, it should be seen as a fundamental research, while for everyday use, the presented algorithm is sufficient.

Part IV

APPENDIX

A

DOCUMENTATION FOR THE SIMULATION SOFTWARE

The software used in this thesis, with its functionality described in Sec. 3.1, was developed to be usable on systems with varying resources, from single workstations up to large HPC clusters. The current version (meep-cpp 1.0, October 12, 2015), can simply be used with the command
meep-cpp $<$ config$-$file $>$. This configuration file, which has to be defined for each simulation contains several parameters. A configuration file including all possible parameters is shown in the following listing:

```
1  NumberOfLayers=4;
2  MultiProfile=n;
3  Size=10;12;12;
4  SubstSize=0.2;
5  SubstDielReal=-1e20;
6  SubstDielImag=0.0;
7  MaxTime=80;
8  Frequency=1.333333333;
9  Resolution=100;
10 LayerDielReal=-1e20;3.17773;11.102422;3.17773;
11 LayerDielImag=-1e20;0.056903;0.055179;0.056903;
12 Thicknesses=0.02;0.08;1.13;0.08;
13 HeightFiles=tilt.dat;
14 PMLThickness=1.0;
15 DefaultDielReal=1.0;
16 DefaultDielImag=0;
17 OutputEpsilon=y;
18 OutputEfield=y;
19 OutputPoynting=n;
20 IncludeTip=y;
21 TipPosition=3.52;8.0;8.0;
22 FiberRadius=0.08;
23 CoatingThickness=0.1;
24 OpeningAngle=15;
25 FiberEps=2.25;
26 IlluminateTip=y;
27 PolDirection=Ez;
28 PeriodicBoundary=n;
```

```
29 TipAreaSource=n;
30 BigDomain=y;
31 EpsAverage=n;
32 TimeInc=0;
```

This is the same simulation file used for the investigation of the illuminating SNOM tip over a flat nip-like structure as investigated for S. Lehnen. The configuration parameters are explained in the following list:

- NumberOfLayers (integer) Number of layers on top of the substrate. Default: n/a
- MultiProfile (boolean) Use different texture files for each interface. Default: false (n)
- Size (List of integer) The size of the simulated system in x, y and z direction, including the perfectly matched layers. Size unit is arbitrary, but in the course of this thesis always in μm. Default: n/a
- SubstSize (float) Thickness of the substrate in size units. Default: 1.5
- SubstDielReal (float) Real part of the dielectric function of the substrate. Default: n/a
- SubstDielImag (float) Imaginary part of the dielectric function of the substrate. Default: n/a
- MaxTime (float) Time at which the simulation should be stopped. One time unit equals $2 \cdot$ Resolution timesteps. Default: n/a
- Frequency (float) Frequency of the incident light. Wavelength λ in size units is calculated from frequency f via $\lambda = 1/f$. Default: n/a
- Resolution (integer) Resolution in points per size unit. Default: n/a

- LayerDielReal (List of floats) Real parts of the dielectric functions of the individual layers. Has to have NumberOfLayers elements. Default: n/a
- LayerDielImag (List of floats) Imaginary parts of the dielectric functions of the individual layers. Has to have NumberOfLayers elements. Default: n/a
- Thicknesses (List of floats) Thicknesses of the individual layers. Has to have NumberOfLayers elements. Default: n/a
- HeightFiles (List of strings) Filenames of the topography files. If MultiProfile is true, this parameter need NumberOfLayer elements. Each topography file beyond the first must consist of differences from the previous layer. If MultiProfile is false, a single interface file is necessary. Default: n/a

- PMLThickness (float) Thickness of the perfectly matched layers in size units. Default: 1.0
- DefaultDielReal (float) Real part of the dielectric function of the ambient material. Default: 1.0 (vacuum)
- DefaultDielImag (float) Real part of the dielectric function of the ambient material. Default: 1.0 (vacuum)
- OutputEpsilon (boolean) Create output file containing the real part of the dielectric function for all points in the simulation. Default: false
- OutputEfield (boolean) Create output files containing the real and imaginary parts of all electric field components. Default: true
- OutputPoynting (boolean) Create output files containing all components of the Poynting vector. Default: false
- IncludeTip (boolean) Include an idealised SNOM tip in the simulation. Default: false
- TipPosition (List of floats) Position of the frontmost part of the aperture center of the SNOM tip. Only becessary if IncludeTip is true. Default: n/a
- FiberRadius (float) Radius of the aperture of the SNOM tip. Only necessary if IncludeTip is true. Default: n/a
- CoatingThickness (float) Thickness of the PEC around the tip. Only necessary if IncludeTip is true. Default: n/a
- OpeningAngle (float) Angle between x-axis and the side of the tip. Only necessary if IncludeTip is true. Default: n/a
- FiberEps (float) Real part of the dielectric function of the fiber inside the SNOM tip. Only necessary if IncludeTip is true. Default: n/a
- IlluminateTip (boolean) Switch for illumination through SNOM tip. Only necessary if IncludeTip is true. Default: n/a
- PeriodicBoundary (boolean) Switch for using periodic boundary conditions in y- and z-direction. Default: true
- TipAreaSource (boolean) Put a planar source at the beginning of the SNOM tip for illumination instead of a point source. Only necessary if IncludeTip and IlluminateTip are *both* true. Default: false
- BigDomain (boolean) Output all results as single slices. This is necessary if the size of the result arrays (e.g. espilon array, electric field array etc.) is larger than the memory available to a single CPU core. Default: false
- EpsAverage (boolean) Perform the internal epsilon averaging of MEEP. Default: false

B

CONVERGENCE TESTS AND CONSIDERATION OF DIFFERENT RESOLUTIONS

One important factor about FDTD simulations is the convergence of the simulation. This convergence mainly depends on two factors:

1. The resolution of the simulation, whith its discretisation in cubic cells. This resolution is of great importance especially for materials with high refractive indices and for short wavelengths, since the period of the electromagnetic wave in any given material and at any given period still has to be resolved in the simulation. Additionally, with layer thicknesses in the simulated devices sometimes being as thin as 40 nm, these layers have to be identifiable in the simulation as well.

2. The time after which the simulation is stopped. Since the simulations in this thesis use a continuous a light source, the simulation has to run until a steady state is reached.

Since computation time available for simulations was limited, this resolution limits had to be chosen in a way to minimise time consumption. This is especially true for the resolution, since an increase in resolution of a factor n increases simulation time by a factor of n^4, since not only the spatial, but also the temporal resolution increases. Another limiting factor is the number of points a single simulation can contain. Due to the fact that the number of cells in the simulation is stored in a 32-bit integer, the maximum number of points in a simulation is $2^{32} - 1 = 4294967295$. With a typical simulation domain of $10\mu m \times 10\mu m \times 8\mu m$ this limits the resolution to a maximum of 10 nm. Additionally, output time of the results increases roughly linear with the number of points.

Fortunately the number of timesteps before the simulation is stopped only increases the computation time linearly and has no influence on I/O time at all, so for this case, the convergence was tested for the largest possible simulation. The result of this simulation was then used for all other simulations as well, even if a shorter simulation time would have sufficed, because it would have been more time consuming to check this convergence for each system.

The resolution convergence was tested for a small part of an AFM scan using a 1 µm thick µc-Si:H layer on top of textured TCO. It is assumed that the simulation converges when the total intensity in the whole system stays constant. The simulation was performed for wavelengths between 350 nm and

1100 nm, with resolutions between 5 nm and 50 nm. The results of this convergence test is shown on Fig. B.1. In this graph, the resolution is shown in points per µm. As can be seen, a resolution of 20 nm is sufficient for wave-

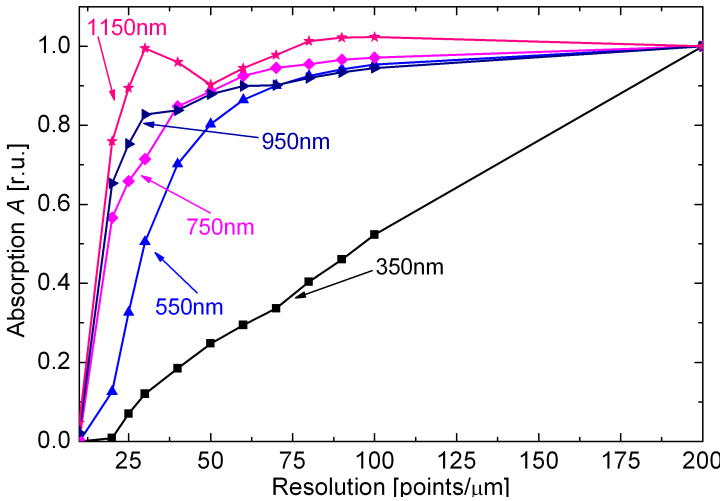

Figure B.1.: Tests of convergence for different resolutions at 350nm, 550nm, 750nm, 950nm and 1150nm. For wavelengths above 550nm, a resolution of 20nm (50 points per µm) is sufficient. For shorter wavelengths, 20nm are a very coarse resolution. However, tests have shown that relative trends are hardly influenced at all. This resolution was chosen due to the limited computation time available. For simulations requiring absolute values (the complete tandem device) or for the simulation of SNOM tips, a resolution of 10nm (100 points per µm) was used.

lengths above 600 nm. At smaller wavelengths, down to 450 nm, a resolution of 10 nm is necessary. At even shorter wavelengths, even 5 nm are too low a resolution. However, other investigations have shown that general trends and especially relative differences, e.q. for simple texture modifications (Sec. 7.2) are not as dependent on the simulation resolutionm with results showing an error of about 1%. Most simulations were performed to investigate relative enhancements, with only the investigation of the tandem device and the optimised textures from AID having any need for absolte values. Therefore, a resolution of 20 nm is sufficient for all other investigations. The same holds true for the investigation of light scattering, as in Chap. 6.

Additionally, the spectral region in which the texture shows the strongest influence in a typical thin-film device is above 600 nm, since light of shorter wavelengths is absorbed during its first pass through the absorber layer and has no need for light scattering. At larger wavelengths, where light scattering is important, a resolution of 20 nm is sufficient, as was shown above.

A special case is the investigation fo systems with an included SNOM tip. in this case, a resolution of 10 nm was used. The transmission characteristic

of the tip, with a transmission of 10^{-5}, as observed for a real-life tip, and the good agreement with the experiment in Chap. 8 are an excellent indication that this assumption is correct.

The investigation of the number of timesteps necessary for concergence was performed with a system of 10µm × 10µm × 8µm, with a field distribution written to disk every 10 time units or 1000 timesteps. For each output, the total intensity in the system was calculated. Convergence is assumed when the total intensity changes by less than one percent. The results are shown in Fig. B.2. In this case, 8000 timesteps at a resolution of 20nm or 80 units of time

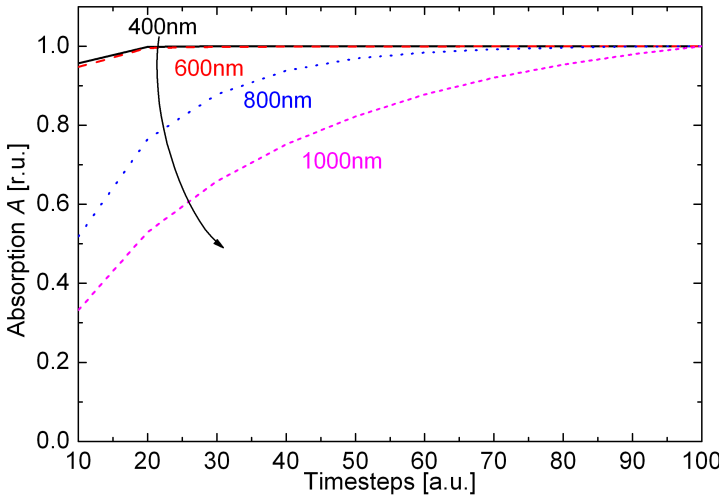

Figure B.2.: Tests of convergence for different stopping times of the simulation at 400nm, 600nm, 800nm and 1000nm using a µc-Si:H single junction cell. For all but the longest wavelengths (1000nm), stopping after 80 time units is sufficient. This was used as a baseline due to limited computing resources, since again relative differences were not influenced. For the absolute values of a tandem device, 100 time units were calculated, resulting in reliable values.

are sufficient to achieve convergence for all but the longest wavelengths. While intensity distributions imply a faster convergence, 8000 timesteps were used.

In conclusion, for relative comparisons and in a wavelength region where light scattering becomes important, a resolution of 20 nm is sufficient. At shorter wavelengths and for absolute values, as well as for simulations including a SNOM tip, a resolution of 10 nm was used. A steady state of the system is achieved after 8000 timesteps for most cases, after which the simulation is stopped.

BIBLIOGRAPHY

[1] F. C. M. van de Pol, F. R. Blom, and T. J. A. Popma, "R.f. planar magnetron sputtered zno films i: Structural properties," *Thin Solid Films*, vol. 204, pp. 349–364, 1991.

[2] M. Berginski, W. Hüpkes, J. amd Reetz, B. Rech, and M. Wuttig, "Recent development on surface-textured zno:al films prepared by sputtering for thin-film solar cell application," *Thin Solid Films*, vol. 516, pp. 5836–5841, 2008.

[3] M. Berginski, J. Hüpkes, M. Schulte, G. Schöpe, H. Stiebig, B. Rech, and M. Wuttig, "The effect of front zno:al surface texture and optical transparency on efficient ligt trapping in silicon thin-film solar cells," *J. Appl. Phys.*, vol. 101, p. 074903, 2007.

[4] M. Ermes, "Study of optical properties of individual layers and layer stacks as used in silicon based thin-film solar cells," Master's thesis, RWTH Aachen, 2010.

[5] www.finanzen.net, "Ölpreis in dollar (wti) chart - 3 jahre." Website, April 2013.

[6] G. Foley, "cells electrification in the developing world," *Energy Policy*, vol. 20, pp. 145–152, 1992.

[7] C. Rockstuhl, S. Fahr, K. Bittkau, T. Beckers, R. Carius, F.-J. Haug, K. Söderström, C. Ballif, and F. Lederer, "Comparison and optimization of randomly textured surfaces in thin-film solar cells," *Opt. Express*, vol. 18, pp. A335–A342, 2010.

[8] P. Wahl, "Belgium-california light machine (b-calm): An open-source gpu-based 3d-fdtd with mult-pole dispersion for plasmonics." Talk, September 2011. NUSOD Roma.

[9] C. Battaglia, J. Escarré, K. Söderström, L. Erni, L. Ding, G. Bugnon, A. Billet, M. Boccard, L. Barraud, S. De Wolf, F.-J. Haug, M. Despeisse, and C. Ballif, "Nanoimprint lithography for high-efficiency thin-film silicon solar cells," *Nano Letters*, vol. 11, pp. 661–665, 2010.

[10] A. F. Oskooi, D. Roundy, M. Ibanescu, P. Bermel, J. D. Joannopoulos, and S. G. Johnson, "Meep: A flexible free-software package for electromagnetic simulations by the fdtd method," *Comput. Phys. Commun.*, vol. 181, pp. 687–702, 2010.

[11] R. Windisch, B. Dutta, M. Kuijik, A. Knobloch, S. Meinlschmidt, S. Schoberth, P. Kiesel, G. Borghs, G. H. Dohler, and P. Heremans, "40% efficient thin-film surface-textured light-emitting diodes by optimization of natural lithography," *IEEE T. Electron. Dev.*, vol. 47, pp. 1492–1498, 2000.

[12] R. Windisch, C. Rooman, S. Meinlschmidt, P. Kiesel, D. Zipperer, G. H. Dohler, B. Dutta, M. Kuijik, G. Borghs, and P. Heremans, "Impact of texture-enhanced transmission on high-efficiency surface-textured light-emitting diodes," *Appl. Phys. Lett.*, vol. 79, pp. 2315–2317, 2001.

[13] A. Shah, *Thin-Film Silicon Solar Cells*. EPFL Press, 2010.

[14] C. M. Chapin, C. S. Fuller, and P. L. Pearson, "A new silicon p-n junction photocell for converting solar radiation into electric power," *J. Appl. Phys.*, vol. 25, pp. 676–677, 1954.

[15] D. Y. Goswami, "Solar thermal power technology: Present status and ideas for the future," *Energy Sources*, vol. 20, pp. 137–145, 1998.

[16] P. Würfel and U. Würfel, *Physics of Solar Cells*. Wiley-VCH, 2009.

[17] C. Authors and E. of the LB Volumes III/17A-22A-41A1b, "Gallium arsenide (gaas), refractive index, absorption index, absorption coefficients," *Landolt-Brnstein - Group III Condensed Matter, Numerical Data and Functional Relationships in Science and Technology*, vol. 41A1b, p. 1, 2002.

[18] C. Authors and E. of the LB Volumes III/17A-22A-41A1b, "Silicon (si), absorption index, absorption coefficient," *Landolt-Brnstein - Group III Condensed Matter, Numerical Data and Functional Relationships in Science and Technology*, vol. 41A1b, p. 1, 2002.

[19] "Astm g173 - 03(2012) standard tables for reference solar spectral irradiances: Direct normal and hemispherical on 37° tilted surface."

[20] C. M. Herzinger, B. Johs, W. A. McGahan, and J. A. Woollam, "Ellipsometric determination of optical constants for silicon and thermally grown silicon dioxide via multi-sample, multi-wavelength, multi-angle investigation," *J. Appl. Phys.*, vol. 83, pp. 3323–3336, 1998.

[21] G. D. Cody, C. R. Wronski, B. Abeles, R. B. Stephens, and B. Brooks, "Optical characterization of amorphous silicon hybride filme," *Solar Cells*, vol. 2, pp. 227–243, 1980.

[22] Wikipedia, "Direct and indirect band gaps – wikipedia, the free encyclopedia," 2013. [Online; accessed 21-July-2013].

[23] D.-H. Neuhaus and A. Münzer, "Industrial silicon wafer solar cells," *Advances in OptoElectronics*, vol. 2007, p. 24521, 2007.

[24] S. Klein, F. Finger, R. Carius, B. Rech, L. Houben, M. Luysberg, and M. Stutzmann, "High efficiency thin-film solar cells with intrinsic microcrystalline silicon prepared by hot wire cvd," *Material Research Society Symposium - Proceedings*, vol. 715, pp. 617–622, 2002.

[25] C. Das, A. Doumit, F. Finger, A. Gordijn, J. Huepkes, J. Kirchhoff, A. Lambertz, T. Melle, and W. Reetz, "Performance of superstrate multijunction amorphous silicon-based solar cells using optical layers for current management," *Sol. Energy Mater. Sol. Cells*, vol. 93, pp. 973–975, 2009.

[26] S. Ito, S. M. Zakeeruddin, P. Comte, P. Liska, D. Kuang, and M. Grätzel, "Bifacial dye-sensitized solar cells based on an ionic liquid electrolyte," *Nature Photonics*, vol. 2, pp. 693–698, 2008.

[27] M. A. Green, *Solar Cells: Operating Principles, Technology and System Applications*. Univ. New South Wales, 1998.

[28] H. W. Deckman, C. B. Roxlo, and E. Yablonovitch, "Maximum statistical increase of optical absorption in textured semiconductor films," *Opt. Lett.*, vol. 8, pp. 491–493, 1983.

[29] E. Yablonovitch and G. D. Cody, "Intensity enhancement in textured optical sheets for solar cells," *IEEE Trans. Electr. Dev.*, vol. 29, pp. 300–305, 1982.

[30] D. Dominé, P. Buehlman, J. Bailat, A. Billet, A. Feltrin, and C. Ballif, "Optical management in high-efficiency thin-film silicon micromorph solar cells with a silicon oxide based intermediate reflector," *phys. stat. sol. (RRL)*, vol. 2, pp. 163–165, 2008.

[31] O. Kluth, B. Rech, L. Houben, S. Wieder, G. Schöpe, C. Beneking, H. Wagner, A. Löffl, and H. W. Schock, "Texture etched zno:al coated glass substrates for silicon based thin film solar cells," *Thin Solid Films*, vol. 351, pp. 247–253, 1999.

[32] P. Bermel, C. Luo, L. C. Kimerling, and J. D. Joannopoulos, "Improving thin-film crystalline silicon solar cell efficiencies with photonic crystals," *Opt. Express*, vol. 15, pp. 16986–17000, 2007.

[33] U. W. Paetzold, E. Moulin, D. Michaelis, W. Böttler, C. Wächter, V. Hagemann, M. Meier, R. Carius, and U. Rau, "Plasmonic reflection grating back contacts for microcrystalline silicon solar cells," *Appl. Phys. Lett.*, vol. 99, p. 181105, 2011.

[34] K. Sato, Y. Gotoh, Y. Wakayama, Y. Hayashi, K. Adachi, and H. Nishimura, "Highly textured sno2:f tco films for a-si solar cells," *Reports Res. Asahi Glass Co.*, vol. 42, 1992.

[35] A. Shah, J. Meier, A. Buechel, U. Kroll, J. Steinhauser, F. Meillaud, H. Schade, and D. Dominé, "Towards very low-cost mass production

of thin-film silicon photovoltaic (pv) solar modules on glass," *Thin Solid Films*, vol. 502, pp. 292–299, 2006.

[36] K. Yamamoto, A. Nakajima, M. Yoshimi, T. Sawada, S. Fukuda, T. Suezaki, M. Ichikawa, Y. Koi, M. Goto, T. Meguro, T. Matsuda, M. Kondo, T. Sasaki, and Y. Tawada, "A high efficiency thin film silicon solar cell and module," *Solar Energy*, vol. 77, pp. 939–949, 2004.

[37] A. V. Shah, F. Sculati-Meillaud, Z. J. Berényi, O. M. Ghahfarokhi, and R. Kumar, "Diagnostics of thin-film silicon solar cells and solar panels/-modules with variable intensity measurements (vim)," *Sol. Energy Mater. Sol. Cells*, vol. 95, pp. 398–403, 2011.

[38] K. S. Yee, "Numerical solutions of initial boundary value problems involving maxwell's equation in isotropic media," *IEEE T. Antenn. Propag.*, vol. 14, pp. 302–307, 1966.

[39] A. Taflove and S. C. Hagness, *Computational Electrodynamics - The Finite-Difference Time-Domain Method*. Artech House, 2005.

[40] H. E. Bennett and J. O. Porteus, "Relation between surface roughness and specular reflectance at normal incidence," *J. Opt. Soc. Am.*, vol. 51, pp. 123–129, 1961.

[41] H. Davies *Proc. Inst. Electr. Eng.*, vol. 101, p. 209, 1954.

[42] S. Rice, "Reflection of electromagnetic waves from slightly rough surfaces," *Commun. Pure Appl. Math.*, vol. 4, pp. 351–378, 1951.

[43] D. Dominé, F.-J. Haug, C. Battaglia, and C. Ballif, "Modelling of light scattering from micro- and nanotextured surfaces," *J. Appl. Phys.*, vol. 107, p. 044504, 2010.

[44] W. Demtröder, *Experimentalphysik, Band 2: Elektrizität und Optik*. Springer-Lehrbuch, 2006.

[45] "Astm d1003 - 11e1 standard test method for haze and luminous transmittance of transparent plastics."

[46] G. Jost, T. Merdzhanove, T. Zimmermann, J. Kirchhoff, and J. Hüpkes, "Angular resolved scattering measurements as quality control tool for texture-etched zno:al front contacts," *Proceedings of the 27th EUPVSEC*, vol. 1, pp. 2543–2547, 2012.

[47] H. Stiebig, M. Schulte, C. Zahren, C. Haase, B. Rech, and P. Lechner, "Light trapping in thin-film solar cells by nano-textured interfaces," *Proceedings SPIE*, vol. 6197, pp. 619701–1, 2006.

[48] M. Schulte, *Streuverhalten von texturierten TCO-Substraten in Silizium-Dünnschichtsolarzellen*. Forschungszentrum Jülich GmbH, 2009.

[49] K. Bittkau, T. Beckers, S. Fahr, C. Rockstuhl, F. Lederer, and R. Carius, "Nanoscale investigation of light-trapping in a-si:h solar cell structures with randomly textured interfaces," *Phys. Status Solidi A*, vol. 205, pp. 2766–2776, 2008.

[50] C. Rockstuhl, F. Lederer, K. Bittkau, and R. Carius, "Light localization at randomly textured surfaces for solar-cell applications," *Appl. Phys. Lett.*, vol. 91, p. 171194, 2007.

[51] G. Binnig, C. F. Quate, and C. Gerber, "Atomic force microscope," *Phys. Rev. Lett.*, vol. 56, pp. 930–933, 1986.

[52] Surface Imaging Systems, Kaiserstr. 100, 52134 Herzogenrath, *Surface Imaging Systems - ULTRAObjective and SIScanPanel User Guide*, 1st ed., February 2008.

[53] G. Jost, *Analyse der Lichtstreuung zur Textur-Optimierung von Zinkoxid-Frontkontakten für Silizium-Dünnschichtsolarzellen*. PhD thesis, RWTH Aachen, 2012.

[54] G. Behme, A. Richter, M. Süpiz, and C. Lienau, "Vacuum near-field scanning optical microscope for variable cryogenic temperatures," *Rev. Sci. Instrum.*, vol. 68, pp. 3458–3463, 1997.

[55] W. Zinth and U. Zinth, *Optik, Lichstrahlen - Wellen - Photonen*. Oldenburg-Verlag, 2011.

[56] E. Moulin, U. W. Paetzold, K. Bittkau, J. Owen, J. Kirchhoff, A. Bauer, and R. Carius, "Investigation of the impact of the rear-dielectric/silver back reflector design on the optical performance of thin-film silicon solar cells by means of detached reflectors," *Prog. Photovolt.: Res. Appl.*, 2013.

[57] R. Dewan, J. I. Owen, D. Madzharov, V. Jovanov, J. Hüpkes, and D. Knipp, "Analyzing nanotextured transparent conductive ooxide for efficient light trapping in silicon thin film solar cells," *Appl. Phys. Lett.*, vol. 101, p. 103903, 2012.

[58] E. Moulin, U. W. Paetzold, K. Bittkau, M. Ermes, L. Ding, L. Fann, S. Nicolay, J. Kirchhoff, D. Weigand, A. Bauer, A. Lambertz, C. Ballif, and R. Carius, "Thin-film silicon solar cells applying opoptical decoupled back reflectors," *Material Science and Engineering: B*, vol. 178, pp. 645–650, 2013.

[59] M. Schulte, K. Bittkau, K. Jäger, M. Ermes, M. Zeman, and B. E. Pieters, "Angular resolved scattering by a nano-textured zno/silicon interface," *Appl. Phys. Lett.*, vol. 99, p. 111107, 2011.

[60] C. Haase and H. Stiebig, "Thin-film silicon solar eclls with efficient periodic light trapping texture," *Appl. Phys. Lett.*, vol. 91, p. 061116, 2007.

[61] D. Madzhanov, R. Dewan, and D. Knipp, "Influence of front and back grating on light trapping in microcrystalline thin-film silicon solar cells," *Opt. Express*, vol. 19, pp. A95–A107, 2011.

[62] U. Palanchoke, V. Jovanov, H. Kurz, R. Dewan, P. Magnus, H. Stiebig, and D. Knipp, "Influence of back contact roughness on light trapping and plasmonic losses of randomly textured amorphous silicon thin film solar cells," *Appl. Phys. Lett.*, vol. 102, p. 083501, 2013.

[63] V. Jovanov, X. Xu, S. Shrestha, M. Schulte, J. Hüpkes, M. Zeman, and D. Knipp, "Influence of interface morphologies on amorphous silicon thin film solar cells prepared on randomly textured substrates," *Sol. Energy Mater. Sol. Cells*, vol. 112, pp. 182–189, 2013.

[64] D. A. G. Bruggeman, "Berechnung verschiedener physikalischer konstanten von heterogenen substanzen," *Annalen der Physik*, vol. 24, p. 636, 1935.

[65] K. Bittkau, M. Ermes, and R. Carius, "Improving light-trapping efficiency of thin-film silicon solar cells by tuning light-scattering properties at front and back side.".

[66] X. Wang, Z. Fan, and T. Tang, "Simulation of topographic images and artifacts in illumination-mode scanning near-field optical microscopy," *J. Opt. Soc. Am.*, vol. 22, p. 2730, 2005.

[67] O. Fenwick, G. Latini, and F. Cacialli, "Modelling topographical artifacts in scanning near-field optical microscopy," *Synthetic Materials*, vol. 147, pp. 171–183, 2004.

[68] G. Kaupp, A. Hermann, and M. Haak, "Amicroscopy scanning near-field optical microscopy (snom) due to deficient tipe," *J. Phys. Org. Chem.*, vol. 12, pp. 797–807, 1999.

[69] J. Hinojosa, "Masterthesis title," Master's thesis, School Title, 2013.

[70] K. Bittkau and T. Beckers, "New applications of light scattering at rough interfaces of a-si:h/µc-si:h tandem solar cells," *Phys. Status Solidi A*, vol. 207, pp. 661–666, 2010.

[71] K. Bittkau, W. Böttler, M. Ermes, V. Smirnov, and F. Finger, "Light scattering at textured back contacts for n-i-p thin-film silicon solar cells," *J. Appl. Phys.*, vol. 111, p. 083101, 2012.

[72] M. Ermes, K. Bittkau, and R. Carius, "Comparison of light scattering in solar cells modeled by rigorous and scalar approach," *J. Appl. Phys.*, vol. 113, p. 073104, 2013.

[73] M. Ermes, K. Bittkau, and R. Carius, "Influence of texture modifications in silicon solar cells on absorption in the intrinsic layers," *Proceedings of SPIE - The International Society for Optical Engineering*, vol. 8438, p. 84380I, 2012.

[74] M. Ermes, W. Böttler, K. Bittkau, and V. Smirnov, "Influence of the back reflector texture on light scattering and performance of a nip-type microcrystalline silicon thin-film solar cell," *Proceedings of the 27th EUPVSEC*, vol. 3DV.2.18, pp. 2628–2631, 2012.

[75] J. Müller, B. Rech, J. Springer, and M. Vanecek, "Tco and light trapping in silicon thin film solar cells," *Solar Energy*, vol. 77, pp. 917–930, 2004.

[76] P. Obermeyer, C. Haase, and H. Stiebig, "Light trapping management by diffractive interlayer for thin-film silicon solar cells," *Appl. Phys. Lett.*, vol. 92, p. 181102, 2008.

[77] B. Rech and H. Wagner, "Potential of amorphous silicon for solar cells," *Appl. Phys., A*, vol. 69, pp. 155–167, 1999.

[78] Y. Safir, "Bifacial solar cell," *Renewable Energy*, vol. 13, pp. 146–147, 1998.

[79] H. Schade, P. Lechner, R. Geyer, H. Stiebig, B. Rech, and O. Kluth *Conference Record of the 31st IEEE - Photovoltaic Specialist Conference*, vol. 1, p. 1436, 2005.

List of Figures

Figure 1.1 3-year chart of the oil-price (April 30th, 2013). The erratic behaviour in oil price is clearly visible with price differences between 70 USD and 150USD. Taken from [5]. 3

Figure 2.1 Conversion of a photon into an electron-hole pair. If the energy of the photon is larger than the band gap, an electron-hole pair can be generated by exciting an electron from the valence into the conduction band. Any additional energy of the photon above the band gap is lost due to thermalisation. Drawings taken from [22]. 10

Figure 2.2 Absorption coefficient alpha of crystalline (black, solid), amorhpous (red, dashed) and microcrystalline (blue, dotted) silicon. While there are some differences in the absorption of the materials, the trends are very similar. the notable differences are the significantly higher absorption of crystalline silicon in the low energy regime and the higher absorption for a-Si:H in the intermediate wavelength range between 350 nm and 600 nm. 10

Figure 2.3 Absorption length and typical absorber layer thickness for crystalline (black, solid), amorphous (red, dashed) and microcrystalline (blue, dotted) silicon. Since the thickness of a typical wafer-cell is always larger than the absorption length, these cells already show good performance without textured interfaces. For the amorphous and microcrystalline cells, however, absorber layer thicknesses are smaller than the absorption length at wavelengths above 600 nm. Therefore, the light path inside the absorber layers has to be increased significantly, e.g. by light scattering at textured interfaces. 11

Figure 2.4 Sketch of light trapping approximated using geometrical optics. A textured interface can scatter light into different angles. For small angles (left side), the light can couple out of the cell in the same way it could with flat interfaces, however the light path is increased by the angle. In the best case (right side), the light is scattered into an angle above the angle total internal reflection and trapped inside the absorber layer until it is absorbed. 12

Figure 2.5 Sketch of an amorphous silicon single junction (a) and an amorphous/microcrystalline silicon tandem solar cell (b). The tandem cell consists of two individual cells with absorber layers exhibiting different band gaps. The top cell consists of an amorphous silicon pin stack and the bottom cell of a microcrystalline pin stack. Optionally, an intermediate reflector can be placed between the two to improve current matching. 14

Figure 3.1 Sketch of the Yee-cell, showing placement and direction of the electric and magnetic fields.[38] 16

Figure 3.2 Discretisation of a line of a topography scan by using rectangular blocks. The better the surface has to be approximated, the more blocks have to be defined. For an algorithm with an initialisation time depending on the number of blocks, a fine discretisation and/or a large domain lead to an extremely large number of blocks, increasing the initialisation time beyond the computation time, making the software unsuitable for use with HPC systems. 17

Figure 3.3 Flow chart and example pictures of our custom MEEP interface. After reading the config file, the topography is read. From this, a three-dimensional representation of the optical properties is created. After optionally including the SNOM tip, a light source is placed. In this example, it is a planar illumination through the substrate. Before actual simulation, the real part of the dielectric function can optionally be written to disk. After this, the actual simulation runs for a pre-determined number of time steps, after which the electric fields are written to disk. 19

Figure 3.4 Illustration of the phase model. At each point the height of the topography is used to calculate a phase shift based on the refractive index of the materials surrounding the interface.[43] 20

Figure 4.1 Visual representation of the calculation of an intensity distribution in a modelled 1 µm thick µc-Si:H cell according to Eq. (4.1). 22

Figure 4.2 Comparison of intensity distribution and absorptance for a single slice of a three-dimensional simulation at a wavelength of 800 nm. While intensity is visible in glass (bottom-most layer), front TCO (middle layer) and μc-Si:H (top-most layer), only the front TCO and μc-Si:H show absorption due to the assumption of $\epsilon_{i,glass} = 0$. 23

Figure 4.3 Sample EQE of a typical 1.5 μm thick textured μc-Si:H single junction cell. The cell absorbs light in a wavelength region between 300 nm and 1100 nm, with the highest EQE at around 500 nm. 24

Figure 4.4 Sketch of the algorithm used for calculating "absorption planes". The absorption for each point is integrated along the propagation direction of the light. As an example, this is shown for one slice of the three-dimensional simulation (a), with the integrated absorption at each point shown in plot (b). Doing this for all points of a layer results in a distribution as shown in (c). 25

Figure 4.5 Example of an absorption plane (b) showing the crater rims of the original texture (a). In this example, a 300 nm thin a-Si:H layer was simulated on top of the texture. Due to the small thickness, the correlation between topography and absorption plane is still clearly visible. Additionally, at the simulated wavelength (450 nm), the absorption of the a-Si:H is high enough so that the light is not reflected again at the back side, so no influence of the back side texture is visible. 26

Figure 4.6 Example of an absorption plane (b) showing little resemblance to the original texture (a). In this example, a 1 μm thick μc-Si:H layer was simulated on top of the texture at a wavelength of 800 nm. Due to the small absorptance, the light passes through the μc-Si:H layer multiple times, with the light being scattered each time it reaches one of the interfaces. Additionally, the large thickness reduces correlation between the layer boundaries due to scattering into large angles, so effects of surface features can influence the absorption at positions beyond the vicinity of the features. While the features in absorption are harder to correlate to a certain surface feature, this can lead to better understanding of the absorption in the layer. 26

Figure 4.7 Example of a calculated AID, which is equivalent to angular resolved scattering measurements (Sec. 5.2) for a textured ZnO:Al layer at an ZnO:Al/air interface at a wavelength of 700 nm. This is an example calculated from PM, using a wet-etched ZnO:Al layer as input. However, since the AID is calculated from a FFT, its resolution is limited by the area over which the FFT is performed and the refractive index of the material into which the light is scattered. The low angular resolution is an effect of the comparably small sample area ($10\mu m \times 10\mu m$) and the small refractive index of the material ($n \approx 1.7$). 28

Figure 5.1 Working principle of the AFM: A very fine tip (typical tip radius: 10 nm), which is mounted on a cantilever, is either pulled over a surface in contact mode or kept at a certain distance, both using a feedback system. The cantilever is illuminated by a laser, and the reflection measured with a spatially resolved detector. Due to the flexing of the cantilever and the resulting shift in the position of the reflection on the detector, the position of the tip can be calculated.[52] 30

Figure 5.2 Working principle of the ARS measurement: A sample is illuminated using a laser, and a detector moves around the sample at constant distance, measuring light intensities at different angles. These result in an angular distribution of measured intensities, both in transmission and reflection. Illustration taken from [53]. 31

Figure 5.3 Sketch of a typical SNOM system. The sample can be illuminated with lasers through the optical window and lens. The tip can be positioned using both motors for coarse and piezo elements for fine movement. The tip is kept at a constant distance above the surface using a feedback system based on a ceramic tuning fork. Illustration taken from [54]. 32

Figure 5.4 SEM image of a SNOM tip. The shape is nearly conical, which will be used later on (Chap. 8). This example also shows a rather large tip with a thick metal coating and a total diameter at the front of about 1 µm. 33

Figure 6.1 Topographies of small feature sample (a) with heights up to 600 nm, stretched sample (b, heights up to 3100 nm), and large feature air and µc-Si:H sample (c) with heights up to 890 nm as measured by AFM. (d) shows the surface of the LPCVD-grown ZnO:B layer (heights up to 540 nm). 38

Figure 6.2 Sketch of the system used in FDTD simulations. The dashed and dotted lines show the planes used for calculation of the AID (dashed: PM, dotted: FDTD) and light scattered into evanescent modes (dashed line). 39
Figure 6.3 Topography, PM and FDTD results for the large feature air sample: Original topography (a), real part of the pupil function as obtained by PM (b), real part of the electric field in polarisation direction obtained by FDTD at the highest peak of the topography (c) and 3.5 µm above the surface (d). All calculations were performed at a wavelength of 600 nm. 40
Figure 6.4 Spectral haze of the small feature (a) and large feature air (b) sample calculated from PM and FDTD. Both models show an excellent agreement. 41
Figure 6.5 Spectral haze of the large feature µc-Si:H (a) and stretched (b) sample. Both models show a very good agreement, but with visible differences between 700 nm and 1250 nm (a) and between 850 nm and 1200 nm (b). 42
Figure 6.6 Spectral haze of the LPCVD sample. Agreement between both models is again very good, with similar differences between the models as for the stretched sample, but shifted to shorter (400 nm to 800 nm) wavelengths. 43
Figure 6.7 Angular intensity distribution of the small feature sample (a) and large feature air sample (b), calculated using PM and FDTD. AID is shown for 600 nm and 1000 nm. All curves are normalised to their respective maxima. 44
Figure 6.8 Angular intensity distribution of large feature µc-Si:H sample (a) and the stretched sample (b). AID is shown for 600 nm and 1000 nm. Both curves are normalised to their respective maxima. 45
Figure 6.9 AID of the LPCVD sample. The curves at wavelengths of 600 nm and 1000 nm are normalized to the values at 23° and 40.5°, respectively, with the PM showing a lower peak at 0°. 46
Figure 6.10 Light scattered into evanescent modes for the small feature sample (a) and large feature air sample (b). The dashed and dotted vertical lines represent the beginning of the evanescent modes for 1000 nm and 600 nm, respectively. 47
Figure 6.11 Light intensity scattered into evanescent modes for the large feature µc-Si:H sample (a) and stretched sample (b). The dashed and dotted lines indicate the beginning of the evanescent modes for 1000 nm and 600 nm, respectively. 48

Figure 6.12 Light intensity scattered into evanescent modes for the LPCVD sample. The dashed and dotted vertical lines indicate the beginning of the evanescent modes for 1000 nm and 600 nm, respectively. 49

Figure 6.13 Textures of the different substrates used for sample preparation. A 6 s etched ZnO:Al (a), a 40 s etched ZnO:Al (b) and a commercial Asahi-U type substrate (c). The 6 s etched ZnO:Al shows isolated craters of sizes between 50 nm and 500 nm, with only a small rms roughness. The 40 s etched ZnO:Al substrate exhibits many creates, most of them adjacent to each other, with sizes between 200 nm and up to 2000 nm. The peak-to-peak roughness is 842 nm and the rms roughness 140 nm. The Asahi-U type structure exhibits many pyramid-like structures, with a maximum height of 380 nm and a rms roughness of 39 nm. 50

Figure 6.14 Textures of μc-Si:H cells deposited on the different substrates with a thickness of 2300 nm. For all three depositions, the growth of the crystallites can be seen. For the 6 s etched ZnO:Al (a), the rms roughness is reduced, while the surface structure shows the small crystallites and retaining some of the larger craters. For the 40 s etched ZnO:Al (b), The large craters from the previous AFM scan (Fig. 6.13(b)) are still visible while much of the structure has been changed by the μc-Si:H growth. The same is true for the Asahi-U structure (c), where distinct features, as the "bulges" at the left and right side of the scan, are still visible. However, the structure shows more similarities with the original AFM scan (Fig. 6.13(c)). 50

Figure 6.15 Samples after polishing. The polishing of the 6 s etched ZnO:Al substrate (a) shows the best results with a remaining rms roughness of 8 nm and a peak-to-peak height of 143 nm. The 40 s etched ZnO:Al sample (b) still shows characteristic features of the original surface, which indicates a non-optimal polishing. The peak-to-peak height was reduced to 536 nm and the rms roughness was reduced to 60 nm. The Asahi-U type sample (c) exhibits a smoother surface with a rms roughness of only 25 nm, while peak-to-peak height remained at a relatively high 311 nm. This can be attributed to a small number of high features, possibly remains of the polishing or AFM artefacts. 51

Figure 6.16 Sketch of the model used for FDTD simulation. (a) shows the sample after polishing, with a reduced average thickness of the absorber layer and a flat front contact. For the real device, this is only a rough approximation, as indicated by the AFM scans after polishing (Fig. 6.15). The unpolished sample is sketched in (b). The interfaces assumed at the back side are shown in Fig. 6.13 and the front side texture assumed for the non-polished samples in Fig. 6.14. 52

Figure 6.17 AID in reflection of the unpolished samples deposited on 6 s etched ZnO:Al (a), 40 s etched ZnO:Al (b) and Asahi-U (c) at a wavelength of 532 nm. FDTD simulations consisted of measured back side texture (Fig. 6.14) and front side texture (Fig. 6.13). For PM calculations, only the front side texture is considered. Agreement between experiment and FDTD simulation is good for all samples, except for the large angle portion of the 40 s etched ZnO:Al substrate. Agreement with PM is also very good. 53

Figure 6.18 AID in reflection of the polished samples deposited on 6 s etched ZnO:Al (a), 40 s etched ZnO:Al (b) and Asahi-U (c). Agreement between experiment and FDTD simulations is good for the 6 s etched ZnO:Al substrate, but much worse for the other two samples. while agreement with PM is good for all samples. With the only difference lying in the front side texture, this is the dominating influence on AID for short wavelengths. 54

Figure 6.19 AID for a wavelength of 800 nm as obtained by FDTD and PM for the 6 s etched ZnO:Al (a), 40 s etched ZnO:Al (b) and Asahi-U. For all samples, large angle scattering is apparently dominated by the back side texture, while small angle scattering is dominated by the front side texture. 55

Figure 6.20 Measured EQE of the unpolished (black) and polished (red) samples on 6 s etched ZnO:Al (a), 40 s etched ZnO:Al (b) and Asahi-U. For all samples, the EQE is strongly decreased by polishing for the short wavelength region. However, this effect is reduced at long wavelengths, indicating the influence of the front sided texture on cell performance in the short wavelength region. Additionally, the polishing has induced defects into the front contact, which also contribute to the reduced performance. For long wavelengths, however, the back side texture has a far stronger influence. 56

Figure 6.21 Relative increase/decrease in EQE (experiment, black) and absorptance (simulation, blue) of the polished sample compared to the unpolished over wavelength for 6 s etched ZnO:Al (a), 40 s etched ZnO:Al (b) and Asahi-U. In the short wavelength region, simulation and experiment only agree for the Asahi-U cell, while for both ZnO:Al cells, agreement only gets better at longer wavelengths. This is attributed to the neglecting of electrical influences in the simulation and non-perfect polishing. At long wavelengths, agreement becomes better, indicating the dominance of the back side texture for cell performance at long wavelengths. 57

Figure 7.1 Topography before (a) and after (b) deposition of a 500 nm thick a-Si:H layer. The a-Si:H-deposition rounds of the sharp crater rims. 59

Figure 7.2 Topography before (a) and after (b) deposition of a 1000 nm thick μc-Si:H layer. The μc-Si:H-deposition adds small protrusions to the whole surface due to the growth of Si crystallites. 60

Figure 7.3 All possible permutations for the measured textures before and after deposition: Reference structure with front TCO texture at both interfaces (a), the textures positioned as in the real-life device (b), the post-deposition texture at both interfaces (c) and the "inverse real-life structure" (d). 61

Figure 7.4 Spectrally resolved increase/decrease in absorptance of a 500 nm a-Si:H cell for different interface texture combinations. The a-Si:H texture shows detrimental influence on light incoupling in the short wavelength region (a-Si:H/a-Si:H and a-Si:H/TCO), while the thickness variation introduced by silicon growth has a positive influence on absorptance in the long wavelength region (TCO/a-Si:H and a-Si:H/TCO). 62

Figure 7.5 Spectrally resolved increase/decrease in absorptance of a 1000 nm μc-Si:H cell for different interface texture combinations. The μc-Si:H texture shows better performance as both the front side texture in the short wavelength region (μc-Si:H/TCO and μc-Si:H/μc-Si:H) and as the back side texture in the long wavelength region (TCO/μc-Si:H and μc-Si:H/μc-Si:H). 63

Figure 7.6 AID of the μc-Si:H-texture in transmission (a) and reflection (b) at a wavelength of 700 nm at a TCO/μc-Si:H interface. Most of the light is scattered in angles smaller than 15° in transmission. In reflection, most of the light is scattered into large angles beyond the angle of total internal reflection. 64

Figure 7.7 10µm × 10µm AFM scan of original texture; a standard wet-etched ZnO:Al layer was used as basis for all texture modifications investigated here. The typical, random crater-like structures of various sizes are clearly visible 65

Figure 7.8 Model of the simulated system: The light enters the system through a glass half space. This "substrate" is covered with a rough ZnO:Al layer, the interface roughness obtained from the AFM scan (Fig. 7.7). On top of this TCO, a 300 nm thin a-Si:H layer is assumed with a conformal texture at the back side. The back contact consists of either a PEC (for the single junction model) or µc-Si:H to model the top cell in a tandem device. 66

Figure 7.9 Sketch of the modifications performed on the original texture (Fig. 7.7). Depending on the type of stretching (lateral: bottom, height: top), either the AFM scan was laterally modified to obtain the same resolution (f_{lat}) or the height was multiplied with a given factor (f_h). 66

Figure 7.10 Spectrally resolved relative absorptance difference for lateral stretching for multiple values of f_{lat}. The best enhancement in this case is shown as dashed line, which can be observed for $f_{lat} = 0.6$. 68

Figure 7.11 AID of a texture with steep flanks ($f_h = 3.0$) (a) and shallow flanks ($f_h = 0.5$) (b). As can be seen, much of the light is scattered into large angles for a texture with steep flanks, with a maxima at about 35° and 48°. For shallow flanks, most of the light is not scattered at all, with the rest scattered only into small angles. 69

Figure 7.12 Absorption planes (as described in Sec. 4.4) of the best lateral stretching ($f_{lat} = 0.6$) for wavelengths of 450 nm (a), 550 nm (b) and 650 nm (c). An integrated absorption plane over all wavelengths weighted with an AM1.5g spectrum is shown in (d). The white squares indicate areas with the highest integrated absorptance of all areas of that size. 70

Figure 7.13 Spectrally resolved absorptance enhancement for height stretching for multiple values of f_h. The best enhancement is shown as dashed line, with a factor of $f_h = 2.0$. 71

Figure 7.14 Absorption planes (as described in Sec. 4.4) of the best height stretching ($f_h = 2.0$) for wavelengths of 450 nm (a), 550 nm (b) and 650 nm (c). An integrated absorption plane over all wavelengths weighted with an AM1.5g spectrum is shown in (d). The white squares indicate areas with the highest integrated absorptance of all areas of that size. 72

Figure 7.15 Spectrally resolved absorptance increase/decrease for the simplified tandem device for multiple values of f_{lat}. While in the short wavelength region is similar to that obtained with a PEC back side (Fig. 7.10), those modifications showing the highest increase in the short wavelength region (and overall) show a strong decline in absorptance in the long wavelength region. Due to the identical parasitic absorptance in the front TCO layer, this must be transmitted into the μc-Si:H back side. 73

Figure 7.16 Absorption planes (s. Sec. 4.4) of the best ($f_{lat} = 0.6$) lateral stretching for 450 nm (a), 550 nm (b) and 650 nm (c). Weighted with an AM1.5g spectrum, the results are displayed in (d). Unlike the PEC-covered a-Si:H layer, areas of highest absorptance are much more size-dependant, especially for the overall absorptance (d). This is caused by the low reflection at the a-Si:H/μc-Si:H interface. 75

Figure 7.17 Spectrally resolved absorptance increase/decrease for the simplified tandem device for multiple values of f_h. While in the short wavelength region is similar to that obtained with a PEC back side (Fig. 7.14), those modifications showing the highest increase in the short wavelength region (and overall) show a strong decline in absorptance in the long wavelength region. Due to the identical parasitic absorptance in the front TCO layer, this must be transmitted into the μc-Si:H back side. Again, when compared to the lateral stretching (Fig. 7.15), there is a decline in absorptance in the very short wavelength region due to higher effective thickness of the TCO layer and therefore more parasitic absorptance. 76

Figure 7.18 Absorption planes (s. Sec. 4.4) of the best ($f_h = 1.4$) lateral stretching for 450 nm (a), 550 nm (b) and 650 nm (c). Weighted with an AM1.5g spectrum, the results are displayed in (d). In this case, areas of highest absorptance are very similar to that of the single junction device (Fig. 7.14). 77

Figure 7.19 Sketch of the topography optimisation by using FFT and PM. (a): The original texture that should be optimised. (b): The real part of the phase as obtained by PM. (c): The resulting FFT and AID. (d): FFT and AID after applying the high-pass filter. (e): The real part of the phase image obtained by iFFT. (f) The final result: An optimised texture calculated from the phase image. The structure is still very similar to the original texture, with smaller additional features inside the craters and the craters generally deeper and steeper. The additional features are rooted in small features which are small but present in the original texture. Also, some FFT artefacts can be seen, but these are not strongly pronounced. 78

Figure 7.20 Original textures used in the optimisation. Two etched ZnO:Al surfaces of type 2 (a) and type 3 (b) as described in [31]. 79

Figure 7.21 Textures optimised for different limits of the high-pass filter. (a) shows the textures optimised for light scattering in transmission, (b) the ones optimised in reflection. The trends of the differences to the original texture are the same as seen for the example in Fig. 7.19. It is noteworthy that the optimisation in reflection leads to a smaller difference through the optimisation, mainly due to the fact that the original texture is already an excellent scatterer in reflection. 79

Figure 7.22 Portion of light scattered into angles larger than the angle of total internal reflection at a TCO/µc-Si:H (T) or µc-Si:H/TCO (R) interface as a function of the width of the high-pass filter for the type 2 (a, 800_40s) and type 3 (b, ipv_100-119_45s) textures. The tuning of light scattering in reflection only leads to a slight improvement of light scattering in reflection and to even less increase in transmission for both textures. Tuning the transmission, however, has a serious impact on the performance in transmission while also slightly improving light scattering in reflection. This effect is more pronounced for the originally worse type 3 texture. 81

Figure 7.23 Improvement in EQE as obtained by FDTD (dashed) and an empirical formula using PM results (solid) for the type 2 (a, 800_40s) and type 3 (b, ipv_100-119_45s) textures at a wavelength of 700 nm. The combination of light scattering in transmission and reflection allow for a good prediction of the FDTD results, with deviations originating from the thin layer thickness of the absorber layer and the multiples reflections at both interfaces of the absorber layer. 82

Figure 7.24 EQE before (solid) and after (dashed) optimisation for both textures as obtained by FDTD (a) and relative enhancement (b) for both type 2 (blue) and type 3 (red) textures. The relative enhancement is very similar for both structures, since the optimisation was performed identically for both. And in both cases, the improvement, especially in the long wavelength region, is significant. 83

Figure 7.25 Comparison of the layer stacks as assumed in simulation (a) and present in a real-life device (b). The simulation omits the doped layers of the p-i-n structures, since they are optically very similar to the intrinsic layer and are not recognisable in the output from the simulation software. Additionally, neither the simulation nor the real device had any intermediate reflector between top and bottom cell. 84

Figure 7.26 Comparison of simulated EQE (solid line) to two measured EQEs (dashed and dotted line), as well as measured reflection data, The simulation modelled the device represented by the dashed line. Also, the reflection measurement was performed on that cell. In the short wavelength region (350 nm to 550 nm), there is an wavelength-dependent difference between experiment and simulation, which can be explained by the low resolution of 10 nm. In the middle wavelength region (600 nm to 800 nm), the agreement with the a-Si:H top cell is very good. However, the bottom cell shows strong differences in this wavelength region as well as in the long wavelength region between 850 nm and 1100 nm. The simulation significantly underestimates the EQE of the μc-Si:H bottom cell. This is caused by three effects: The real-life device is likely to have a thicker bottom cell, the optical data used in the simulation is not of the exact same layer, but taken from a different layer deposited on glass in a different deposition system, and the air/glass interface at the front of the cell is neglected in the simulation, leading to less light trapping in the long wavelength region, where the measurement shows high reflection from the device. 85

Figure 8.1 Examples of a topography measured by AFM (a) and SNOM (b), as well as the intensity measured simultaneously by SNOM (c). The topography as measured by SNOM is blurred compared to the (sharp tip) AFM measurement. In the intensity measurement, the crater rims show a much higher intensity than the crater centres. 88

Figure 8.2 Sketch of the algorithm used to calculate probe positions. Both the surface texture and the probe geometry, e.g. an idealised, calculated geometry (a), are stored in a three-dimensional array. At each point of the texture, the center of the tip is assumed to be 20 nm above the surface. Next, a part of the surface has to be defined in a way that adding the tip array would result in a distance of 20 nm between the center of the probe and the surface (b). Calculating the intersection of the arrays, marked with a red circle in (b), it is clear that the real position must be above this point, since anything else would result in a tip crash in the experiment. From now on, the tip is moved upward pixel by pixel, until there is no longer any intersection, as shown in (c). This point marks the offset between probe and surface. This procedure is repeated for every point of the texture. From the resulting two-dimensional array of offsets, the intensity at these offsets can be extracted from simulation data. These sketches also resemble the discretisation or pixels as used for the calculations. 89

Figure 8.3 Textures investigated with the tip algorithm. 50s etched ZnO:Al, shown in (a) and AN10 substrate, shown in (b). The former shows the known crater-like structures, while the latter exhibits pyramid-like structures, similar to Asahi-U. 90

Figure 8.4 Cross-sections of the tip geometries: The idealised shape of the probe is assumed to be a truncated cone. (a) shows an approximation of a good SNOM probe, with an aperture radius of 40 nm, a coating thickness of 80 nm and an angle of 15°. (b) shows a presumably bad tip, with an aperture radius of 80 nm, a coating thickness of 120 nm and an angle of 25°. 91

Figure 8.5 Topographies, surface angle distribution and offsets obtained by the algorithm for the ZnO:Al sample. (a) shows the topography as obtained by AFM measurement, (b) is the topography signal of the SNOM. The offset between AFM and SNOM can be explained by a non-perfect z-calibration of the SNOM. (c) and (d) show the topography of the surface after application of the algorithm for the good and bad probe, respectively. It is visible that the good probe shows a slightly better resemblance to the SNOM than the bad probe geometry. However, an actual tip geometry is likely to be somewhere in between those two. (e) shows the surface angle distribution obtained from the AFM scan. (f) shows the offsets obtained for the good probe geometry. These offsets correlate well with the surface angle distribution.
92

Figure 8.6 Topographies, surface angle distribution and offset obtained by the algorithm for the AN10 sample. (a) shows the topography as obtained by AFM, (b) is the topography signal of the SNOM. (c) and (d) show the topography of the surface after the application of the algorithm for the good and bad probe geometry, respectively. It is visible that the general feature size is better represented by the bad tip. The strong discretisation results from the FDTD resolution of 20 nm. (e) shows the surface angle distribution obtained from the AFM, (f) shows the offsets obtained for the bad probe geometry. Again, the features are similar to those of the surface angle distribution. However, small features in the angle distribution are not visible due to the large dimensions of the probe.
93

Figure 8.7 Light intensity distribution from SNOM measurements and FDTD simulation of the ZnO:Al sample. (a) shows the intensity distribution as measured by SNOM. A high light intensity is observed at nearly all crater rims. (b) shows the intensity distribution from FDTD simulation at a constant distance of 20 nm above the sample surface. There are many interferences visible, as well as features that relate to near-field effects. In contrast to the measurement, the crater rims do not exhibit a much higher intensity than the crater centres. (c) and (d) show the light intensity distributions obtained when taking into account the offsets obtained from the algorithm (Fig. 8.5(f) for the good geometry), respectively. The agreement with the measurement is much better, especially for the good probe geometry, as can be seen for the features in the top right. The crater rims are better visible in the measurement as well as for the good probe geometry. 95

Figure 8.8 Light intensity distributions from SNOM measurement and FDTD simulation of the AN10 sample. (a) shows the intensity distribution as measured by SNOM. The shape of the features in this distribution is similar to those seen in the topography measurement (Fig. 8.6(a)). (b) shows the intensity distribution from FDTD simulation at a constant distance of 20 nm above the surface. There are many smaller features visible, as well as features that relate to near-field effects. (c) and (d) show the light intensity distribution obtained when taking into account the offsets obtained by the algorithm (Fig. 8.6(f) for the bad geometry). The agreement with the SNOM measurement is better for both geometries. 96

Figure 8.9 Intensity vs. reciprocal lattice constant obtained by FFT of the intensity distribution of the ZnO:Al(a) and AN10(b) sample. The dotted line indicates the transition from propagating to evanescent intensity. For the ZnO:Al sample, the trends in the propagating part are very similar for the measurements as well as all intensity distributions obtained by FDTD. In the evanescent region, however, the inclusion of the tip significantly improves agreement with the measurement, while the intensity directly above the surface indicates a strong over-estimation of the evanescent intensity. For the AN10 sample (b), the overall result is similar. However, due to the small feature size and the comparatively large tip, the FDTD results directly above the surface lead to a shift of the propagating peak to higher reciprocal lattice constant. This can be explained by the fact that the sharp features are blurred by the large tip and lead to smaller angles when analysed by FFT. Additionally, the measurement only drops to 10^{-1} in the evanescent region due to high noise. 97

Figure 8.10 Sketch of the crater used for investigating the influence of the SNOM tip; (a) shows a top-down view of the crater. It is assumed to be rotationally symmetric, with an inner (crater centre to rim) radius of 500 nm. (b) shows a cross-section of the crater. The inner and outer angles of the crater were set to 65° and 55°, respectively. 98

Figure 8.11 Intensity distributions for an idealised ZnO:Al crater, without a SNOM tip (a), with a SNOM tip above the centre (b), and with the tip placed above the crater rim (c). The presence of the tip changes the light propagation in its close vicinity. For example, the flare above the crater centre is suppressed in (b) and diverted in (c). However, the intensity distribution inside the layer and further away from the tip is hardly affected at all. However, the "flare" visible above the centre of the crater in the undisturbed system is modified by the tip; in (b), it is not visible at all due to the tip being in its place, while in (c), the flare is diverted due to the metal coating of the tip. 100

Figure 8.12 Intensities at the front (solid) and back (dotted) of the SNOM tip for each position (a) and shape of the crater as approximated in FDTD simulation (b). The good agreement indicates a good light incoupling into the tip. 101

Figure 8.13 Intensity directly above the surface (dotted) and inside the tip (solid) for simulations of the disturbed system (a) and shape of the crater as approximated in FDTD simulation (b). These curves are nearly identical. This indicated that the SNOM actually measures the intensity directly above the surface for the disturbed system. This, however, does not give any clues as to the results of the undisturbed system, which is shown in Fig. 8.14. 102

Figure 8.14 Comparison between the measured intensity (solid), the intensity of the undisturbed system at the actual tip positions (dotted) and directly above the surface in the undisturbed system (dashed) (a) and shape of the crater as approximated in FDTD simulation (b). While there are similarities between the intensity at the tip positions and the intensity above the surface, the small features directly above the surface are not reproduced, since they result from near-field effects. Comparing the intensity at the tip positions with the actual (simulated) measurement, the shape is very similar, with a slight shift. This shift can be explained due to the aperture radius of 80 nm. Due to this, light can couple into the fibre approximately 80 nm before the centre of the aperture is above the point of interest, correlating very well with this shift. 103

Figure B.1 Tests of convergence for different resolutions at 350nm, 550nm, 750nm, 950nm and 1150nm. For wavelengths above 550nm, a resolution of 20nm (50 points per μm) is sufficient. For shorter wavelengths, 20nm are a very coarse resolution. However, tests have shown that relative trends are hardly influenced at all. This resolution was chosen due to the limited computation time available. For simulations requiring absolute values (the complete tandem device) or for the simulation of SNOM tips, a resolution of 10nm (100 points per μm) was used. 122

Figure B.2 Tests of convergence for different stopping times of the simulation at 400nm, 600nm, 800nm and 1000nm using a μc-Si:H single junction cell. For all but the longest wavelengths (1000nm), stopping after 80 time units is sufficient. This was used as a baseline due to limited computing resources, since again relative differences were not influenced. For the absolute values of a tandem device, 100 time units were calculated, resulting in reliable values. 123

NOMENCLATURE

a-Si:H	hydrogenated amorphous silicon
μc-Si:H	hydrogenated microcrystalline silicon
AFM	atomic force microscope
AID	angular intensity distribution
ARS	angular resolved scattering
BST	back side texture
CPU	central processing unit or processor
EQE	external quantum efficiency
FDTD	Finite-Difference Time-Domain
FFT	fast Fourier transform
FST	front side texture
GPU	graphics processing units
HPC	high-performance cluster
LED	light emitting diode
PEC	perfect electric conductor
PM	phase model
PML	perfectly matched layer
SEM	scanning electron micrograph
Si	silicon
SNOM	scanning near-field optical microscope
TCO	transparent conductive oxide
ZnO:Al	aluminium-doped zinc oxide
ZnO:B	boron-doped zinc-oxide

LIST OF PUBLICATIONS

In the course of this thesis, the following publications were made:

- Schulte, M., Bittkau, K., Jäger, K., Ermes, M., Zeman, M., Pieters, B.E., "Angular resolved scattering by a nano-textured ZnO/silicon interface", Appl. Phys. Lett., Vol. **99** (11), 111107, 2011.
- Bittkau, K., Böttler, W., Ermes, M., Smirnov, V., Finger, F., "Light Scattering at textured back contacts for n-i-p thin-film silicon dolar cells", J. Appl. Phys **111** (8), 083101, 2012.
- Ermes, M., Bittkau, K., Carius, R., "Influence of texture modifications in silicon solar cells on absorption in the intrinsic layers", Proc. of SPIE **8438**, 84380I, 2012.
- Ermes, M., Böttler, W., Bittkau, K., Smirnov, V., "Influence of the Back Reflector Texture on Light Scattering and Performance of a nip-Type Microcrystalline Silicon Thin-Film Solar Cell", Proc. of the 27th EUPVSEC, pp. 2628-2631, 2012.
- Ermes, M., Bittkau, K., Carius, R., "Comparison of light scattering in solar cells modelled by rigorous and scalar approach", J. Appl. Phys. **113** (7), 073104, 2012.
- Moulin, E., Paetzold, U. W., Bittkau, K., Ermes, M., Ding, L., Fanni, L., Nicolay, S., Kirchhoff, J., Weigand, D., Bauer, A., Lambertz, A., Ballif, C., Carius, R., "Thin-film silicon solar cells applying optically decoupled back reflectors", Mat. Sci. Eng. B-solid **178** (9), 645-650, 2013.
- Ermes, M., Lehnen, S., Bittkau, K., Carius, R., "Reconstruction of SNOM near-field images from rigorous optical simulations by including topography artifacts", Proc. SPIE Opt. Metr. **8789**, 87890I, 2012.

Oral and visual presentations:

- Ermes, M., Bittkau, K., Carius, R., "Influence of texture modifications in silicon solar cells on absorption in the intrinsic layers", Oral presentation, SPIE Photonics Europe 2012.
- Ermes, M., Böttler, W., Bittkau, K., Smirnov, V., "Influence of the Back Reflector Texture on Light Scattering and Performance of a nip-Type Microcrystalline Silicon Thin-Film Solar Cell", Poster presentation at the 27th EUPVSEC, 2012.
- Ermes, M., Lehnen, S., Bittkau, K., Carius, R., "Reconstruction of SNOM near-field images from rigorous optical simulations by including topography artifacts", Oral presentation, SPIE Optical Metrology 2013.

ACKNOWLEDGEMENT

I am very grateful for all the support I was given in the course of this thesis and I would like to thank all colleagues and other people involved in the research presented in this thesis.

I would like to thank Prof. U. Rau for supervising this work and his support during the past three years. His suggestions for this work are deeply appreciated.

Also, I would like to thank Prof. Dr. R. Carius for supporting this work. His open-mindedness to some of my less conventional ideas, especially for the investigations of the SNOM-tip have been a great help as well as his honest and well-founded criticism to the less successful investigations which did not make it into this thesis.

I also thank Dr. K. Bittkau for direct supervision of this work and his cooperation and input on my work presented in this thesis. His knowledge of programming has proven invaluable in the course of this thesis. Also, whenever I missed simple answers because I was too involved in looking for more complex solutions, he helped me get back on track.

The help and support of all my other colleagues is also greatly appreciated, since they helped create a very special atmosphere at my workplace.

A very special thanks to the following colleagues:

- Dr. Tsvetelina Merdzhanova for the interesting discussions on many work-related and other topics during the time we shared an office. While I was focused on simulation and optical effects, she helped me see the bigger picture of our technology and the influence of all things non-optical.
- Dr. Ulrich W. Paetzold for the lively discussions. He helped me see the limits of what I could do with my software and his remarks and criticism helped me improve much of this work.
- Dipl.-Ing. Josef Klomfaß, for his invaluable knowledge about experimental setups, as well as PDS measurements which formed the basis for the optical data used in all simulations.
- Dr. Etienne Moulin for his interest in my work and the opportunity to work with him on publications.
- Dr. Melanie Schulte for her support and interest even in the earliest stages of my thesis, as well as the opportunity to work on publications very early.
- André Hoffmann for SNOM measurements and testing of my software, as well as improving it.

- Stephan Lehnen for SNOM measurements and his great sense of humour, as well as the chance to perform some large simulations for him.
- Maurice Nuys for his help in all the bureaucratic challenges that arose when I submitted my thesis.
- Andreas Lambertz for his extensive knowledge on the workings of layer deposition and their influence on layer properties.
- Andrea Mühlheims for her honest and quick help in the finer points of the administrative tasks at the FZ Jülich GmbH.
- Dr. Bart Pieters for his support and discussions.
- Dipl. Ing. Chao Zhang for the fabrication and measurement of the tandem cell simulated in this thesis.
- Dipl. Ing. Xu Xu for the AFM measurements used for the investigation of non-conformality on cell performance.
- Dr. Wanjiao Böttler for fabrication of the cells presented at EUPVSEC 2012.
- Dr. Vladimir Smirnov for cooperation on the "polished" samples and QE measurements of these cells presented at EUPVSEC 2012.
- Dipl. Ing. Gabrielle Jost for ARS measurements and the nice sketch of the ARS system.
- Dr. Torsten Bronger for his friendship and all the fun we had off-duty.
- B.-Sc. Marvin Goblet for being a loyal friend.
- Oliver Thimm for performing PDS measurements.

I would also like to thank Pierre Wahl for the opportunity to be involved in the development of a great software, B-CALM.

I thank the Jülich Supercomputing Center and their support team for the opportunity to use their HPC systems via a VSR project and their quick and competent support whenever I ran into problems with my simulation software.

Also, I thank all my friends for their support during this time, many of them being very interested in my work. Thanks for keeping my spirits up even when my research did not work according to plan.

And a very special thanks to my parents, Alexander Michael Ermes and Angelika Maria Ermes for their continuous support at all times. Your help, understanding and care helped me to carry on regardless of obstacles and challenges. Thank you!

ASSURANCE

This PhD thesis and the research presented within have been carried out at the IEK5 - Photovoltaik of the Forschungszentrum Jülich GmbH.

Herewith, I declare that this work has been produced personally. All sources, citations and auxiliary means are made recognisable.

Alexander Markus Ermes

Band / Volume 286
Neue Charakterisierungsmethoden für die Gasdiffusionslage in PEM-Brennstoffzellen vor dem Hintergrund produktionsprozessbedingter Materialschwankungen
S. M. Bach (2015), VIII, 149 pp
ISBN: 978-3-95806-088-3

Band / Volume 287
Using the anisotropy of electrical properties for the characterization of sedimentological structures and preferential flow processes
S. Al-Hazaimay (2015), xxii, 94 pp
ISBN: 978-3-95806-090-6

Band / Volume 288
Aktivitätsuntersuchungen und Methoden zur Regeneration von Katalysatoren für die autotherme Reformierung von Dieselkraftstoffen
K. Löhken (2015), II, 147 pp
ISBN: 978-3-95806-093-7

Band / Volume 289
Large-Scale Three Dimensional Modelling of a Direct Methanol Fuel Cell Stack
J. W. McIntyre (2015), 138 pp
ISBN: 978-3-95806-094-4

Band / Volume 290
Abscheidung von Wärmedämmschichtsystemen mit dem Plasma Spray-Physical Vapor Deposition- (PS-PVD-) Prozess – Untersuchung des Prozesses und der hergestellten Schichten
S. Rezanka (2015), XII, 204 pp
ISBN: 978-3-95806-095-1

Band / Volume 291
Characterization & Modification of Copper and Iron Oxide Nanoparticles for Application as Absorber Material in Silicon based Thin Film Solar Cells
M. R. Nuys (2015), XII, 123 pp
ISBN: 978-3-95806-096-8

Band / Volume 292
Interpretation of L-band brightness temperatures of differently tilled bare soil plots
M. Dimitrov (2015), XIV, 116 pp
ISBN: 978-3-95806-098-2

Band / Volume 293
Atrazine in the environment 20 years after its ban: long-term monitoring of a shallow aquifer (in western Germany) and soil residue analysis
D. S. Vonberg (2015), 149 pp
ISBN: 978-3-95806-099-9

Band / Volume 294
Yttria-Stabilized Zirconia / Gadolinium Zirconate Double-Layer Plasma-Sprayed Thermal Barrier Coating Systems (TBCs)
E. Bakan (2015), viii, 131 pp
ISBN: 978-3-95806-100-2

Band / Volume 295
Hydration and dehydration at the tropical tropopause
C. Schiller (2015), 72 pp
ISBN: 978-3-95806-101-9

Band / Volume 296
Influence of Impurities on the Fuel Retention in Fusion Reactors
M. Reinhart (2015), 140 pp
ISBN: 978-3-95806-105-7

Band / Volume 297
The role of abiotic processes in the formation and degradation of gaseous nitrogen compounds in the soil
J. Heil (2015), XIV, 106 pp
ISBN: 978-3-95806-106-4

Band / Volume 298
12th Carolus Magnus Summer School on Plasma and Fusion Energy Physics
edited by Kristel Crombé (2015), 468 pp
ISBN: 978-3-95806-107-1

Band / Volume 299
Optical near-field investigations of photonic structures for application in silicon-based thin-film solar cells
A. M. Ermes (2015), vi, 157 pp
ISBN: 978-3-95806-108-8

Energie & Umwelt /
Energy & Environment
Band / Volume 299
ISBN 978-3-95806-108-8

JÜLICH
FORSCHUNGSZENTRUM